Global Observations of Physical and Biogeochemical Processes in the Ocean

Tyler D. Hennon

A dissertation
submitted in partial fulfillment of the
requirements for the degree of

Doctor of Philosophy

University of Washington

2016

Reading Committee:

Stephen Riser, Chair

Steven Emerson

Sabine Mecking

Program Authorized to Offer Degree:
School of Oceanography

University of Washington

Abstract

Global Observations
of
Physical and Biogeochemical Processes
in the Ocean

Tyler D. Hennon

Chair of the Supervisory Committee:
Professor Stephen Riser
School of Oceanography

We employ numerous global, or semi-global, datasets to observe the large-scale variability of physical and biogeochemical phenomena. In Chapter 1, we use Argo floats to estimate the vertical displacement of internal gravity waves. Internal wave intensity is found to be positively correlated with bathymetric roughness and proximity to the seafloor. The global variability of internal wave intensity also strongly resembles patterns of diapycnal diffusivity established by prior studies, suggesting breaking internal waves are largely responsible for abyssal mixing. In Chapter 2, we use Argo floats equipped with dissolved oxygen sensors to measure oxygen drawdown beneath the mixed layer, which is representative of respiration and remineralization of organic matter. We observe strong regional variability across the eight locations examined. Depth-integrated respiration is used as a lower-bound for organic carbon exported from the surface ocean. We find that carbon export and export efficiency is low at weakly seasonal locations, and high at strongly seasonal locations. In Chapter 3, we use a variety of datasets to construct composite averages of mesoscale eddy characteristics. By using repeat hydrography, we are able to estimate the nitrate anomaly within the interior of eddies. Additionally, satellite observations allow us to estimate the chlorophyll anomaly at the surface. By combining subsurface and surface observations, we examine how the nitrate

anomaly covaries with the chlorophyll anomaly. Although our observations only allow us to explore global variability very coarsely, we find that the influence of mesoscale eddies on nutrients and chlorophyll is significantly different at low-, mid-, and high-latitude.

TABLE OF CONTENTS

ACKNOWLEDGMENTS

I would like to acknowledge friends and family for their kind support, as well as all the colleauges and mentors at UW (and elsewhere) for their excellent guidence and professionalism.

DEDICATION

To Gwenn and Isaac

INTRODUCTION

The ocean is, in general, a poorly sampled environment. Until the initiation of programs such as Argo, World Ocean Circulation Experiment (WOCE), and numerous satellite missions, oceanographers were often required to make extrapolations based on highly limited observations. While it is still practically impossible to fully resolve even the most basic parameters in the ocean (temperature and salinity), in many cases these global, or semi-global datasets (often coupled with models) have allowed the oceanographic community to estimate the first-order variability of physical and biogeochemical processes, spanning from turbulent mixing (*Kunze et al.*, 2006; *Whalen et al.*, 2012) to carbon sequestration (*Dunne et al*, 2005; *Henson et al.*, 2012). These global observations serve as a starting point to determine the importance of dynamics on smaller scales. The chapters of this thesis are unified by the theme of global observations (with a particular emphasis on observations of autonomous Argo floats) and the important insights they provide to our understanding of a wide range of natural phenomena.

Chapter 1

A comprehensive understanding of internal waves is essential to our ability to estimate global mixing patterns (*Munk and Wunsch*, 1998), on which ocean circulation and overturning is highly dependent (*Samelson*, 1998; *Simmons*, 2004). However, most observations are based on mooring (*Alford and Whitmont*, 2007) or satellite observations (*Alford*, 2003), and wide-ranging *in situ* measurements are often lacking. In Chapter 1 we aim to mitigate this problem by using park-phase data from ∼200 Argo floats to observe internal wave activity. This new method yields semi-global observations of internal wave intensity, showing regions that are relatively quiescent and others that are far more energetic, and patterns bear strong resemblance to prior observations of diapycnal mixing. We find correlations between internal wave intensity and local bathymetric conditions. We also demonstrate that Argo floats are capable of resolving internal wave behavior on relatively fine spatial scales from observations of a single float around two seamounts in the Southern Ocean.

Chapter 2

The ocean acts as a sink to anthropogenic CO_2 (*Sarmiento and Gruber*, 2002). Organic forms of carbon are exported from the surface of the ocean and eventually sequestered, a process known as the biological pump. Respiration plays an important role in determining what fraction of organic matter exported from the surface eventually reaches the deep ocean (*Martin et al.*, 1987). In the last decade, several hundred Argo floats have been equipped with oxygen sensors (*Gruber et al.*, 2007) to expand the breadth of the Argo program to biogeochemical topics. In Chapter 2, we estimate respiration and carbon export below the mixed layer with floats equipped with dissolved oxygen sensors. With this *in situ* dataset, we are able to estimate the vertical profile of respiration at eight distinct locations around the globe (varying from low- to high-latitude). We also use the depth-integrated respiration coupled with satellite estimates of surface net primary production to formulate lower bounds on export and export efficiency from the surface ocean. We find that export and export efficiency vary significantly with latitude, although our observations may be biased low at weakly seasonal locations.

Chapter 3

It has been known for some time that diffusive processes alone cannot supply the euphotic zone with the nutrients required to balance the biological uptake (*Ledwell et al.*, 1993). Mesoscale eddies are one mechanism expected to be a significant term in closing the nutrient budget (*Oschlies and Garcon*, 1998), as cyclonic eddies uplift nutrient-rich isopycnals to depths accessible to phytoplankton. There are a myriad of studies that make detailed full-depth *in situ* observations of a single eddy event (*Falkowski et al.*, 1991; *Siegel et al.*, 2008), or estimate the average effect of eddies on surface chlorophyll using thousands of satellite observations (*Chelton et al.*, 2011a; *Siegel et al.*, 2011). In Chapter 3 we again utilize global datasets to examine this topic on a global scale. Although there are a number of floats equipped with nitrate sensors, their population is too few and coverage too sparse to allow us to characterize global trends. Here, we instead turn to the World Ocean Database (WOD; *de Boyer Montégut et al.* (2013)) for our primary *in situ* dataset. We use a number of global datasets (WOD included) to assess, in an average sense, the effects of eddies on both surface chlorophyll and subsurface nutrient availability. We construct regional composites that allow us to characterize the effect of eddies on nutrients and chlorophyll at many different regions across the globe. We find relatively strong correlations between nutrient availability and surface chlorophyll at low- and mid-latitude, but not high latitude, suggesting fundamentally different biophysical behavior there.

Chapter 1

OBSERVATIONS OF INTERNAL GRAVITY WAVES BY ARGO FLOATS

CITATION

Hennon, T. D., S. C. Riser, and M. H. Alford (2014), Observation of Internal Gravity Waves by Argo Floats, *Journal of Physical Oceanography*, **44 (9)**, 2370-2386, doi:10.1175/JPO-D-13-0222.1.

Abstract

We examine the global variability of the internal wave field near a depth of 1000 m using data from a set of 194 Argo floats equipped with Iridium communications, capable of measuring hourly temperature and pressure during the park-phase of their 10 day cycles. The data have been used to estimate vertical isotherm displacements at hourly intervals, yielding a global measure of the heaving due to internal gravity waves. The displacement results have been employed to examine the global variability of these waves and how the displacement power spectrum compares to the canonical Garrett-Munk spectrum. Using the data, we find correlations between internal wave intensity and seafloor roughness, proximity to the seafloor, and the magnitude of the local barotropic velocity. The measurements also show large seamount-trapped waves at high latitudes and coastally-trapped sub-inertial waves. These observations provide a rough global census of the nature of these waves that can ultimately be used in studies of ocean mixing.

1.1 Introduction

It has been suggested for some time that ocean stratification and meridional overturning are related to the strength of abyssal mixing (*Munk*, 1966). More recently acknowledged has been the role of the spatial variability in mixing to these processes (*Samelson*, 1998; *Simmons*, 2004). Despite this importance, global patterns of mixing are still relatively poorly understood. Internal waves are thought to be a key contributor to abyssal mixing (*Munk and Wunsch*, 1998). They overturn and break, much like surface waves. Via turbulence, this dissipates some of their energy, which leads to diapycnal mixing. Hence, understanding the variability of internal waves can yield clues to the distribution of dissipation and mixing throughout the ocean (*Gregg*, 1989).

Recent studies (*Kunze et al.*, 2006; *Whalen et al.*, 2012) have attempted to assess the global distribution of diapycnal mixing. In this work we present broad observations that complement these works by examining the global behavior of internal waves using data collected from a suite of profiling floats deployed as part of the global Argo array. The general behavior of these floats has been described in a number of places (*Roemmich et al.*, 2004). The floats used in Argo typically cycle vertically between 2000 m and the sea surface on approximately 10 day cycles, collecting profiles of temperature and salinity as a function of pressure during their ascent. In many cases the floats also collect periodic observations of temperature during their park-phase at 1000 m. In this work we examine the park-phase temperature variability from a suite of 194 floats deployed over the globe by the University of Washington during the period 2004-2013. These floats were all equipped with Iridium communications and thus were capable of storing and transmitting considerably more data than most other active Argo floats during this time period. In the suite of floats used in this work, temperature and pressure observations were collected at 1 hour intervals during the park-phase, allowing variability in the internal gravity wave frequency band along the float paths to be examined.

As will be shown in Section 1.2, the park-phase temperature data from the floats can be used to examine the vertical displacement spectrum of internal gravity waves at the park depth. Due the quasi-Lagrangian nature of the float motion during their park-phase, the effect of advection on Argo floats can be assumed to be minimal. Thus, even in regions with fast currents (e.g., the Antarctic Circumpolar Current), the data can be used to make credible estimates of the displacement spectrum uncontaminated by Doppler shifts in frequency.

In a prelude to our broad analysis we focus on two case studies of specific floats (Section 1.3). Following the two case studies, we will turn our attention to observations made by our dataset (Section 1.4) and comparisons to the empirically derived Garrett-Munk (GM) spectrum (*Garrett and Munk*, 1975). While the energy spectra of internal waves in much of the world's oceans have properties similar to the GM spectrum, regions whose spectra depart markedly from this model are clearly of interest, perhaps as sources or sinks of internal wave energy (*Wunsch*, 1975). Deviations could also point to areas where the GM description is inadequate (*Levine*, 2002).

Also in Section 1.4 we examine the effects of seafloor roughness, height above the seafloor, and barotropic velocity magnitude on internal wave intensity. Internal waves are one of the primary mechanisms for mixing the deep ocean (*Munk and Wunsch*, 1998), and because diapycnal diffusivity is known to be elevated above rough bathymetry (*Polzin et al.*, 1997; *Ledwell et al.*, 2000) we examine the possibility internal waves might be excited in these areas as well. We also examine the properties of internal gravity waves at high latitudes.

1.2 Methods

1.2.1 Displacement Estimates

The data presented in this work come exclusively from a set of 194 University of Washington Argo floats using Iridium communications, which have a broad spatial coverage (shown in Fig. 1.1). The primary mission of these floats is to collect vertical profiles of temperature and salinity in the upper 2000 m of the ocean, nominally at ten day intervals. The floats drift freely during a quasi-isobaric park-phase at 1000 dbar between profiles. These floats collect hourly measurements of temperature and pressure during the park-phases. Thus, from these hourly measurements we can observe the temperature variability representing isotherms heaving vertically past the quasi-isobaric float. As an example, Fig. 1.2 shows hourly temperature measurements during both a single park-phase for UW float 5135 and over the entire float lifetime.

With the knowledge of the local temperature gradient obtained from the vertical profiles, we can translate the temperature fluctuations into isotherm displacement. It is assumed that isotherm displacements are primarily due to internal wave motion, at least for periods less than a few days.

For individual park-phases, we estimate the hourly vertical isotherm displacement observed by the float, $\eta_T(t)$, as

$$\eta_T(t) = \frac{T_p(t) - \overline{T_p}}{(dT/dP)_{1000}} \tag{1.1}$$

Here $\overline{T_p}$ is the time average of the hourly park-phase temperature measurements, $T_p(t)$ over one park-phase and $(dT/dP)_{1000}$ is the temperature gradient at 1000 dbar, estimated using the profile measurements within 100 dbar of the parking pressure. The temperature gradient is calculated from the average of the vertical profiles immediately before and after the particular park-phase.

If the floats were perfectly isobaric, ηT would be the only estimate needed to determine vertical isotherm displacement. However, the floats are imperfect and do typically experience small vertical motions while in the park-phase, so the float's displacement, η_P, needs to be taken into account and removed from the total isotherm displacement. We define the float displacement as

$$\eta_P(t) = \overline{P_p} - P_p(t) \tag{1.2}$$

Here $\overline{P_p}$ is the time average of the hourly park-phase pressure measurements, $P_p(t)$, taken over one park-phase cycle. The float motion, η_P, is typically less than 20% of η_T. By taking the motion of the float into account, we arrive at a corrected estimate for isotherm displacement, and hence vertical internal wave displacement, (t), given by

$$\eta(t) = \eta_T(t) + \eta_P(t) \tag{1.3}$$

An example of the various components of $\eta(t)$ is shown in Figure 1.3. In our analyses here, we have chosen to high-pass $\eta(t)$ using a fourth-order Butterworth filter in order to remove all variability below 0.3 cycles per day (cpd). This filtering removes error from slow temperature trends during the park-phase that is likely due to low-frequency spatial variability and water-mass changes. Poleward of about 10 of latitude the inertial frequency exceeds 0.3 cpd, so except near the equator the inertial peak is not removed by this filter.

1.2.2 Combining Park-Phases for Longer Records

In analyzing the internal wave displacement it can sometimes be advantageous to examine each set of park-phase data as a discrete time-series. This gives good temporal resolution $\sim$ 10 days) of the variability of the spectrum, but it comes at the expense of frequency resolution in spectral analysis. In other cases it is acceptable to increase the length of the park-phase record in order to have better frequency resolution, but for this requires time-series that are longer than the 10-day park-phases.

To examine longer records, we have stitched together all the individual park-phase records for $\eta(t)$ to create a single multiyear time-series for each float. We linearly interpolate $\eta(t)$ of all park-phases in order to create a set of hourly samples that is the length of the operative mission of the float, typically several years (an example is given in Fig. 1.4). After interpolation, hourly bins that correspond to times when the float is in its profiling phase (about 6 hours every 10 days) are set to zero (the park-phase displacement average, adding no variance). Additionally, all $\eta(t)$ for park-phases that do not meet quality controls are set to zero (see Section 1.2.3 below for details on quality control). The advantage of having one long time-series for each float is that it can be broken down into uniform segments that are longer than 10 days. In this work we have typically used non-overlapping 30-day segments, as this considerably increases the frequency resolution without sacrificing too much temporal and spatial resolution. Constructing 30-day segments of $\sim$10 day park-phases by filling the time (typically 6 hours) between park-phases with zeros does not in practice distort the shape of the power spectrum to a degree that affects our analysis.

1.2.3 Quality Control

We have implemented several quality controls in order to avoid unreasonable estimates for internal wave displacement. For each park-phase we have required that

- The temperature profile in the vicinity of 1000 dbar is nearly linear. We find the least squares best-fit line to the temperature profile within 100 dbar of the parking depth. This best-fit line must account for at least 90% of the variance of the local temperature profile for the displacement data to be included our analysis. This is the most common quality criterion that is violated (in just over 10% of park-phases), occurring most often at high latitudes where density is increasingly dependent on salinity instead of temperature.

- The parking pressure is within 50 dbar of 1000 dbar. Occasionally a float will park at a pressure significantly different than 1000 dbar. For consistency, data from these park-phases are not included in the analysis.

- The vertical float movement is minimal. There can be no more than one pressure measurement in each park-phase that deviates more than 50 dbar from the average parking depth. Float motion is accounted for in Eq. 1.2 and 1.3, but park-phases with large deviations are eliminated to avoid excessive error.

- Park-phases have at least 24 hourly measurements. The number of samples in most park-phases greatly exceeds this number.

If any of these conditions are violated for a particular park-phase, the corresponding hourly bins for the entire park-phase are set to zero.

1.2.4 Power Spectra

Whether we use the park-phase segments or the 30-day segments (described in Section 1.2.2), the power spectrum for segment j, $S_j(\omega)$, is defined for a discrete time-series as

$$S_j(\omega) = \frac{2}{M_j \Delta t} \big| \Delta t \cdot \sum_{m=1}^{M_j - 1} \eta_{j,m} e^{-i2\pi\omega\Delta T} \big|^2 \tag{1.4}$$

Here M_j is the number of hourly measurements in the j^{th} park-phase or 30-day segment, Δt is the time between measurements (one hour), and ω is the frequency of oscillation. The factor of two comes from confining frequencies to positive values only, considering the symmetry of the displacement spectrum in positive and negative frequencies. The total variance in $S_j(\omega)$ is exactly equal to the variance in the j^{th} temporal segment, in accordance with Parseval's theorem.

The spectrum from each of the 30-day segments for a single float can be formed into a mean power spectrum, which is useful for accurately quantifying typical internal wave behavior for a float that did not drift over vast distances. We define the average power spectrum, $\overline{S}(\omega)$, as the mean of all $S_j(\omega)$ for the 30-day segments. Choosing 30-day segments gives a frequency resolution of 0.03 cpd for the power spectrum. The hourly measurements during each segment result in a Nyquist frequency of 12 cycles per day, and thus the major tidal and inertial frequencies are generally well-resolved with this method. Segments that have zeros (corresponding to times of vertical profiling, or data that did not meet quality control criteria) in more than 50% of their hourly bins are not included in the estimate for $\overline{S}(\omega)$. An example of $\overline{S}(\omega)$ is shown in Fig. 1.5 and will be discussed in Section 1.3.1).

In this study we calculate spectra that are obtained from individual park-phases as well as the longer 30-day segments. We use park-phases in Sections 1.4.1, 1.4.3, and 1.4.4 where the precise location is more important than accurate frequency resolution. Conversely, in Section 1.4.2, the frequency resolution is of greater importance to us than the floats' location, so the 30-day segments are used for analysis. Section 1.3.2 uses the 30-day segments to describe general trends (Figs. 1.6 and 1.7) and then uses park-phases to explore the data with greater temporal/spatial resolution.

Generally, we used the 30-day segments to calculate $\overline{S}(\omega)$ in favor of the park-phases because the individual park-phases can vary in temporal duration thus causing the frequency grids for the spectral estimates to be non-uniform. However, as a consistency check we compared the power spectrum for each float using the park-phases with the 30-day segments (we truncated some park-phases to yield a uniform number of hourly measurements to ensure a consistent frequency grid). There was little quantitative difference between the average power spectrum from the park-phase segments and the 30-day segments, which suggests that the spectrum of the 30-day segments is not severely distorted. Examples of this can be seen in Figs. 1.5 and 1.6.

1.2.5 Error Analysis

The Argo floats are outfitted with the SBE41/41CP CTD module, fabricated by Seabird Electronics. The SBE41/41CP has an accuracy of ± 0.002 ^{o}C (.0002 ^{o} C drift per year) and ± 2 dbar (0.8 dbar drift per year) for temperature and pressure, respectively (available from seabird.com). The precision (i.e. sensitivity) of the pressure measurement is roughly two orders of magnitude smaller than the accuracy of ± 2 dbar (Dana Swift, personal communication). Equations 1.1 and 1.2 remove the mean temperature and pressure during the parking-phase, and as a result it is the precision (rather than accuracy) that will affect the quality of our observations.

The range of temperature and pressure is typically on the order of 0.1^{o}C and 1-10 dbar (see Fig. 1.3) while the precision of temperature and pressure is orders of magnitude smaller than these values. Therefore, the majority of the variability seen in temperature and pressure is real, rather than measurement error.

Equation 1.1 assumes a constant vertical temperature gradient, which introduces additional error. However, we only analyzed park-phases where the temperature profile was nearly linear in the vicinity of the parking depth (see Section 1.2.3, so the use of a constant gradient should not introduce a large error.

We assume a chi-square distribution on our spectral estimates, $S_j(\omega)$. The integrated internal wave variance during park-phases is a prevalent quantity in our paper (see Section 1.4). During a park-phase that lasts 4-9 days, there are approximately 100-200 degrees of freedom that make up each integrated internal wave variance estimate. This leads to an error of 20-30%, which is likely the largest source of error on our estimates of internal wave variance.

Given the variability shown in subsequent sections is much larger than these combined sources of error, we are confident that the trends presented by this paper are an accurate representation of real-world phenomena.

1.3 Single Float Case Studies

1.3.1 Common Features

Most floats used in this paper operated for at least three years and completed at least 100 cycles. UW Float 5135 (World Meteorological Organization (WMO) 5901312) had a lifetime of nearly 5.5 years and collected profile and park-phase data from over 200 cycles; the averaged power spectrum ($\overline{S}(\omega)$) from this float is shown in Fig. 1.5.

Its location for the entire deployment was over a relatively small region just west of Australia. Given the length of deployment and limited spatial range, we would expect $\overline{S}(\omega)$ to be generally representative of the internal wave behavior in the area.

Some of the most obvious features in Fig. 1.5 include the inertial peak and the diurnal and semidiurnal tidal peaks. The semidiurnal peak is ubiquitous for all floats in the dataset, although this peak sometimes is blended with the near-inertial peak at higher latitudes. The diurnal peak is a common feature equatorward of 30^o. Poleward of 30^o, the diurnal peak usually vanishes, though important exceptions exist that will be discussed later in the paper. The near-inertial peak is also a nearly ubiquitous feature in the dataset. For simple linear internal gravity waves, vertical motion (and thus temperature variability) vanishes at the inertial frequency; thus the observed peak is likely due to contributions from near-inertial motion, when the waves oscillate with some vertical component. The dispersion relation for linear, freely propagating internal gravity waves confines the waves to exist in a band of frequencies bounded below by the inertial frequency and above by the buoyancy frequency.

Here we define the buoyancy frequency, N, as

$$N^2 = -\frac{g}{\rho}\frac{\delta\rho}{\delta z} \tag{1.5}$$

where g is the force of gravity, and ρ is potential density. In Eq. 1.5, N has units of radians per unit time, but in this study we convert to cpd by introducing a factor of $(2\pi)^{-1}$. A cutoff in the spectrum at frequencies below the inertial frequency can be seen in Fig. 1.5. The buoyancy frequency for float 5135 is about 30 cpd, well above the Nyquist frequency for our data (12 cpd), so the theoretical high-frequency cutoff cannot be seen in this case. The buoyancy frequency generally exceeds 12 cpd for floats at low- to mid-latitudes. Only at high latitudes do some floats experience buoyancy frequencies that are lower than 12 cpd. In these conditions, we generally observe a steep drop-off in spectral density above the buoyancy frequency as predicted by simple linear theory. Less obvious harmonic signals are also noticeable in Fig. 1.5. There is a peak near the $2M_2$ and $M_2 + K_1$ frequencies (M_2 and K_1 are prominent semidiurnal and diurnal tidal frequencies, respectively). Although not present in Fig. 1.5 significant peaks at $M_2 + f$ are discernible for a number of floats (where f is the local inertial frequency). For float 5135, the spectral density at frequencies above the semidiurnal peak is quite consistent with the GM spectrum in both magnitude and slope, as can be seen in Fig. 1.5 (spectra from other floats are also generally consistent with the GM spectrum and are examined in further detail in Section 1.4.2).

1.3.2 Observations of Seamount-Trapped Waves

A second case study we present is notable for its uniqueness in the dataset. Float 6097 (WMO 5902118) was subjected to very large diurnal motion while in the vicinity of two seamounts around the Amundsen (see Fig. 1.6 for the trajectory). For freely propagating internal gravity waves, diurnal motion is generally not permitted poleward of $\sim 30^o$, as beyond these latitudes the diurnal frequencies are below the inertial frequency. Yet the averaged power spectrum from this float shows a strong peak at the diurnal frequency (see

Fig. 1.6). As can be seen in Fig. 1.7 (the temporal evolution of the spectrum), however, this peak is not steady in time. The elevated diurnal activity only appeared when the float was in the immediate vicinity of the two seamounts. To examine this further, we quantify our observations by defining diurnal variance or semi-diurnal variance, σ_j^2, during j^{th} park-phase as

$$\sigma_j^2 = \int_{\omega_o - \Delta\omega}^{\omega_o + \Delta\omega} S_j(\omega) d\omega \tag{1.6}$$

where ω_o is the K_1 or M_2 frequency used for calculating the diurnal or semidiurnal variance, respectively. We have chosen $\Delta\omega$ to be 0.3 cpd in order to capture as much as possible of the variance in and around the semidiurnal and diurnal peaks. The semi-diurnal variance is calculated to provide a standard with which we can compare changes in diurnal variance. As can be seen in Fig. 1.8, it would seem that there is a connection between proximity to the seamounts and the strength of the diurnal signal.

The variance in the semidiurnal and diurnal bands can be examined as a function of seafloor depth, which in this case can be thought of as a proxy for proximity to the seamounts. As can be seen in Fig. 1.9, the semidiurnal peak increases by about an order of magnitude over the seamounts compared to the open ocean. While a significant increase, this is greatly exceeded by the change in the diurnal signal, which increases by three to four orders of magnitude near the two seamount apexes. The vertical amplitude of the seamount trapped waves measured by the floats is often around 100 meters, and during early 2011 amplitudes in excess of 200 meters were observed, as shown in Fig. 1.10.

In a modeling study, Brink (1990) found similar results, with sub-inertial variance near a seamount increasing several orders of magnitude above the open ocean levels. Around the same time, moored observations showed that the diurnal tidal amplitude increased significantly near Fieberling Guyot in the eastern North Pacific (*Eriksen*, 1991). Eriksen also found that there was a spring-neap cycle to the diurnal amplitude, a pattern we also observe for a month-long period as shown in Fig. 1.10. The data suggest that these two seamounts in the Amundsen Ridge could be sites of elevated mixing due to the large internal waves that are consistently present there; unlike superinertial internal gravity waves, these diurnal waves are trapped and not free to propagate away from the seamounts implying that any energy initially input into baroclinic diurnal motion will ultimately be dissipated locally.

1.4 Multi-Float Observations

1.4.1 Global Observations

While the float ensemble used here does not have complete spatial coverage over the world's oceans, there are large regions of the ocean that are well-sampled. These regions are diverse enough that we can begin to quantify how internal waves behave under a variety of conditions. Fig. 1.11 shows a global plot of internal wave displacement variance derived from each park-phase of every instrument included in this ensemble. The internal wave displacement variance during park-phase j is

$$\sigma_j^2 = \int_f^N S_j(\omega) d\omega \tag{1.7}$$

where N and f are the local buoyancy and inertial frequencies. These limits are chosen based on the properties of the dispersion relationship for linear, freely propagating internal waves. In practice, it is not possible to integrate to the buoyancy frequency when it is above the Nyquist frequency. In these cases, we integrate only to the Nyquist frequency.

1.4.2 Comparisons to the Garrett-Munk Spectrum

We examine the relationship between the observed internal wave spectrum and the expected Garrett-Munk displacement spectrum, originally formulated by *Garrett and Munk* (1975) and modified by *Cairns and Williams* (1976). To quantify the comparisons, we estimate the variance of the Garrett-Munk spectrum (henceforth GM76, after the *Cairns and Williams* (1976) modifications) integrated between 3 cpd and 6 cpd, and the variance of a fit of the float-derived spectrum integrated between 3 cpd and 6 cpd. We choose to integrate over this particular frequency range because 3 cpd is well above the main tidal/inertial frequencies while 6 cpd is almost universally lower than the buoyancy frequency observed by all the floats in the ensemble. Thus, this frequency domain should extend over a fairly consistent region of the observed spectrum.

The expected variance (EV) is established by integrating the local GM spectrum, $GM_i(\omega)$, of each 30-day segment of each float from 3 cpd to 6 cpd,

$$EV_i = \int_{3cpd}^{6cpd} GM_i(\omega, f, N) d\omega \tag{1.8}$$

Here $GM_i(\omega, f, N)$ depends on the local inertial and buoyancy frequencies and has been evaluated via MATLAB using the GM76 Toolbox (Klymak, unpublished). The subscript i denotes the i^{th} 30-day segment. To characterize the observed spectrum, we obtain a least-squares fit of $S_i(\omega)$ between 3 cpd and the Nyquist or buoyancy frequency (whichever is lower). The fit is referred to as $F_i(\omega)$, and takes the form

$$F_i(\omega) = C_1 \omega^{C_2} \tag{1.9}$$

where C_1 and C_2 are constants defined by the best fit (C_2 is typically around 2, consistent with the GM expectations). Not all frequency bins of $S_i(\omega)$ above 3 cpd and below the buoyancy/Nyquist frequency are included in the fitting process, however. The frequency bins within 5% of $M_2 + K_1$, $M_2 + f$, and integer multiples of M_2 are not included in fitting F_i so that it only characterizes the background slope of the spectrum, rather than include the effects of these peaks. Once $F_i(\omega)$ is obtained from $S_i(\omega)$, it is integrated from 3 cpd to 6 cpd to calculate the observed variance (OV_i),

$$OV_i = \int_{3cpd}^{6cpd} F_i(\omega) d\omega \tag{1.10}$$

The ratio of OV_i/EV_i provides an estimate of the similarity between the observed internal wave spectrum and the GM spectrum for each 30-day segment; a global map of this ratio is shown in Fig. 1.12. The ratio exceeds one in typically energetic regions of the ocean such as the Antarctic Circumpolar Current (ACC), the Hawaiian Ridge, and portions of the Gulf Stream. It is not surprising that the observed ratio is approximately one near the Northwest Atlantic continental slope (the Woods Hole Oceanographic Institution Site D, located at roughly 39^o N, 70^o W), the location of numerous long-term moorings in the 1970s that had a large influence on the development of the GM models (Garrett and Munk, 1975). There are also large regions where the internal wave displacement spectrum falls far below the expected GM spectrum. These regions often appear to correspond to areas with smooth bathymetry or regions at high latitudes. Data within 10 degrees of the equator were excluded as the GM spectrum from 3 to 6 cpd approaches zero at the equator (forcing OV_i/EV_i to infinity).

1.4.3 Effects of Local Bathymetry and the Barotropic Tide

The float dataset used here is unique in its ability to observe the broad relationship between internal waves and bathymetric variability over large spatial scales. Although the float ensemble used here does not provide truly global coverage, the floats used have been deployed over diverse bathymetric conditions and thus provide a wealth of knowledge of internal wave intensity at a depth near 1000 m over both rough and smooth conditions. The distance from 1000 m to the seafloor is quite variable, so we can observe the effects of proximity to the seafloor on internal wave displacement. With use of the tidal model, TPXO 7.2 (*Egbert et al.*, 1994), examination of the effects of the barotropic velocity on internal wave intensity can also be examined.

1.4.4 Internal Waves vs. Roughness and Proximity to Bottom

We characterize the local bathymetric conditions (roughness and float height above bottom) using the ETOPO1 (*Amante and Eakins*, 2009) data within 100 km of the surface location. ETOPO1 has one arc-minute resolution of the Earth's land and seafloor topography, and is constructed from a number of datasets that are primarily based off of bathymetric soundings and satellite gravimetry. The 100 km radius is chosen as it is on the order of the horizontal wavelength of the first baroclinic mode internal waves of the semi-diurnal frequency; our results are not particularly sensitive to this choice. The ETOPO1 data within 100km of a float position is weighted in a Gaussian manner so that the bathymetry directly under the float is most heavily weighted, yet the influence of bathymetry at the fringe of the 100 km radius is still included (again, the results are not particularly sensitive to the weighting scheme). The weighting factor is

$$w_i = e^{(L_i/100km)^2}(1.11)$$

where L_i is the horizontal distance of the i^{th} ETOPO1 data point from the location of the float park-phase location. We calculate a weighted average of depth, $\overline{D}$, by weighting all individual ETOPO1 depths, D_i, by w_i. Because floats park at approximately 1000 m depth, the height in meters above the bottom, H, is then

$$H = \overline{D} - 1000 \tag{1.12}$$

The bottom roughness, R, is the weighted standard deviation of depth around D,

$$R^2 = \frac{1}{\sum\limits_{i=1}^{J} w_i} \cdot \sum_{i=1}^{J} [\overline{D} - D_i]^2 \cdot w_i \tag{1.13}$$

where J is the total number of depth measurements within the 100 km radius of the float. Although not shown in equation 1.13, we have removed the best-fit plane (by least-squares) from the data so that smooth sloping bathymetry (e.g. some continental slopes) is not parameterized as rough. From each park-phase, we obtain three important estimates for comparing internal waves to local bathymetry: (1) the internal wave variance (σ^2, equation 7); (2) the weighted bottom roughness (R); and (3) the weighted height above the bottom (H).

As an example, we show in Fig. 1.13 a time series of all three quantities for UW float 5061 (WMO 1900413). Float 5061 was deployed in the middle of the Indian Ocean, and over the course of its multiyear lifespan traveled westward across the Southwest Indian Ridge. During the period that the float crossed the ridge, H decreased and R increased, indicating shallower, rougher local conditions. Internal wave variance correspondingly increased significantly, which can be seen in Fig. 1.13. Similar correspondences can be seen throughout the float ensemble, as is shown in Fig. 1.14, showing internal wave variance as a function of height above the seafloor and bottom roughness for each park-phase of every float.

1.4.5 Internal Waves vs. Roughness and Barotropic Tides

As the barotropic tide generates fluid oscillations over bathymetric irregularities, internal waves are created. Thus, it is reasonable to hypothesize that the intensity of the internal waves generated will not only depend on the roughness, but also the strength of the barotropic tide. Here we examine the relationship between internal wave variance, barotropic velocity strength, U, (as calculated by TPXO 7.2), and the bottom roughness (ETOPO1). Floats in regions of fast lateral advection have been removed from this analysis, because as will be discussed (Section 1.5.1) internal lee waves can be a significant source of internal waves. This source of internal waves obscures the barotropic tidal signal we wish to examine; hence these floats are not included. We remove floats that had a mean horizontal velocity (calculated from distance and time between profiles) greater than 0.1 m s^{-1}. These floats came primarily from the ACC, Gulf Stream, Kuroshio, and equator, and accounted for 18% of the total number of floats.

The definitions for internal wave variance, σ^2, and bottom roughness, R, are again defined by Eqs. 1.7 and 1.13, respectively. Both are calculated once for each park-phase. The strength of the barotropic tidal velocity, U, is also calculated once per park-phase and is defined as

$$U^2 = \frac{1}{K-1}\sum_{k=1}^{K}[u_k - \overline{u}]^2 + [v_k - \overline{v}]^2 \tag{1.14}$$

Here U^2 is the combined variance of the east-west and north-south barotropic velocities, u and v, respectively. The velocities are computed onto an hourly grid during each park-phase by the TPXO model 7.2 (Egbert et al., 1994), and K is the total number of hourly velocities during the park-phase. Fig. 1.14 shows internal wave displacement variance plotted against roughness (R) and barotropic velocity (U). Internal wave variance appears to have noticeable correlations with both bottom roughness and the barotropic velocity. This suggests that strong tides oscillating over coarse bathymetry present favorable conditions to internal wave generation. Combined, Figs. 1.14 and 1.15 illustrate that, in a broad sense, internal wave intensity is strongly dependent on seafloor roughness, proximity to the seafloor, and the strength of the local barotropic tides. While these findings are not a revelation, it is still informative to observe general trends of internal waves over the wide range of conditions the float database encompasses.

1.4.6 Sub-Inertial Diurnal Waves

The dataset provides broad float coverage poleward of 30^o, especially in the Southern Hemisphere, and the measurements indicate a number of cases of notable diurnal intensification above the turning latitude $\sim 30^o$, as shown in Fig. 1.16. Each point in Fig. 1.16 represents the difference of the diurnal peak from the background of the spectrum, rather than the total diurnal variance.To calculate the difference, first we integrate over three regions of each park-phase spectrum, including: (*i*) the three frequency bins closest to one cycle per day; (*ii*) the three frequency bins immediately above those in (*ii*); and (*iii*) the three frequency bins immediately below those in (*i*).

The integrated variance arising from (*ii*) and (*iii*) are then averaged to estimate the background variance of the spectrum just outside the diurnal range. This average is then subtracted from (*i*) to estimate the degree to which diurnal variance exceeds the background variance of the spectrum (if at all), which we refer to as the diurnal prominence (P, in Figs. 1.16 and 1.17). The park-phases do not all have uniform duration. While most are close to nine or ten days, some are closer to five days, which causes the frequency resolution to change depending on the length of the park-phase. This means that the three frequency regions (*i-iii*) do not occupy a completely uniform range for all floats (the frequency resolution is usually between 0.1 and 0.2 cpd). Because we are examining qualitative trends only, the moderate differences in frequency resolution do not significantly affect our conclusions.

We can also estimate the difference of the diurnal variance from the spectral background in an effort to negate any spectral broadening that may occur in areas of high overall variance (the ACC for example). In some cases there exists a relatively high diurnal variance even when no clear diurnal peak is discernible. While prominent diurnal peaks are not uncommon equatorward of 30^o, poleward of this latitude discernible diurnal peaks become much less frequent and more localized. This topic is examined in detail in the following section.

1.5 Discussion of Multi-Float Observations

1.5.1 Global Observations

Perhaps the most striking feature in Fig. 1.11 is the intensification of internal wave variance in the path of the Antarctic Circumpolar Current (ACC) east of Drake Passage. The pattern of intensification is qualitatively similar to recent estimates of energy flux from geostrophic flows into internal lee waves (*Nikurashin and Ferrari*, 2011). This suggests that lee waves could be a significant contributor to internal waves in the ACC east of Drake Passage. Both *Whalen et al.* (2012) and *Wu et al.* (2011) present detailed observations of diapycnal diffusivity in the Southern Ocean. Each study shows that, qualitatively, the spatial pattern of diffusivity is comparable to the pattern of internal wave variance in Fig. 1.11. Coupled with these recent studies, our observations help corroborate the notion that breaking internal waves play a key role in mixing the interior of the Southern Ocean.

Other regions with relatively large internal waves include the Hawaiian Ridge and the Gulf

Stream. A number of works have shown Hawaii to be a strong source of internal tides (e.g. *Alford and Whitmont* (2007)). We also observe internal wave intensification in the vicinity of the Gulf Stream. *Rainville* (2004) found that internal wave intensity in the North Pacific can be significantly enhanced on the coastal side of the Kuroshio. The Kuroshio has strong horizontal velocity gradients, and the corresponding increase in vertical vorticity creates a barrier that low frequency internal waves cannot cross (*Kunze*, 1985). We hypothesize the same process may be trapping internal waves on the coastal side of the Gulf Stream, resulting in the elevated internal wave variance.

Curiously, internal waves appear to be relatively weak over much of the subtropical Indian Ocean. The Southwest Indian Ridge is a prominent bathymetric feature in this region, and due to its roughness it is surprising that there is little or no enhanced internal wave energy.

The intensification of internal waves near the equator is intriguing. *Whalen et al.* (2012) estimates higher than average dissipation at the equator but acknowledges that this intensification could be a sampling artifact of features such as equatorial jets. We observe that internal waves are indeed more intense at the equator, lending credence to the notion of elevated dissipation observed by Whalen. There are also many other similarities between the global results presented by *Whalen et al.* (2012) and the internal wave intensity in Fig. 1.11.

There is no obvious seasonal cycle in the internal waves observed. This suggests that the internal waves arise from a fairly consistent forcing (at least on the time scale of months). *Alford and Zhao* (2007) used horizontal velocity observations from moorings to show a factor of two to three increase in wintertime near-inertial energy compared to summertime estimates. The observed wintertime intensification often resulted from intermittent events, rather than being consistently more energetic than the summertime. Our float ensemble should be capable of observing such intermittency due to the hourly temporal resolution and high percentage of time spent in the park-phase, yet generally we do not observe a seasonal dependence of the inertial peak. This is possibly because the float temperature technique used here is only capable of inferring vertical motions, thus skewing our results toward the steadier tidal signals rather than the predominantly horizontal motion of near-inertial waves.

1.5.2 Garrett-Munk Comparisons

Caution is required in making generalized conclusions about how the GM spectrum compares to the observed spectrum from this dataset. Floats are often deployed at scientifically interesting locations, thus potentially biasing the results and conclusions. The GM ideas were formulated using primarily mid-latitude data, while most of the floats in our ensemble are not at mid-latitude. Furthermore, a large portion of our mid-latitude observations were collected around Hawaii and the Gulf Stream, sites that are not representative of most of the ocean.

With these caveats noted, the mean of all OV_i/EV_i shown in Fig. 1.12 is slightly less than one (0.7), which is fairly close to what would be expected. This low value could at least partially be explained by the single depth measurements. The float data used here are all collected in the vicinity of a depth of 1000 m, thus making the modal structure of internal wave field impossible to determine. If 1000 m lies at, or near, one of the vertical modal nodes (primarily the low modes), then the displacement inferred by the floats could be a significant underestimate of the maximum displacements elsewhere in the water column.

Another source of error could be the latitudinal dependence of the GM spectral amplitude. There is no such dependency observed in the real-world spectra of internal waves (*Levine*, 2002). This could at least partially explain why the ratio of the observed spectrum to the GM spectrum appears to be so low (often an order of magnitude less than GM) at many high latitude locations, thus contributing to lowering the global average.

1.5.3 Effects of Local Bathymetry and Barotropic Tide

Results shown in Fig. 1.14 suggest that when floats are over smooth bathymetry and far above the seafloor (the upper left portion of the figure), they tend to observe relatively low amplitude internal wave fields. When the floats are over rougher bathymetry, and closer to the seafloor (lower right), internal wave variance increases dramatically. This result is analogous to Polzin's 1997 observations of diffusivity in the Brazil Basin (*Polzin et al.*, 1997), where diffusivity was dependent on proximity to the seafloor and seafloor roughness.

An analogous examination of the dependence of internal wave amplitude on both seafloor roughness and the strength of the barotropic tide (Fig. 1.15) also indicates a relationship between both bottom roughness and the barotropic tide. This dual dependency is clearest for the roughness bins less than 400 m, and the barotropic velocity bins less than 2 cm s^{-1} (where most bins have well over 100 individual park-phase estimates). Figs. 1.14 and 1.15 show that internal wave displacement is dependent on seafloor roughness, proximity to the seafloor, and forcing from the barotropic tide. It is striking and informative to observe the expected trends throughout this large dataset that covers such a diverse range of conditions.

1.5.4 Coastally-Trapped Waves

In addition to seamount trapped waves at the Amundsen Ridge (Section 1.3.2), we observe significant diurnal displacement at many locations poleward of 30^o. Most of the discernible diurnal peaks poleward of 30^o (see Fig. 1.16) occur near continental rises or other sloping bathymetry, suggesting that these diurnal waves are coastally trapped. We find little evidence of diurnal excitation in the pelagic ocean. While the seamount trapped waves discussed in Section 1.3.2 were fairly ubiquitous, the observations of coastally trapped waves in general are quite patchy. Fig. 1.17 highlights a region in the Southern Ocean, on the shelf between 75^oE and 104^oE that showed significant diurnal activity, but not much else in the surrounding area. While there is considerable uncertainty in the cause of such shelf intensification, we posit that the patchiness of the diurnal signal near coastal rises might be partially explained by sporadic wind events. Storms could provide the necessary energy to excite coastally trapped waves. Intermittent wind intensification could also explain why we observe significant diurnal energy at one location and no such intensification at other nearby sites.

1.6 Conclusions

The combination of quasi-Lagrangian drift trajectories, relatively high frequency sampling, and multi-year operating lifetimes make the iridium Argo floats a unique platform to observe internal waves. The float data are most instructive on global-scale internal wave behavior as demonstrated in Section 1.4. There is significant similarity between the direct observations of internal waves presented here and studies that employ mixing parameterizations (Section 1.5.1). The wide range of geographic and oceanic conditions encompassed by our work helps to further validate such parameterization methods.

The nature of the Argo program is global in its scope; however Section 1.3.2 demonstrates that internal waves on a finer scale can be investigated from data collected from an individual float. There are almost undoubtedly individual iridium floats that could contribute significant information to smaller regional studies of internal waves.

The gaps in spatial coverage will slowly be filled, as there is a steady supply of new iridium floats. As the coverage improves, so too will our ability to address the questions examined in this work. A complete global coverage would also open up many more lines of inquiry.

Acknowledgments

This work was generously supported by NOAA through the Joint Institute for the study of the atmosphere and ocean at the University of Washington, grant number NA17RJ1232 Task 2. The floats were all fabricated at the University of Washington from components purchased from Teledyne/Webb Research. We thank Dana Swift, Dale Ripley, Rick Rupan, and Greg Brusseau of the University of Washington for their superb skills in producing these high quality instruments.

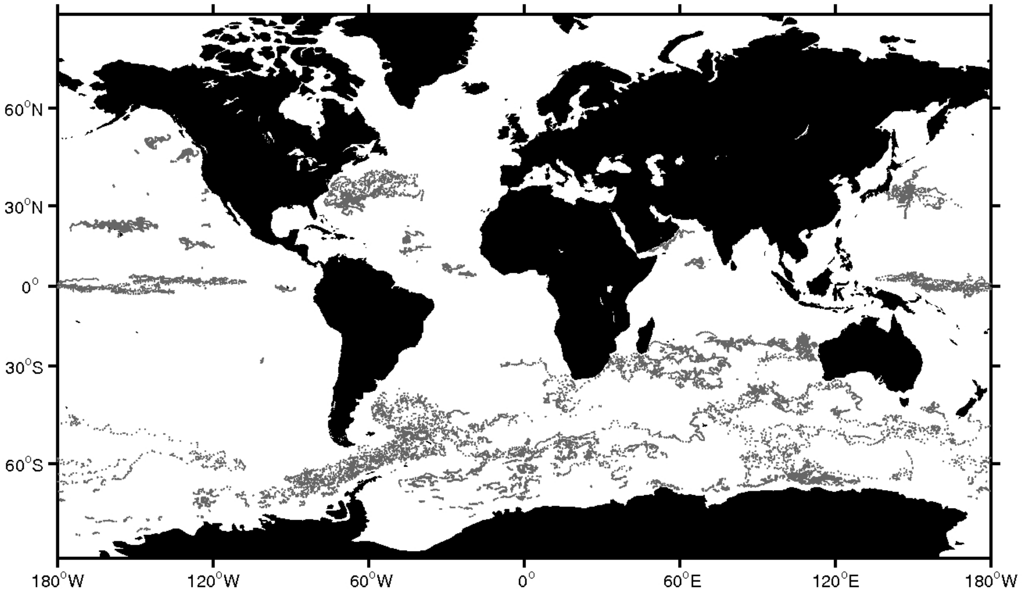

Figure 1.1: The surface locations of 194 UW-built profiling floats used in this study, collected between 2004 and 2013. Most floats were parked at a depth of 1000 m and profiled between a depth of 2000 m and the sea surface at approximately 10 day intervals.

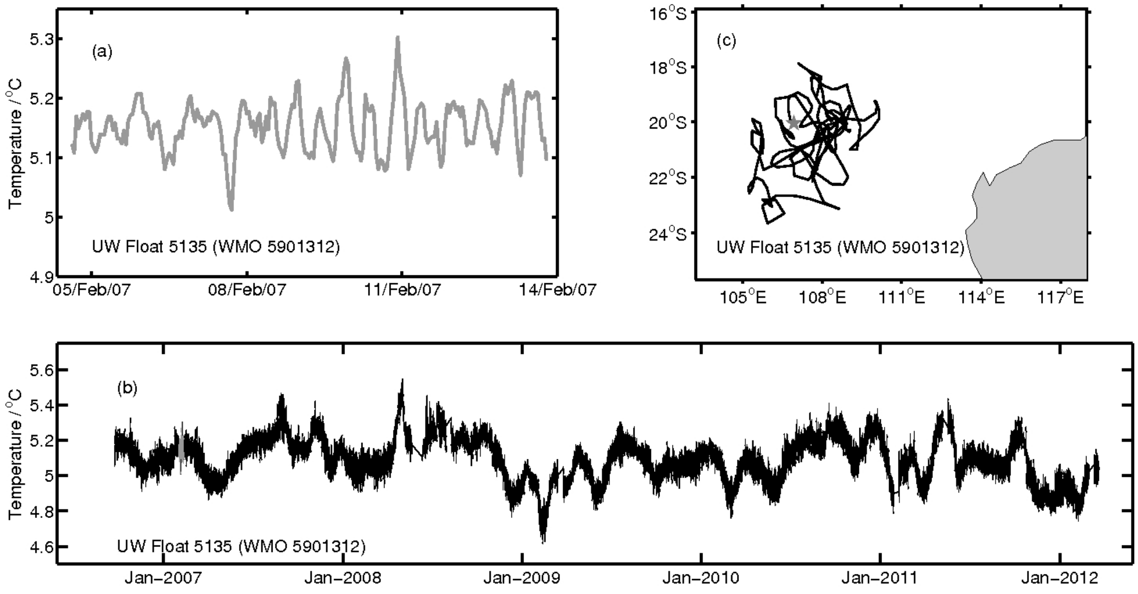

Figure 1.2: (a) The hourly temperature during a park-phase (cycle 21) of float 5135 (WMO 5901312), 04/02/2013-13/02/2013. (b) The park-phase temperature record for the entire deployment of UW float 5135 with the park-phase from panel (a) highlighted in early 2007. (c) The trajectory of float 5135 over its deployment. The shaded land mass on the east is the northwestern coast of Australia.

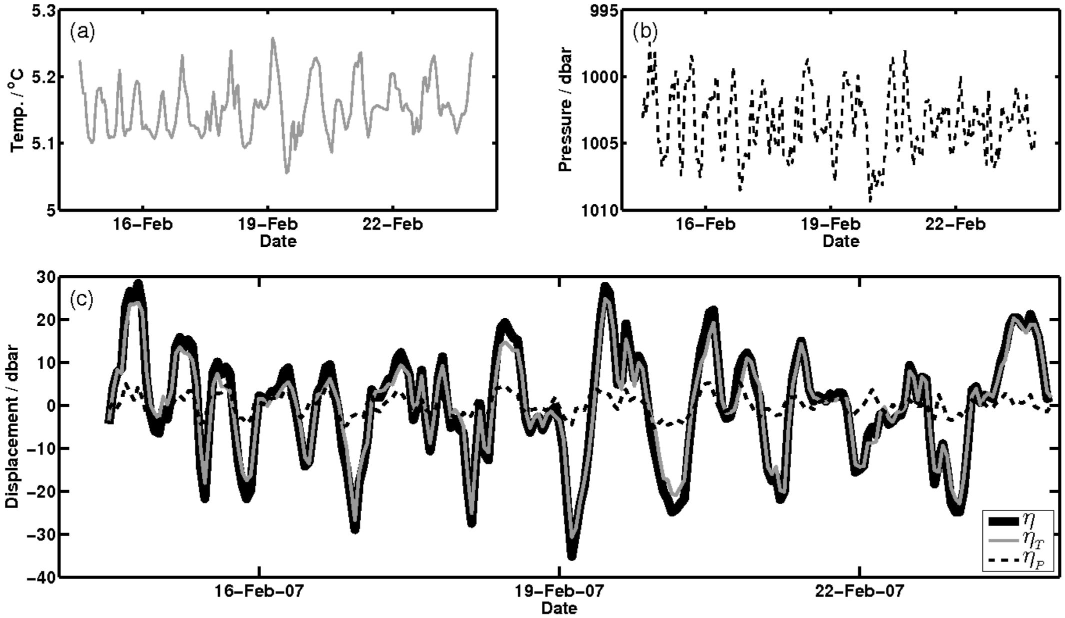

Figure 1.3: (a) Raw park-phase temperature during cycle 22 for Float 5135. (b) Raw park-phase pressure during cycle 22. (c) Processed isotherm displacement as seen by the float (grey), the float displacement (dashed), and the actual isotherm displacement (thick black) during the park-phase of cycle 22.

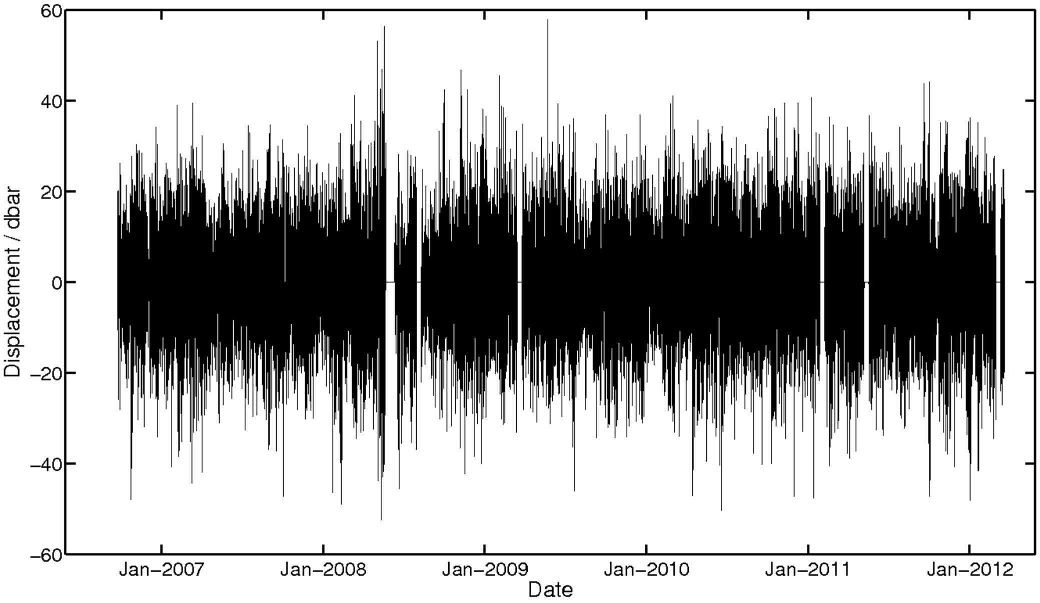

Figure 1.4: The synthesized time series of vertical internal wave displacement for float 5135, located in the Indian Ocean. The small gaps of data (zeros) correspond to park-phases where the vertical temperature profile was not linear enough to meet quality control (see Section 1.2.3).

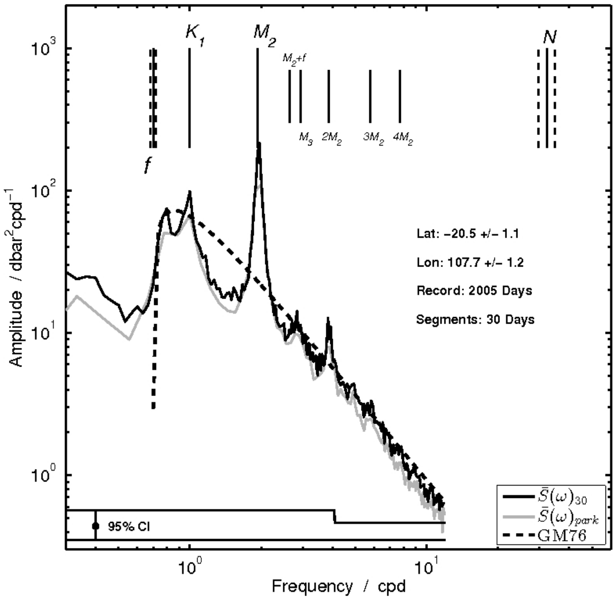

Figure 1.5: An example of the average power spectrum of displacement, $\overline{S}(\omega)$, from both 30-day segments (dark solid line) and park-phases (light solid line) for float 5135. The dashed curve is the GM76 expected spectral density calculated from Klymak's MATLAB toolbox. The light curve, $S(\omega)_{park}$, is the power spectrum averaged over the 9 day park-phase segments and shows that $S(\omega)_{30}$ is not severely distorted. The solid vertical lines above the spectrum indicated frequencies of note, such as the: diurnal (K_1), semidiurnal (M_2), buoyancy (N), inertial (f), and several harmonic frequencies. The dashed vertical lines indicate one standard deviation away from the average N and f, as these parameters can change over the float's deployment. Spectral density is averaged (smoothed) across three frequency bins for estimates beyond four cycles per day (which results in a tighter confidence interval as well). The range of the 95% confidence interval is shown on the bottom of the plot.

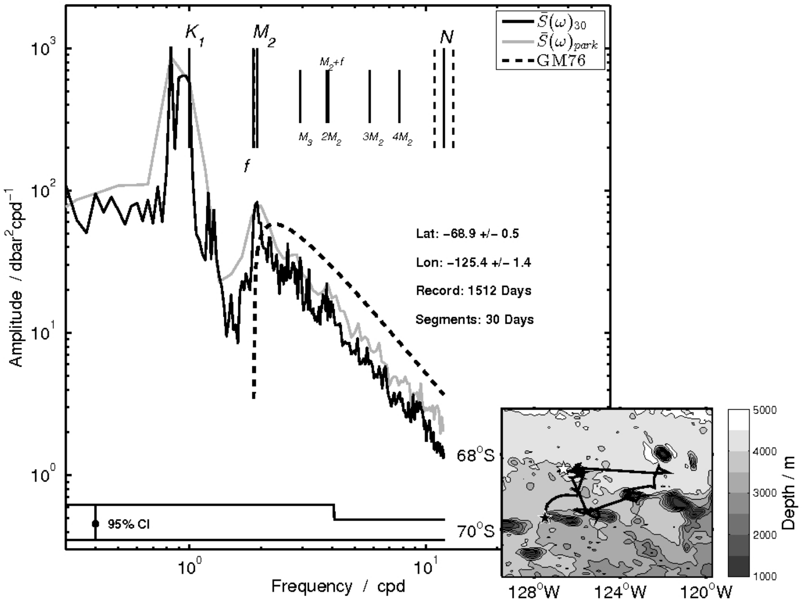

Figure 1.6: Identical to Fig. 1.5, but calculated for UW float 6097 (WMO 5902118), located in the Southern Ocean near the Amundsen Ridge. $S(\omega)_{park}$ is formulated from 5-day park-phases for this float. The lower right plot shows the surface locations of the float (the white star is the first profile and the black star is the final profile).

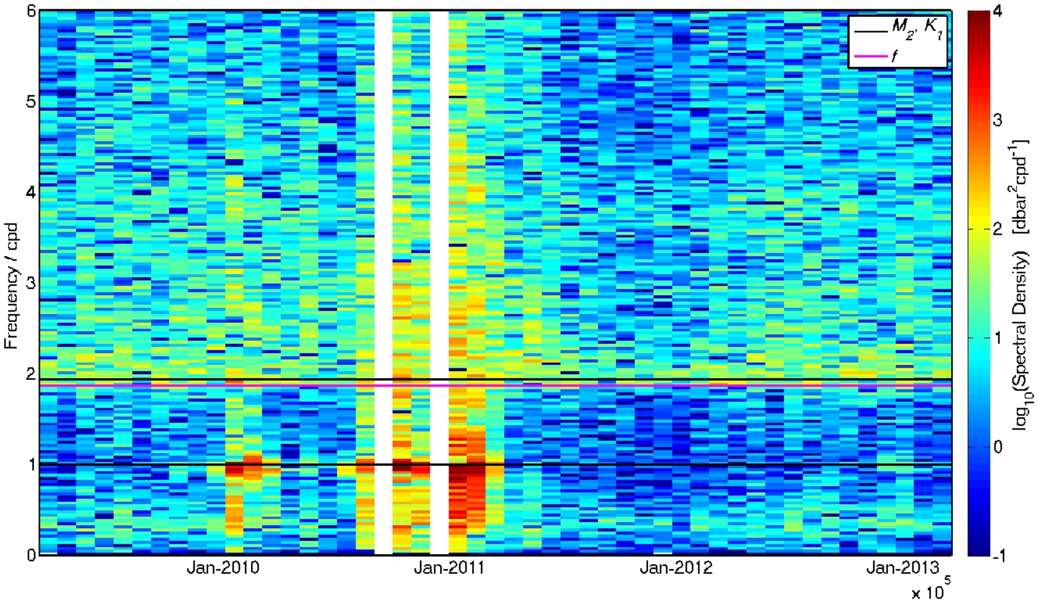

Figure 1.7: Plots the temporal evolution of the displacement power spectrum over the lifetime of float 6097. Each vertical section represents one power spectrum calculated from a 30-day segment. There are two gaps that did not have sufficient data that met quality control, and hence no power spectrum is calculated. The horizontal lines show frequencies of interest (M_2, K_1, and average inertial).

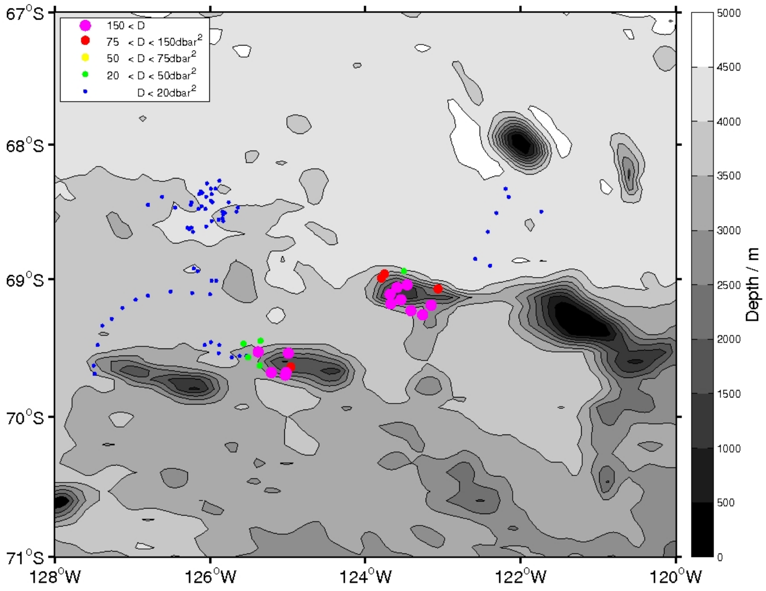

Figure 1.8: A spatial plot of the diurnal variance, D, of each park-phase recorded by float 6097. Each point on the map depicts the diurnal variance for a single park-phase during the ice-free periods (locations are not known precisely when the float is under sea ice). Variance has been classified by different variance bins, indicated by the different sized/colored dots. The filled contours show bathymetry data from ETOPO1.

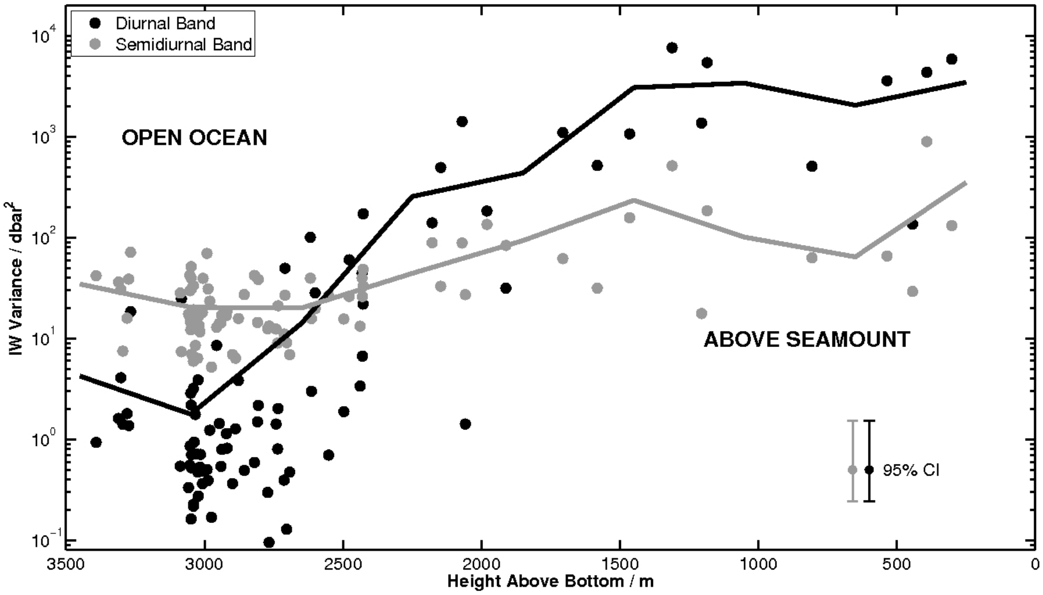

Figure 1.9: The semi-diurnal (grey) and the diurnal (black) variance as a function of height above the bottom. Each point is an estimate from one park-phase of float 6097. In open ocean depths (left), diurnal variance is very low. As the seafloor depth decreases and some measurements are from the flanks of the seamounts, diurnal variance increases by several orders of magnitude. The semi-diurnal variance also increases, albeit less dramatically. Periods when the float is under seasonal sea ice are not plotted, as the location and depth are not precisely known.

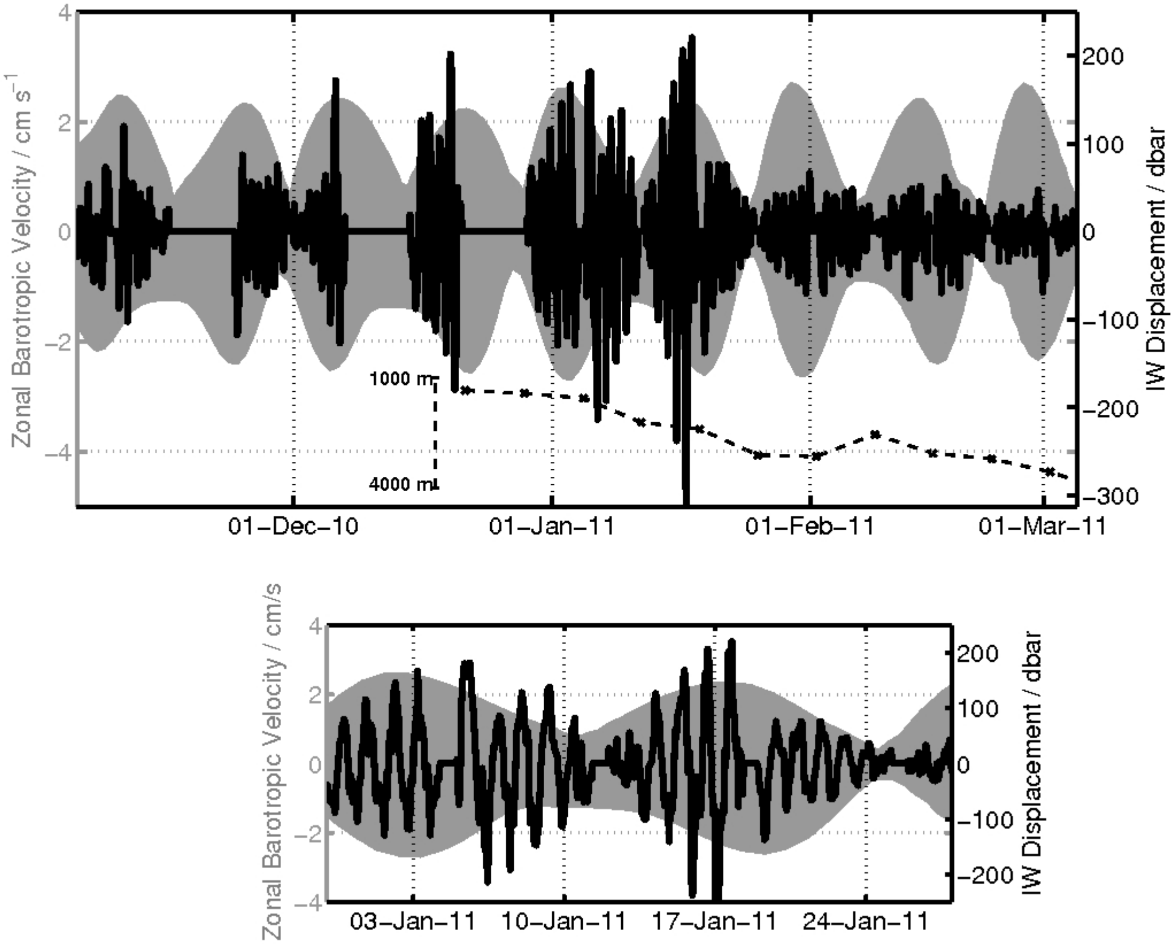

Figure 1.10: Top: The spring neap envelope of the barotropic zonal velocity (grey shading) and the internal wave displacement (black line) observed by float 6097 from November, 2010, to March, 2011. The dashed line plots seafloor depth, but only after mid-December as the float was ice-covered prior to this (preventing a satellite fix on location). Barotropic zonal velocity was obtained from the TPXO 7.2 tidal model. Several large gaps are due to quality control criteria being violated. Note the two different scales for the barotropic tide (left), and the internal wave displacement (right). Bottom: Same as above plot, but zoomed in on the month of January, where the diurnal motion is exceptionally large and dominates the displacement signal.

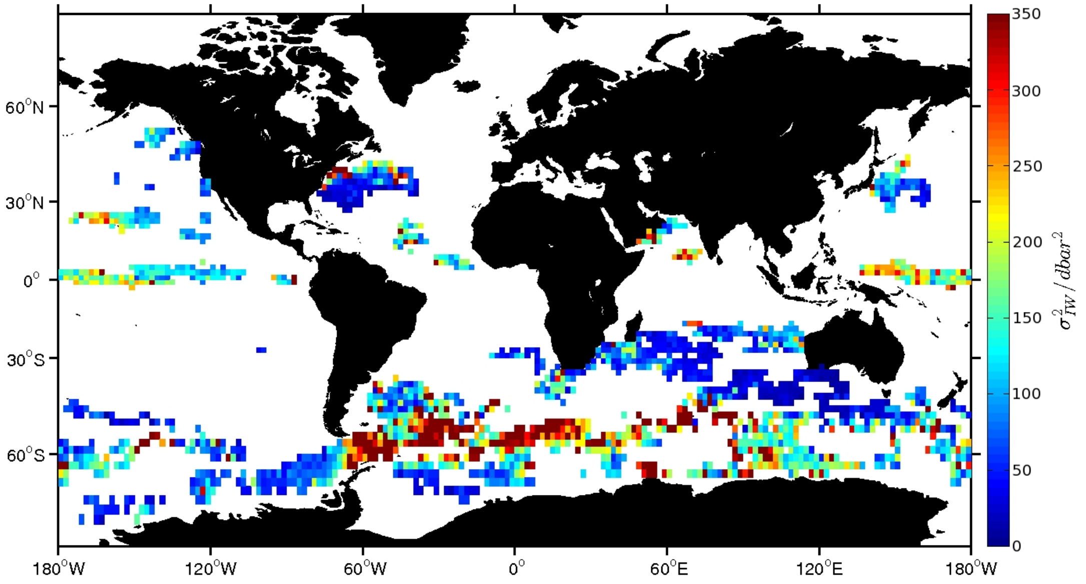

Figure 1.11: Estimates of internal gravity wave vertical displacement variance from the 194 profiling floats used in this study. Values are averaged into 2^o by 2^o bins.

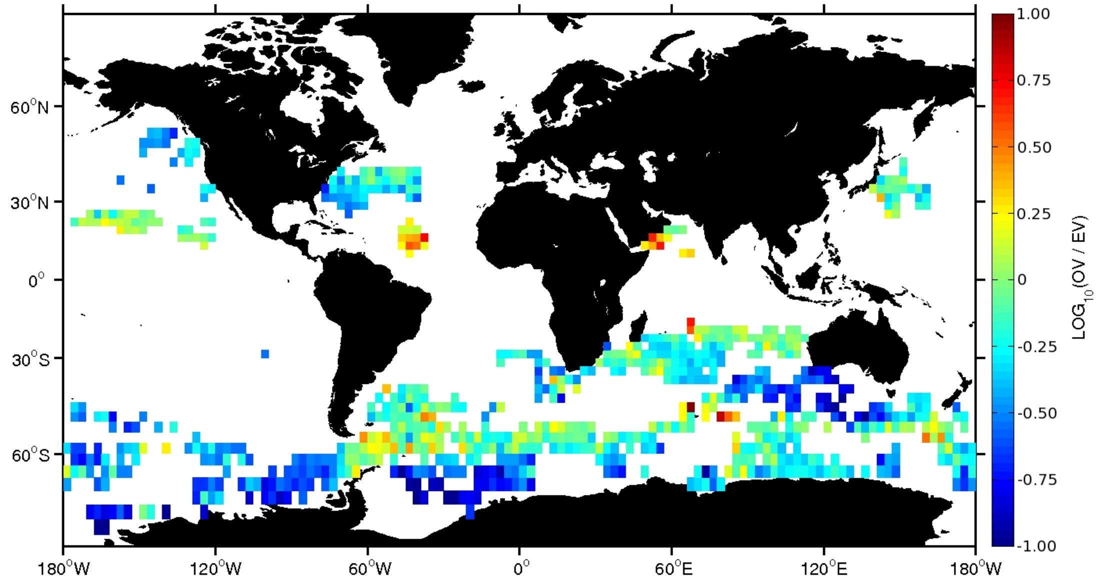

Figure 1.12: The ratio of the observed spectrum and the GM76 spectrum between 3 cpd and 6 cpd. Values are averaged into 3^o by 3^o bins.

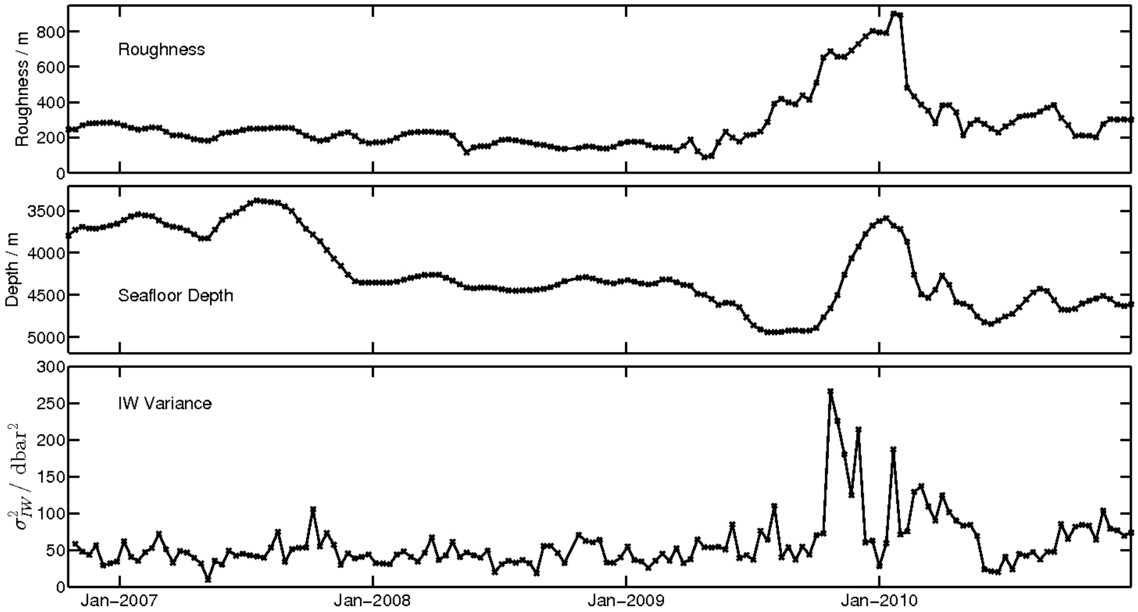

Figure 1.13: Top plot: The weighted standard deviation of the seafloor depth along the path of UW float 5061 (WMO 1900413). Middle plot: The weighted average of seafloor depth. Bottom plot: The internal wave variance. The spike in all the quantities around January 2010, occurs when float 5061 passed over the Southwest Indian Ridge.

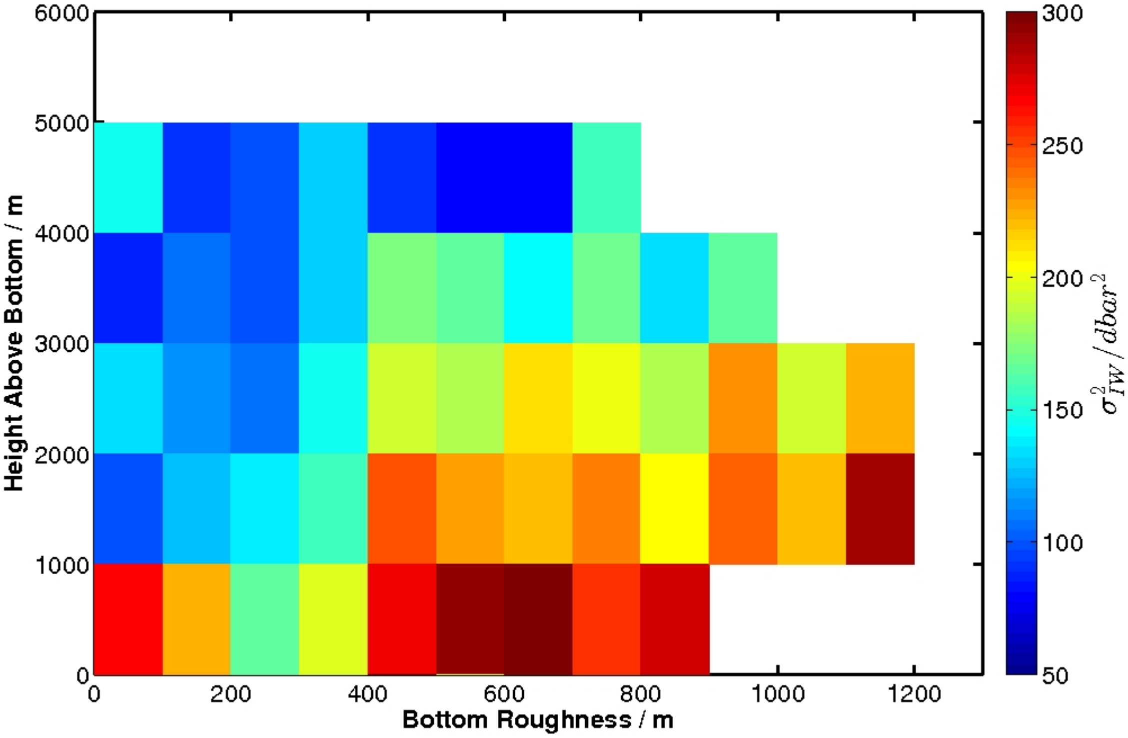

Figure 1.14: The internal wave variance plotted against both bottom depth and parameterized roughness. All bins contain at least 20 estimates, however, the bins between 2000 - 5000 m depth and 0 - 400 m roughness contain most of the variance estimates. The strong internal waves observed at < 1000 m above the bottom and < 200 m bottom roughness are intriguing. However, there are less than 100 measurements in each bin (higher bin counts are in the hundreds or thousands).

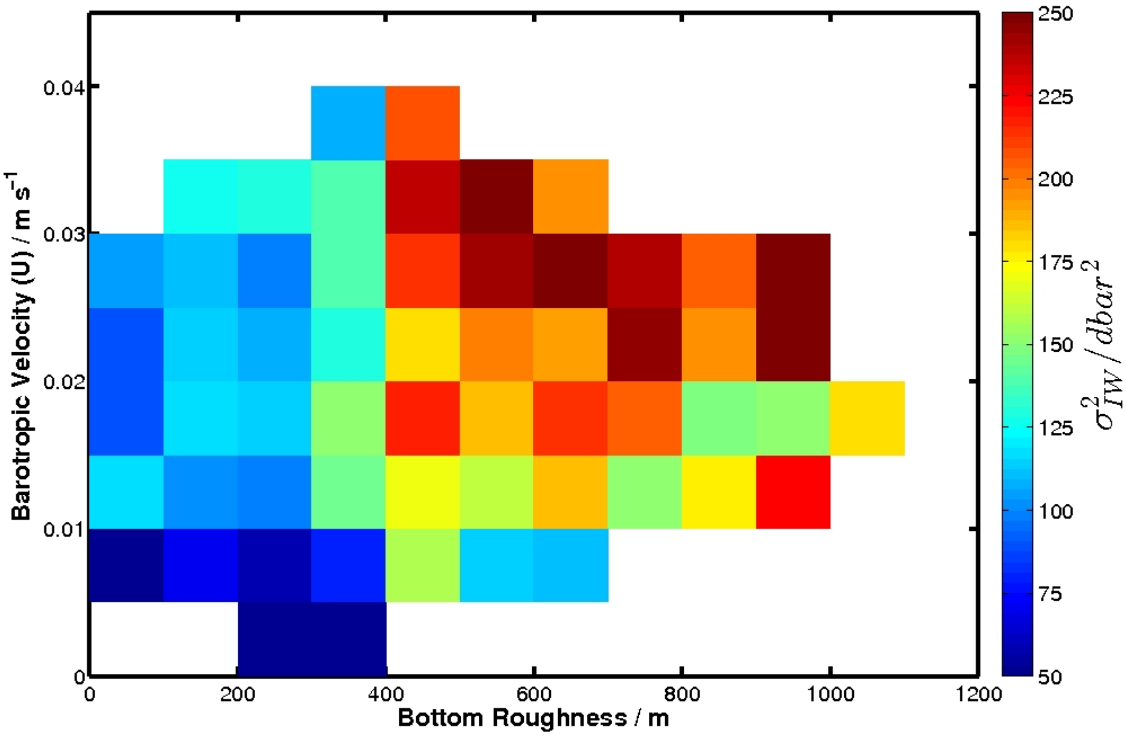

Figure 1.15: The internal wave variance plotted against both bottom depth and parameterized roughness. All bins contain at least 20 estimates, however, the bins between 0 - 600 m on the horizontal axis and 0 - 0.025 m s^{-1} on the vertical axis contain most of the estimates.

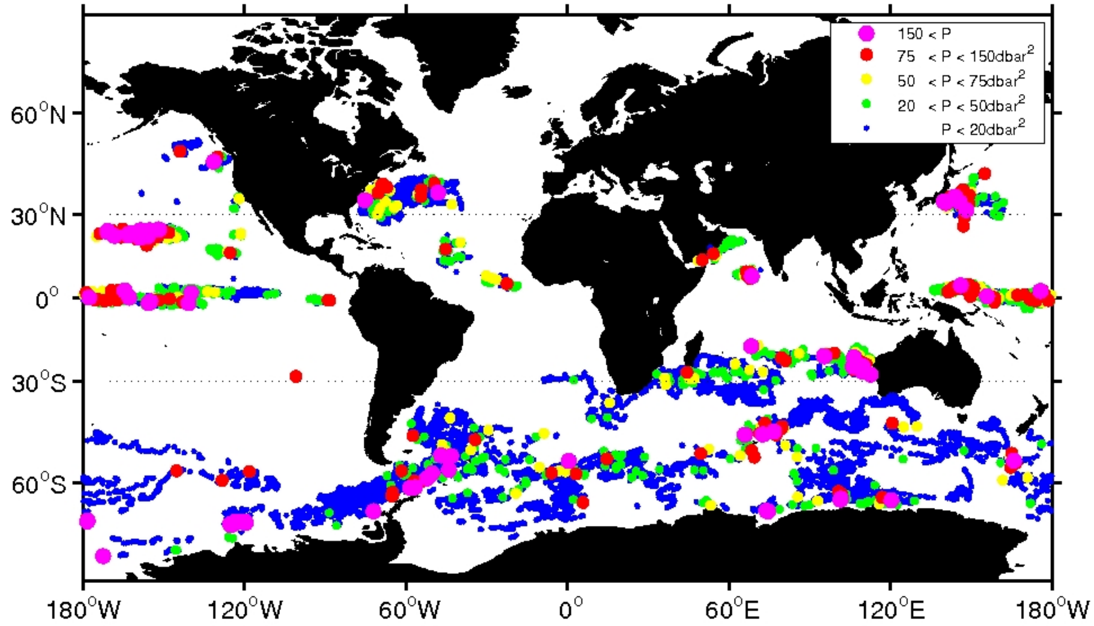

Figure 1.16: A spatial plot of the diurnal prominence, P, (see Section 1.4.6 for definition) of each park-phase for each float in the ensemble used here. Variance has been classified by different variance bins, indicated by the different sized/colored dots. The turning latitudes for diurnal waves are indicated by the black dotted lines. Park-phases occurring when a float is under ice are not included, as their location is not accurately known.

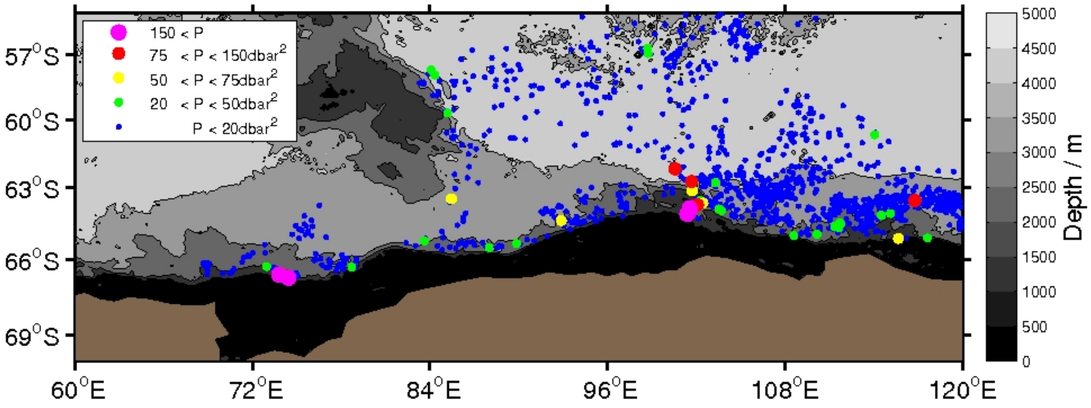

Figure 1.17: Similar to Fig. 1.16, but focused on a region of the Southern Ocean (the southern Indian Ocean). The shaded contours indicate depth from ETOPO1. The brown shaded region is land.

Chapter 2

PROFILING FLOAT-BASED OBSERVATIONS OF NET RESPIRATION BENEATH THE MIXED LAYER

CITATION

*Hennon, T. D., S. C. Riser, and S. Mecking (2016), Profiling float-based observations of net respiration beneath the mixed layer, *Global Biogeochem. Cycles*, **30**, doi:10.1002/2016GB005380.

[*The following is identical to the GBC article, but with the addition of Section 2.4.4 and Figs. 2.9 and 2.10 to augment analysis.]

Abstract

We employ profiling floats with dissolved oxygen sensors to observe *in situ* temporal oxygen evolution below the mixed layer, allowing us to characterize net respiration of organic carbon in eight distinct regions over the globe. Export and export efficiency are generally high in locations with strong seasonal variability, and low in locations of weak seasonality. Vertically integrated respiration is weakly, yet significantly, correlated with remote observations of chlorophyll, net primary production, and planktonic community size structure. These correlations suggest that regimes of high net primary production and large phytoplankton fuel elevated respiration at depth. Several regions of float-based observations intersect with sites of other detailed observations (e.g. Hawaii and Sargasso Sea), which allows us to compare our results to independent studies. We find that there is good agreement among export production estimates at highly seasonal locations, and that float-based observations may be biased low at weakly seasonal locations occurring most often at low latitudes. We posit that the reason for the low-latitude discrepancy is the relative steady-state of oxygen concentration caused by weak seasonality and shallow wintertime mixed layer depths.

2.1 Introduction

The oceans are an important part of the global carbon cycle and act as a significant sink to atmospheric CO_2 (*Sarmiento and Gruber*, 2002; *Sabine et al.*, 2004) as planktonic communities transform carbon between organic and inorganic forms, and physical circulation acts to redistribute carbon inventory (*Hansell and Carlson*, 1998). Remote sensing has been used since the 1970s to characterize the net primary production (NPP) at the surface of the ocean (*Hovis et al.*, 1980; Platt and Sathyendranath, 1988; *Platt et al.*, 1991). The satellite observations have revealed that marine phytoplankton comprise approximately half of NPP globally (*Field et al.*, 1998).

Ultimately, a fraction of the organic matter formed at the surface sinks beneath the observational range of satellites (the first few tens of meters (*Gordon and McCluney*, 1975)), with the potential to undergo long-term sequestration (*Eppley and Peterson*, 1979). This process has inefficiencies. As organic matter sinks from the surface, it is consumed by heterotrophs, and a large fraction is converted back to inorganic carbon (remineralized) via respiration before it reaches the abyssal ocean. *Martin et al.* (1987) characterized this depth-dependent carbon flux, and formulated the well-known Martin curve, a power function that describes the decrease in carbon flux with increasing depth.

There are many factors that influence the fraction of NPP that eventually escapes the euphotic zone, a ratio referred to as the f-ratio. Models, verified by *in situ* data, indicate that the $f-$ratio is affected by temperature (and latitude) dependent growth rates (*Laws et al.*, 2000). Planktonic community size structure is an important control on carbon export efficiency (*Henson et al.*, 2012; *Michaels and Silver*, 1988), as particle size distribution affects sinking rate. Larger particulate matter generally sinks faster (Stokes' law), and is exported from the euphotic zone more readily. Several studies have parameterized community structure based on remote chlorophyll and backscatter observations (*Kostadinov et al.*, 2009; *Hirata et al.*, 2011), which we later employ in comparison to our observations. Particulate matter can also aggregate during blooms, enhancing export (*Martin et al.*, 2011).

In recent years autonomous profiling floats have been used to characterize net community production (NCP), defined as NPP minus heterotrophic respiration. *Riser and Johnson* (2008) used data from two such floats in the subtropical Pacific that observed oxygen accumulation in the shallow oxygen maximum (< 100 dbar) and determined that the elevated oxygen concentration was due to autotrophic production outpacing respiration (positive NCP). *Martz et al.* (2008) used 18 floats with dissolved oxygen sensors to characterize the vertical structure of NCP (with an emphasis on 50 to 200 dbar) in the sub-polar South Pacific and observed that remineralization exhibited a decrease with depth consistent with the Martin curve. Since 2008 (year of publication of the aforementioned Martz et al. and Riser and Johnson studies) the global coverage of profiling floats equipped with dissolved oxygen sensors has greatly expanded. The present work utilizes this increase in data volume to investigate the regional variability of ocean metabolism and carbon cycling.

Our aim is to estimate net respiration, referred to here as R, of heterotrophic communities below the mixed layer. R is not exactly equivalent to the carbon exported from the euphotic zone to the abyssal ocean, but rather an inefficiency in this transfer as the remineralized carbon can be ventilated back into the atmosphere by the annual formation of the deep wintertime mixed layer. Consequently, it is an important control on the fraction of NPP that is ultimately sequestered into the deep ocean for decades or longer. In fact, most of the export flux leaving the upper ocean is remineralized before it reaches the deep ocean (*Buesseler et al.*, 2007; *Henson et al.*, 2012). Therefore, although we have no direct observations of carbon export, we can ascertain reasonable constraints on carbon flux out of the upper $\sim$ 100 m and on export efficiency. We expect that R will be larger in regions of greater surface productivity, so we also make use of remote observations of surface production to identify possible correlations.

2.2 Methods

2.2.1 Float Data

We use data from 112 profiling floats equipped with Aanderaa Optode sensors (fabricated at the University of Washington; http://runt.ocean.washington.edu/o2/) to characterize sub-mixed layer oxygen evolution. We avoid analysis in the mixed layer because, while the Optode sensors are stable over time (addressed further in Section 2.2.2), there is a large factory calibration bias (*Gruber et al.*, 2007). The bias of approximately 10-40 μmol kg^{-1} leads to prohibitively high error in air-sea gas exchange calculations. *Takeshita et al.* (2013) introduced a method using climatology to calibrate Optodes to $\sim$ 3% error, and Robert Drucker of the University of Washington (unpublished) has used a similar method that may reduce error to about 3 μmol kg^{-1} ($\sim$ 1%). Even with these improvements, a 3 μmol kg^{-1} error is still only sufficient to be confident in the sign of the air-sea gas exchange in most regions and leads to very large errors in mixed layer NCP estimates. Newer floats sample atmospheric oxygen, which allows calibration accurate enough to characterize NCP in the mixed layer (*Bushinsky and Emerson*, 2013). However, the floats with this ability are currently limited in both number and breadth of spatial coverage.

Our estimates of R are more reliable if analysis is limited to depths below the mixed layer, where tracers are isolated from direct surface forcing. Here, the temporal evolution of oxygen is more indicative of biological processes, and constraining our analysis to below the mixed layer takes advantage of the strength of the Optodes (precision and temporal stability), and eliminates the weaknesses (calibration bias) by focusing on the time rate-of-change of oxygen.

2.2.2 Calculating Net Respiration

In the methods used here, the float-based oxygen data are linearly interpolated to a pressure grid spaced by 10 dbar from the surface to 2,000 dbar and a temporal grid spaced by five days, beginning at the first profile of a float and ending at the last. The choice of the pressure grid is designed to roughly reflect the oxygen sampling scheme of the floats in the upper ocean, while the temporal grid represents the floats' nominal 5 to 10 day cycle. The interpolated data are broken into temporal segments that span approximately one year, starting at one winter's maximum mixed layer depth and ending at the maximum mixed layer of the following year. This constitutes one float-year of data. We use a density threshold of 0.125 kg m^{-3} or temperature threshold of 0.5 ^{o}C, whichever is reached first, to estimate mixed layer depth (e.g. *Monterey and Levitus* (1997)).

As mentioned previously, we use the temporal evolution of oxygen to characterize biological influences on oxygen concentration. Autotrophic and heterotrophic processes are not the only factors that alter oxygen, however, as physical mechanisms also play a role, such that:

$$\frac{d[O_2]}{dt} = 1.45 \times NCP - \vec{u} \cdot \nabla[O_2] + \nabla \cdot (\kappa \nabla[O_2]) \tag{2.1}$$

where $\vec{u}$ is the three dimensional velocity vector, and κ is the turbulent diffusivity tensor. We scale NCP by the Redfield ratio ($1.45\ O_2 : 1\ C$) to convert between organic carbon and O_2 (*Anderson and Sarmiento*, 1994). Surface flux terms are neglected because our analysis is constrained to beneath the mixed layer and 70 dbar (whichever is greater). We choose to omit data from the mixed layer for reasons outlined in Section 2.2.1. The 70 dbar threshold is chosen because it is roughly at the compensation depth (*Najjar and Keeling* (1997); 50 - 100 m), where respiration begins to outpace photosynthesis. We make the assumption that floats are equally likely to drift through positive and negative oxygen gradients, and given a large enough sample size, oxygen variability caused by water mass changes ($\vec{u} \cdot \nabla[O_2]$ and $\nabla \cdot (\kappa[O_2])$) tend to offset. We also assume that vertical diffusion is small (*Ledwell et al.*, 1993), and will play a minor role in oxygen evolution. Therefore, we use the simplification that oxygen evolution is dependent on NCP alone (revisited in Section 3.4). Since our analysis is constrained to depths where it is common for respiration to outpace photosynthesis, we frame our results in terms of net respiration, R (where $R = -1 \times NCP$), such that:

$$R = -\frac{1}{1.45} \times \frac{d[O_2]}{dt} \tag{2.2}$$

Here positive R represents conditions of net destruction of organic matter via respiration. To determine R for a given float-year, we first use least squares linear regression to find the best fit to the temporal evolution of oxygen concentration along isobars (Fig. 2.1). The annual time rate-of-change of oxygen (d[O_2]/dt) is defined as the slope of this linear regression (Fig. 2.2). In contrast to the constant temporal bounds used by *Martz et al.* (2008) (December to April), we calculate the respiration using the entire time that an isobar is below the mixed layer (see horizontal lines in Fig. 2.1), so long as there are at least 100 uninterrupted days. This variable temporal domain allows us to utilize the greatest possible number of available measurements.

Attempts to analyze oxygen trends on sub-annual time scales (e.g. months or seasons) did not reveal any obvious differences in the time-rate-of-change of oxygen, unlike the signals with an annual period observed by *Najjar and Keeling* (1997). We calculate annual respiration rates (in μmol C kg^{-1} yr^{-1}) from segments that are often less than one year, and thus may expect some bias arising from extrapolation. However, due to the relative temporal consistency we observe in d[O_2]/dt, and because the temporal segments used often constitute a large fraction of the float-year, we assume that these biases will be small.

This method yields vertical profiles of d[O]$_2$/dt for each float-year for all floats used in this study. Although the analysis presented here uses pressure surfaces as the vertical coordinate, our results are not highly sensitive to the choice of a pressure or density coordinate system, likely because isopycnal depth is not highly variable along the path of most floats.

We make the idealization that Optode sensors are stable in time, and d[O]$_2$/dt is not influenced by instrument drift. Naturally, there is some degree of instrument drift, but the effects are presumed minor. Optodes have been found to drift $\sim 0.3\%$ per year [Bushinsky S., et al., Accurate oxygen measurements on modified Argo floats using in situ air calibrations, under review in *Limnology and Oceanography: Methods*, 2016], which will typically correspond to 1 μmol O_2 $kg^{-1}yr^{-1}$ or less. We often see temporal O_2 changes of 10-20 μmol $kg^{-1}yr^{-1}$ (Fig. 2.2), so a drift on the order of 0.3% will not adversely affect our findings or interpretations.

Grouping float-years by region allows us to diagnose both the variability and ensemble average of $d[O]_2/dt$ in areas with an abundance of floats equipped with Optodes (see example in Fig. 2.3). Before calculating the ensemble mean, we visually inspect the data and remove float-years in which sensors malfunctioned or the float obviously crossed a strong front (e.g. crossing the Gulf Stream in the Sargasso Sea), as these events can introduce extraordinarily strong oxygen signals that do not correspond to any biological processes. Regional results (Fig. 2.4) are discussed in Section 2.3.1.

We also calculate the depth-integrated respiration, R_{sub} for each float-year, such that:

$$R_{sub} = \int_{70dbar}^{P_{max}} R(p)dp \tag{2.3}$$

where $R(p)$ is the pressure dependent net respiration (R). As mentioned previously, we choose 70 dbar as the lower limit on pressure because it roughly coincides with the compensation depth. The upper limit of integration, P_{max}, varies regionally, and is the point at which the mean respiration rates reach zero (e.g. ~500 dbar in Fig. 2.3). We do not integrate beyond P_{max} because $R(p)$ is generally indistinguishable from zero at pressures greater than P_{max}. Similar to $R(p)$, R_{sub} is an extrapolation to an annual depth-integrated respiration rate based on partial temporal coverage of the float-year.

2.2.3 Correlation with surface variables

The depth profiles of R (Fig. 2.4) suggest a high degree of spatial variability in subsurface respiration. Next, we aim to examine several surface variables and how they may be related to subsurface respiration. The surface datasets examined are:

1. Chlorophyll *a*, hereafter *Chl* (satellite observations of chlorophyll concentration from

Moderate-resolution Imaging Spectroradiometer (MODIS); *Esaias et al.* (1998)).

2. Community structure, hereafter ξ (*Kostadinov et al.* (2009); based on satellite observations of ocean color. ξ describes the particle size distribution; lower values represent communities with larger particles, and higher values represent communities with smaller particles).

3. Vertically-generalized production model, hereafter $VGPM$; (*Behrenfeld and Falkowski* (1997), a parameterized estimate of NPP, primarily based on remote observations of chlorophyll).

4. Carbon-based production model, hereafter $CbPM$ (*Westberry et al.* (2008); Similar to $VGPM$, but this parameterization of NPP also uses remote observations of backscatter to estimate planktonic carbon content.)

For each float-year, R_{sub} is compared with the surface variables over the same time period (Fig. 2.5). To make these comparisons, we average the surface variables both temporally and spatially. We take the mean of all surface data within 100 km of the float at each monthly time bin, and then use the monthly means to calculate an average over the entire float year (and convert to an annual rate, in the case of the $VGPM$ and $CbPM$ NPP data). Using 100 km as a threshold effectively creates an area of averaging that is 200 km in diameter. This is slightly larger than the typical mesoscale length scale (~100 km), which smoothes some of the variability caused by the mesoscale field without being so large that it includes environments far from the domain of the float.

We remove the lower and upper 1% of both remote observations and float data before calculating correlation coefficients (treating these observations as outliers).

2.2.4 Export production and efficiency

To estimate the export efficiency ($f-$ratio) in the different regions examined in this study, we couple our *in situ* observations of R_{sub} with satellite measurements of NPP. We use the $VGPM$ estimate of NPP since it is better correlated to our respiration data than the $CbPM$ model (Fig. 2.5). We use the depth integrated respiration, R_{sub}, as a proxy for the export flux of organic matter at 70 m. This estimate of export flux is likely to be a lower bound of the true carbon flux (i.e. $R_{sub} \leq$ export), because almost certainly some (small) fraction of the exported organic matter will pass below P_{max} (*Buesseler et al.*, 2007) before being remineralized. The $f-$ratio is defined as:

$$f - ratio = \frac{NCP}{NPP}. \tag{2.4}$$

where we treat NCP as equivalent to the export of organic matter at 70 m (assuming steady-state). Our float-based estimate of the export efficiency, f_F, is thus defined as:

$$f_F = \frac{R_{sub}}{NPP_{vgpm}} \tag{2.5}$$

where R_{sub} is defined as in Eq. 2.3, and NPP_{vgpm} is the monthly $VGPM$ parameterization of remote observations (*Behrenfeld and Falkowski*, 1997). Each float-year yields a single estimate of f_F by combining the measured R_{sub} and mean NPP_{vgpm} over that time span (NPP_{vgpm} is averaged in the same manner as in Section 2.2.3). Since we assume that R_{sub} is a lower bound for the carbon exported out of the euphotic zone, it follows that f_F is a lower bound on the true $f-$ratio.

To construct a standard by which to compare our observations, we also calculate the $f-$ratio using two independent parameterizations. *Dunne et al* (2005) used temperature, NPP, and the euphotic zone depth (Z_{eu}) to parameterize the $f-$ratio, hereafter f_D, as:

$$f_D = -0.0101^oC^{-1} \times T + 0.0683 \times ln(NPP/Z_{eu}) + 0.419. \tag{2.6}$$

Here we set Z_{eu} as a constant (100 m), use NPP_{vgpm} as the primary production term, and take T to be the monthly average of the corresponding uppermost temperature measurements from the float profiles (usually ∼5 dbar). *Henson et al.* (2011) used *Laws et al.* (2000)

observations of temperature and export efficiency to formulate a temperature-only based parameterization of the $f-$ratio, hereafter f_L, as:

$$f_L = 0.62 - (0.02 \times T), \tag{2.7}$$

where we define T as in Eq. 2.6. We use the monthly estimates of NPP_{vgpm} and T to calculate f_L and f_D for each month.

As with the $f-$ratio, we would like to also have a benchmark by which to compare the values of R_{sub} (our proxy for export). We calculate two estimates of the export production, E_D (*Dunne et al*, 2005), and E_L (*Laws et al.*, 2000):

$$E_D = NPP_{vgpm} \times f_D \tag{2.8}$$

$$E_L = NPP_{vgpm} \times f_L \tag{2.9}$$

where we use the monthly estimates of NPP_{vgpm}, f_D, and f_L. Results of calculations using Eqs. 2.5-2.9 are presented in Section 2.3.3.

2.2.5 Comments on Methods

The simplifications leading from Eq. 2.1 to Eq. 2.2 are necessary due to the uncertainties in the advective and diffusive terms. In most of the regions we examine, this is a reasonable approximation given that the advective-diffusive terms are expected to be small and we see robust signals in d[O_2]/dt. However, in weakly seasonal locations (e.g. low latitude), where the magnitude of the advective-diffusive terms are comparable to d[O_2]/dt, Eq. 2.2 may be insufficient to determine the respiration. Weakly seasonal locations generally have little difference between summertime and wintertime mixed layer depths, and biological production tends to be relatively consistent with time (*Behrenfeld and Falkowski*, 1997). These factors lead to a relatively steady oxygen concentration (d[O_2]/dt ~ 0), and using Eq. 2.2 would suggest negligible respiration, however, in these regions the advective-diffusive terms are actually offsetting respiration. In contrast, regions with higher seasonality in physical and biological processes (e.g. high latitude) show strong signals in d[O_2]/dt and Eq. 2.2 is likely a reasonable assumption. The performance of our methods will be further evaluated in Section 2.4.3 where we contrast our observations to past results.

2.3 Results

2.3.1 Regional Respiration Profiles

We estimate R in eight distinct regions globally, ranging from the North Pacific to the Southern Ocean (Fig. 2.4). All locations have at least 16 float-years of data (with a maximum of 34 at Hawaii), providing a reasonable statistical sample size by which to evaluate the ensemble behavior. The 95% confidence intervals (assuming Gaussian distribution) show that mean vertical profiles of R are generally distinct from zero in the upper ocean. The vertical structure and magnitude of R is significantly variable across different regions. High latitudes and locations where the mixed layer undergoes drastic seasonal changes tend to have much stronger respiration signals. Conversely, some subtropical sites (Hawaii and Central Indian Ocean) exhibit negligible respiration. In Section 3.4 we discuss these results and their significance further.

2.3.2 Correlations between R_{sub} and surface variables

There are weak, but significant (p-value < 0.05), correlations between R_{sub} and the remote estimates of Chl and $VGPM$, while R_{sub} is significantly anti-correlated with ξ and not correlated with $CbPM$ (Fig. 2.5).

As Chl and $VGPM$ rise, so does R_{sub} which suggests, as one would expect, that as more organic matter is created at the surface, more sinks below the euphotic zone, resulting in greater heterotrophic respiration and remineralization. The negative correlation between ξ and R_{sub} may be a result of larger phytoplankton sinking out of the euphotic zone more readily (less nutrient recycling), fueling greater respiration at depth.

It is somewhat difficult to disentangle these results, as all the surface variables are highly correlated with one another since they share the same underlying data (remote observations of color and backscatter), but our results suggest that more productive regions fuel greater respiration at depth. There could be significant noise introduced by errors in yearly estimates of R_{sub}. Remote observations are well-known to have significant error (*Hooker and McClain*, 2000). Thus, there may be a substantial amount of variance in R_{sub} left unexplained by surface processes, as there is only a weak correlation. This underscores the importance of collecting *in situ* subsurface measurements, as satellite observations only offer a narrow window into the full complexities of carbon cycling.

2.3.3 Export and export efficiency

Our regional calculations of export flux (Eq. 2.3) and the $f-$ratio (Eq. 2.5) are summarized in Table 1. It bears repeating that we expect these estimates to be lower bounds of the $f-$ratio and export production, as elucidated in Section 2.2.4. The float observations reveal significant variability in export efficiency (Fig. 2.6, yellow bars) and export (Fig. 2.7, yellow bars) across the world ocean. At mid- to high-latitude, the integrated respiration (our proxy for export) and $f-$ratio values are generally higher, while in some subtropical regions (Hawaii, and Central Indian Ocean) we find essentially no respiration export below the compensation depth (assumed 70 m). We also contrast these observations with parameterizations of the $f-$ratio (f_D, Eq. 2.6; f_L, Eq. 2.7) and export (E_D, Eq. 2.8; E_L, Eq. 2.9), shown in Figs. 2.6 and 2.7, respectively.

The parameterizations display the same trend as our observations; values of export and export efficiency are generally higher at high-latitude, while low nearer the tropics. There are several regions of significant difference, however. For example, the Sargasso Sea float observations of the $f-$ratio and export are higher than the parameterizations. This disagreement could arise from several issues.

As stated in Section 2.2.4, we expect our float-based estimates to be lower bounds of the true values of the f-ratio and export. This suggests that E_D and/or E_L are too low in regions

Table 2.1: Regional estimates of R_{sub} (Eq. 2.3; a proxy for export) and $f-$ratio (Eq. 2.5) from profiling floats with mean and 95% CI. The rightmost column shows results from previous publications, where available. Here, NCP is expected to be roughly similar to export.

Region	$f-$ratio	Export [mol C m$^{-2}yr^{-1}$]	NCP [mol C m$^{-2}yr^{-1}$]
Central Indian	0.02 ± 0.08	0.1 ± 0.5	-
Drake Passage	0.68 ± 0.55	4.4 ± 2.9	-
Hawaii	0.00 ± 0.03	-0.1 ± 0.2	2.5 ± 0.7^{a}
Sargasso	0.34 ± 0.16	3.9 ± 2.3	3.8 ± 1.2^{a}
Southern Indian	0.36 ± 0.13	3.8 ± 1.1	-
Southern Pacific	0.47 ± 0.77	3.2 ± 3.2	-
Station P	0.19 ± 0.22	1.3 ± 1.5	2.3 ± 0.6^{a}
Western Pacific	0.42 ± 0.28	3.8 ± 1.8	2.9 ± 0.2^{b}

[a] Annual Net Community Production (ANCP), *Emerson* (2014). [b] Total NCP between winter and September, *Midorikawa et al.* (2002).

where they fall significantly short of R_{sub}, as in the Sargasso Sea (Fig. 2.7). The difference here could arise from local inaccuracies in Eqs. 2.6 and 2.7 (which are formulated to fit global trends), or from errors in satellite measurements of NPP, which can be as large as 35% (*Hooker and McClain*, 2000). In several regions (e.g. Hawaii) float-based observations are significantly lower than parameterizations, and we explore this further in Section 2.4.3.

2.4 Discussion

2.4.1 Comparison to previous work

Several of the regions in the work (Hawaii, Sargasso Sea, Station P, and Western Pacific) coincide with areas that are very well studied and have many estimates of surface NCP. Again, we assume that on annual time scales the upper ocean is at steady state, and the estimates of NCP from these studies are approximately equal to the export flux, which in turn is largely remineralized in the upper ocean (*Martin et al.*, 1987; *Buesseler et al.*, 2007). We do not expect NCP at the surface to exactly match our observations of R_{sub}, however, they are likely similar in scale.

Our estimates of R_{sub} in the Sargasso and Western Pacific regions are in general agreement with the observations of surface NCP by other studies (see Table 1). Observations of tracer-based apparent oxygen utilization rates (AOUR) in the Sargasso Sea also allow us to make a more direct comparison. *Stanley et al.* (2012) found AOUR to be 3.1 ± 0.5 mol O_2 $m^{-2}yr^{-1}$ in the upper 500 m, which is about half of what we estimate from float observations. This difference may be at least partially attributable to spatial variability, as the floats are not tightly clustered around the site examined by *Stanley et al.* (2012) and we do observe spatial gradients in R_{sub} in the Sargasso Sea. In contrast to past results, our observations at Station P are somewhat low, and very low at Hawaii (*Emerson*, 2014). In order to diagnose the performance of our methods (oxygen evolution on profiling floats), we further examine what may cause such discrepancies.

2.4.2 Comparison to HOT and BATS

To augment our analysis, we also compute R at Hawaii Ocean Time-Series (HOT; *Karl and Lukas* (1996)) and Bermuda Atlantic Time-Series (BATS; *Michaels and Knap* (1996)) using those sites' oxygen concentration time series and utilizing the same analysis used for float oxygen data (Section 2.2.2). The temporal resolution (approximately monthly) is not as fine as float cycles, but this should not negatively impact our results. The vertical structure of the net respiration profile based on BATS data is similar to the nearby float data (Fig. 2.8, left panel), with a moderate difference in magnitude. Examination of individual float-year data suggests that this discrepancy in magnitude is due to spatial variability, where float data collected closer to the BATS site show the most similarity. The HOT-based net respiration estimates and Hawaiian float data (Fig. 2.8, right panel) both suggest that R is quite weak in the region. It is encouraging that R calculated from multi-decadal time-series generally corroborate the float-based measurements. However, the method of using oxygen evolution as a proxy for biological metabolism (Eq. 2.2) must be scrutinized.

2.4.3 Method examination

The large difference between float measured R_{sub} and past observations of upper ocean NCP at HOT may have several different interpretations. First, it could indicate high transfer efficiency, where a very large fraction of the new production at the surface makes its way to the deep ocean, bypassing remineralization. Second, it could suggest the magnitude of biological production in the region is substantially different than has previously been assumed. Third, it could reveal that our methods have shortcomings, and under certain conditions we are unable to adequately capture the sub-mixed layer respiration.

Carbon flux usually exhibits a strong decrease with depth (*Martin et al.*, 1987), so it would be unusual for such a large fraction (well over 50%) of carbon to escape to great depth without being remineralized. We are also hesitant to claim that the float-based estimates of respiration are representative of the Hawaiian region, as we expect the depth-integrated respiration to be of similar scale to past estimates of euphotic zone NCP. *Emerson* (2014) compiled numerous independent studies and estimated NCP to be 2.5 ± 0.7 mol C $\text{m}^{-2}\text{yr}^{-1}$ at HOT, while we observe essentially no statistically significant respiration below the euphotic zone. This leads to the examination of the third reason for the potential discrepancy.

Thus far, we have employed Eq. 2.2 with the assumption that (at least for ensemble averages) advective and diffusive terms can be neglected. However, Eq. 2.1 demonstrates that there can be significant respiration without a corresponding change in oxygen concentration (e.g. $\text{d}[\text{O}_2]/\text{dt} = 0$), so long as there are balancing advective-diffusive contributions. Consequently, our low values obtained at HOT could be biased by physical interference.

In order to investigate the potential effect of lateral advection on our observations (i.e. the horizontal terms in $\vec{u} \cdot \nabla O_2$), we utilize World Ocean Atlas (WOA) oxygen climatology (*Garcia et al.*, 2010). Here we assume that oxygen concentrations are constant in time and vary only along the float path. We linearly interpolate the WOA oxygen to the floats' position, thereby creating synthetic oxygen time-series determined solely by float drift. We then applied Eq. 2.2 to the WOA-based oxygen time series to examine potential bias from float advection. Based off of this simple analysis, we find that none of the regions examined in Fig. 2.4 have a contribution from horizontal float advection that is statistically different from zero. This is not to suggest that advection plays no role in biasing our measurements, but it may not be the primary factor in the discrepancy between float observations and other methods.

In addition to lateral float advection, vertical pumping and diffusion could account for the disagreement between float data and other studies. Hawaii is a region of general downwelling caused by the dominant local wind stress curl (*Risien and Chelton*, 2008), and coupled with the vertical structure of oxygen in the region it could play a role in replenishing oxygen and obscuring our observations of R. Similarly, vertical diffusion could act to oxygenate the sub-mixed layer, creating a net downward flux of oxygen and counteracting the effects of respiration.

There are a number of large uncertainties associated with the physical terms in Eq. 2.1 that prevent us from accurately quantifying the physical impact on oxygen. First, diffusion terms are uncertain and difficult to accurately constrain. Second, we do not have reliable estimates of velocities associated with Ekman pumping. Last, our aforementioned analysis of lateral advection is based on climatology that cannot replicate the true complexity of the oxygen field traversed by the floats. When oxygen is at steady-state, respiration is essentially the residual of the physical terms in Eq. 2.1. Without a strong respiration signal even small uncertainties in the physical terms compound and make it impossible to deduce respiration.

However, in locations well-sampled by other studies (Hawaii, Sargasso Sea, Western Pacific, Station P), we can arrive at some qualitative observations on the effectiveness of this method. In regions where there is a deep wintertime mixed layer ($\geq$ 200 m) and a high degree of ventilation (Sargasso Sea, Western Pacific) there is good agreement with previous estimates. Regions of relatively shallow wintertime mixed layers ($\sim$ 100 m) do not corroborate past results. We find R_{sub} to be negligible to small at both Hawaii and Station P, while we expect values to be approximately 2 to 4 mol C $\mathrm{m^{-2}\ yr^{-1}}$ in these regions (*Sonnerup et al.*, 2013; *Emerson*, 2014). We therefore suggest that attempts to diagnose net respiration and remineralization solely based on temporal oxygen evolution will perform reasonably well in regions where the mixed layer undergoes large seasonal change, and fare poorly where ventilation is weakly seasonal.

2.4.4 Examining where methods are valid

As discussed, we posit that Eq. 2.2 will perform poorly at estimating respiration at weakly seasonal locations. It is useful to quantify this further, and we employ two datasets to determine seasonality of export production.

The first is the VGPM NPP estimate (*Behrenfeld and Falkowski*, 1997). For each region we calculate the amplitude of the annual cycle of NPP at each grid point of the VGPM dataset (spaced by $1/6^o$) where the ocean is at least 2000 m deep (to avoid coastal environments the floats do not encounter). We use the following equation as a fit to the time series of NPP data, using least squares:

$$NPP_{fit} = A_{vgpm} cos(\omega t + \phi) + y_0 \tag{2.10}$$

where A_{vgpm} is the amplitude of the fit (mol C $m^{-2}yr^{-1}$), we fix the frequency, ω, to be equivalent to $2\pi/yr$, ϕ is the phase, and y_0 is the offset from zero. We then determine the mean of A_{vgpm}, $\overline{A}_{vgpm}$, over the spatial domain of the eight regions examined (see Fig. 2.6 and 2.7 for extent of spatial domains in each region). The comparison between $\overline{A}_{vgpm}$ and R_{sub} is presented in the upper panel of Fig. 2.9. The second metric we use for seasonality is derived from climatological mixed layer depths (*de Boyer Montégut et al., 2004*; grid spacing 2^o). Here we take the simple difference between the maximum and minimum climatological estimates for the mixed layer depth ($\Delta MLD = MLD_{max} - MLD_{min}$) at each grid point to determine how much MLD changes over the course of one year. We then calculate the average of ΔMLD, $\overline{\Delta MLD}$, in each region. The comparison between $\overline{\Delta MLD}$ and R_{sub} is presented in the lower panel of Fig. 2.9.

Grouped by region, we observe similar patterns using both NPP and MLD metrics to represent seasonality (Fig. 2.9). In general, higher seasonality (higher $\overline{A}_{vgpm}$ and $\overline{\Delta MLD}$) corresponds to higher estimates of R_{sub}, with the notable exception at Station P using the NPP seasonality measure.

Our estimates of R_{sub} tend to agree reasonably well with past estimates (*Emerson*, 2014; *Midorikawa et al.*, 2002) for $\overline{A}_{vgpm} > 3$ mol C $m^{-2}yr^{-1}$ and $\overline{\Delta MLD} > 80$ m. $\overline{A}_{vgpm}$ and $\overline{\Delta MLD}$ generally exceed these thresholds in higher latitude regions where seasons actually occur (Fig. 2.10). The spatial patterns of highly seasonal regions are fairly similar, whether defined by MLD or NPP (Fig. 2.10), and are not particularly sensitive to in the precise values used for the thresholds. The subarctic north Pacific is one region of some disagreement between the two metrics for seasonality. Here, there is strong seasonality in NPP, but not MLD (presumably due to a strong halocline inhibiting deep winter mixed layers). Because our Station P estimate of R_{sub} could be an underestimate (*Emerson*, 2014) in this region, the MLD method for determining the seasonal threshold may be more advisable here. However, in the absence of more information, it is inadvisable to extend this to a global generalization. 3 mol C $m^{-2}yr^{-1}$ and 80 m are usually exceeded poleward of 30^o, while the lower latitudes are expectedly less seasonal. Using Fig. 2.10 as a rough guideline we can conclude that other studies using methods similar to ours (Section 2.2.2) will generally obtain reasonable estimates poleward of 30^o and should be skeptical of results equatorward of 30^o.

2.5 Conclusions

There are several central results from this study. The vertical structure and overall magnitude of net respiration is highly variable across different global regions. Generally, we estimate that export and export efficiency is greater at higher latitudes, which corroborates past studies (*Laws et al.*, 2000; *Dunne et al*, 2005; *Henson et al.*, 2012). However, our observations may be biased low at low-latitude and regions with weakly seasonal mixed layer depth and shallow seasonal pycnoclines.

The float-based estimates of export and export efficiency that we expect are reliable are in Drake Passage (export = 4.4 ± 2.9 mol C m^{-2} yr^{-1}; $f-$ratio = 0.68 ± 0.55), Sargasso

Sea (3.9 ± 2.3, 0.34 ± 0.16); Southern Indian Ocean (3.8 ± 1.1; 0.36 ± 0.13), and Western Pacific (3.8 ± 1.8; 0.42 ± 0.28).

There is weak, yet significant, correlation between subsurface respiration (R_{sub}) and surface variables, where greater production and larger community structure tend to accompany greater respiration at depth. The weak correlation could be partially caused by variability in respiration rates caused by physical advection or large errors in satellite derived data products. However, it highlights the importance of field observations in determining net community production and respiration.

Ultimately, as the population of profiling floats equipped with dissolved oxygen sensors grows, so too will our ability to observe net respiration and remineralization in the ocean. Greater sample sizes will allow more precise regional characterizations and a greater breadth of spatial coverage will enable further exploration of important aspects of the global carbon cycle. Although this method has shortcomings, mostly at low-latitudes, the majority of export production (and hence remineralization) occurs at mid- to high-latitude (*Henson et al.*, 2011), suggesting profiling floats equipped with appropriate sensors can make valuable contributions to carbon cycling research.

Acknowledgments

This work was generously supported by University of Washington grant number NA15OAR 4320063 and grants OPP-1353177 and OPP-1429342 from the National Science Foundation. The float data presented here can be accessed at http://runt.ocean.washington.edu/o2/. All other data used are attributed in the references. The floats were all fabricated at the University of Washington from components purchased from Teledyne/Webb Research. We thank Dana Swift, Rick Rupan, and Greg Brusseau of the University of Washington for their superb skills in producing these high quality instruments. We thank Steven Emerson for valuable discussions that substantially improved the content of the manuscript, as well as Shirley Leung for discussions on remote observations of community structure. We also thank two anonymous reviewers for comments that helped clarify and improve the manuscript.

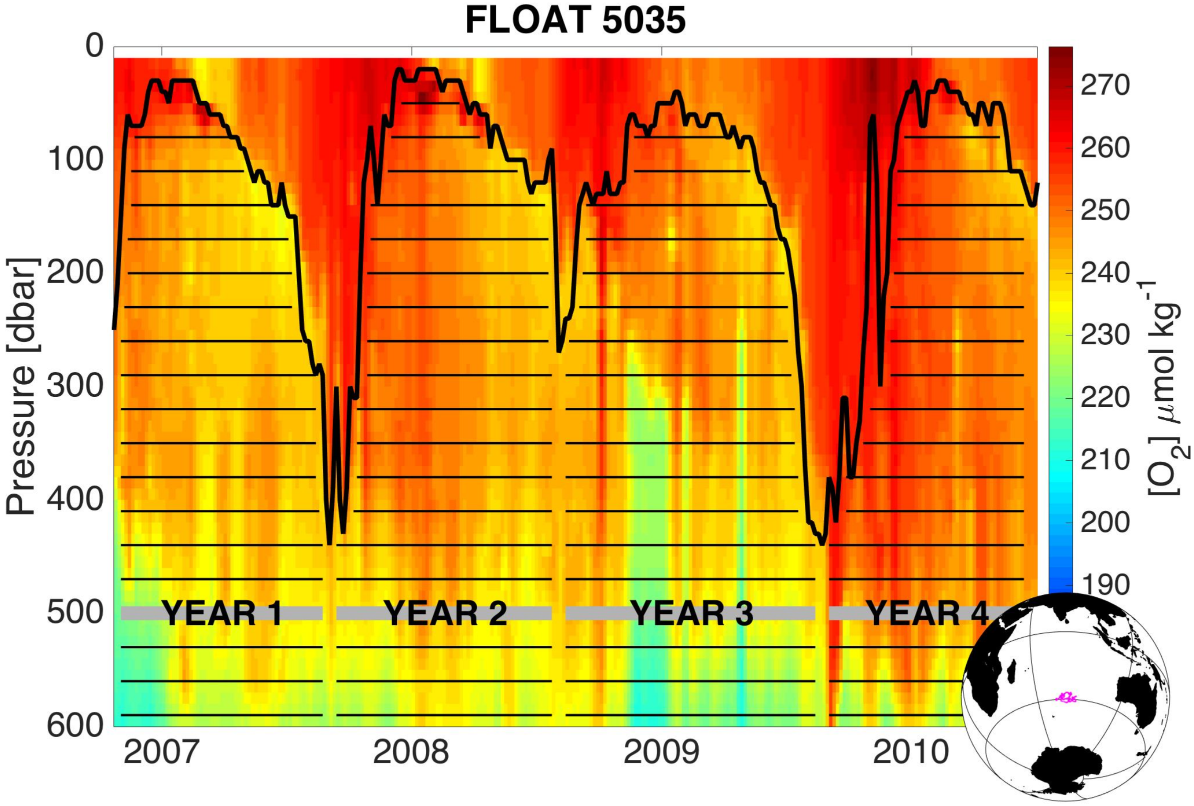

Figure 2.1: An example of oxygen evolution in the upper 600 m for UW float 5035 (WMO 1900722), located in the southern Indian Ocean. Thick black line: mixed layer depth. Horizontal black lines: time periods and depths for which the time rate-of-change of oxygen is calculated (for visual clarity, not every pressure level used is shown here). Small globe: the profile locations of float 5035 from 2007-2010 (magenta dots).

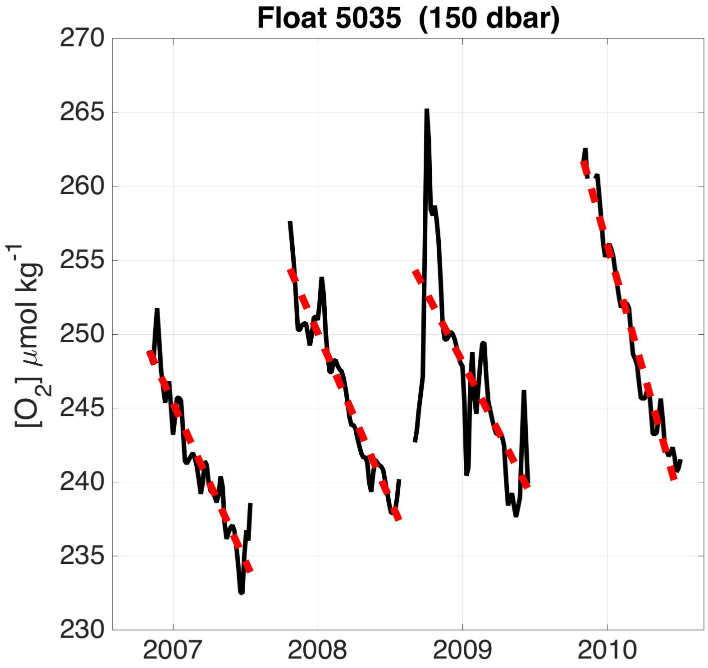

Figure 2.2: Solid black: oxygen concetration from UW float 5035 at 150 dbar (only when below the mixed layer). Dashed red: linear regression to each float-year. The slope of this line is assumed to be the net oxygen consumption rate (or production if slope is positive).

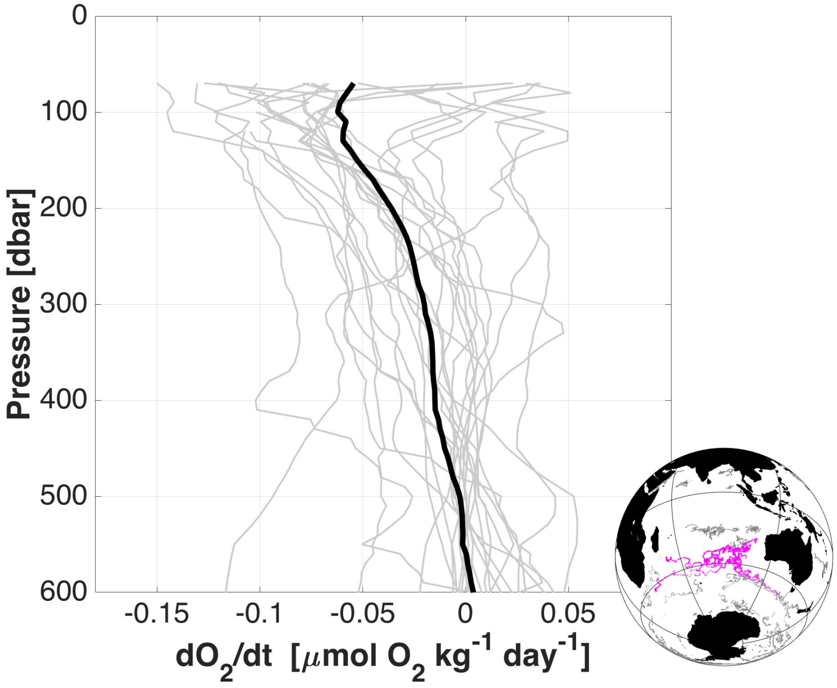

Figure 2.3: 25 vertical profiles of oxygen time rate-of-change calculated from each float-year in the southern Indian region. The thick black line is the ensemble mean. Small globe shows the float profiles used (magenta) and unused (grey) in main panel.

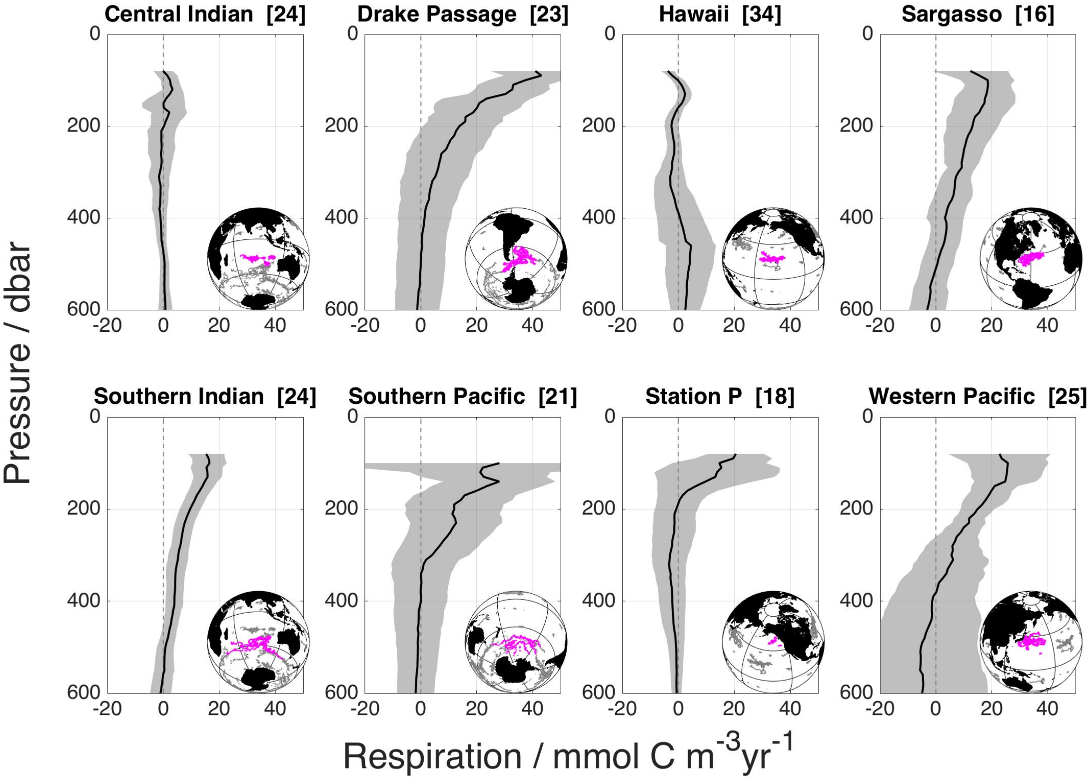

Figure 2.4: Depth profiles of net respiration rate (R) determined from floats with Optode oxygen sensors. The thick black line is the mean profile calculated from the ensemble of float-years in the given region, while the shaded region is the 95% confidence interval (assuming Gaussian distribution). The bracketed number is the number of float-years used in each region. The small globe shows the locations of profiles used (magenta) and unused (grey) in regional composite.

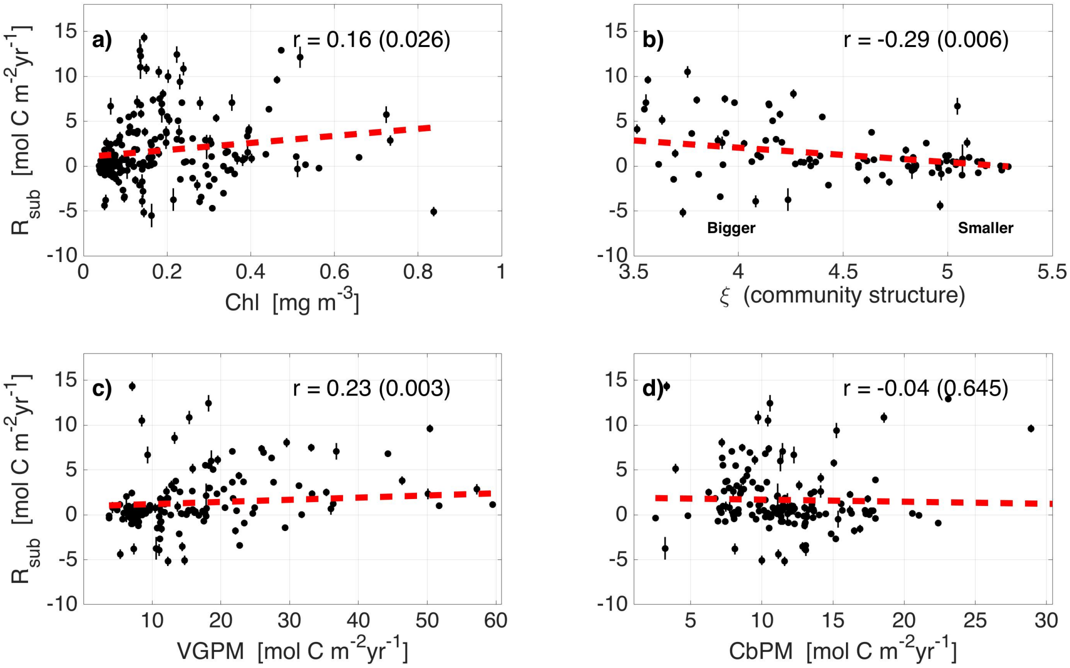

Figure 2.5: Correlation between surface variables and the subsurface respiration, R_{sub}. In each panel the black points show data that are used for determining the correlation coefficient, r (with the corresponding p-value in parentheses). Vertical error bars are established by summing (in quadrature) the error from the d$[O_2]$/dt estimates in the pressure range used in Eq. 2.3, and scaling by the Redfield ratio to convert from oxygen to organic carbon. The red dashed line is the linear regression to the black points.

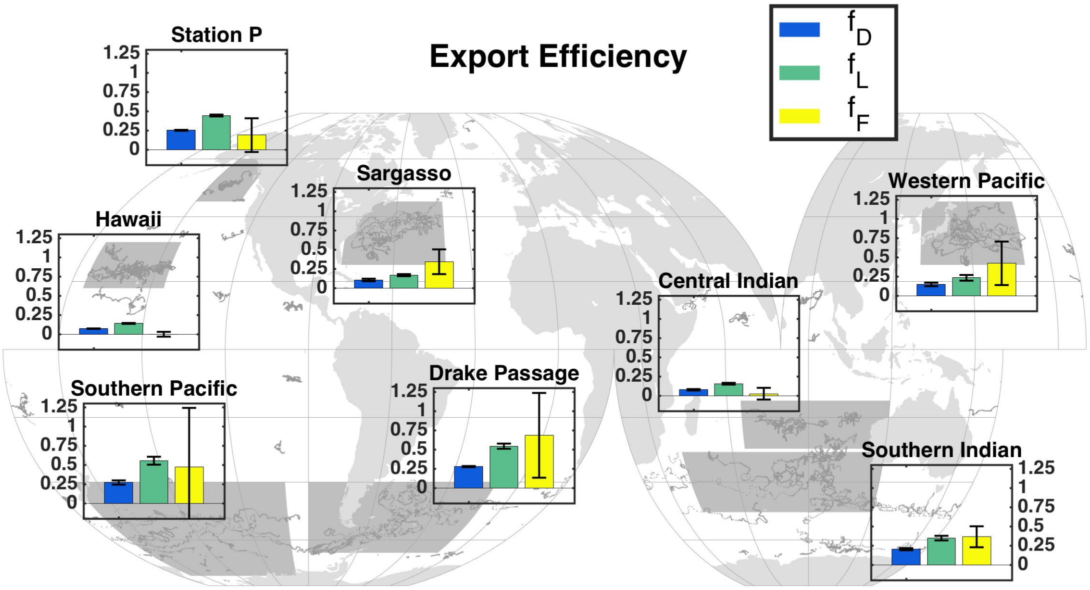

Figure 2.6: Regional estimates of the $f-$ratio. Dark grey dots are profile locations of floats used in this study. Shaded grey regions are the spatial boundaries used to delineate regions, and accompanying small bar plots show the regional $f-$ratio calculated by several means. Yellow: estimates of f_F derived from float and satellite observations. Blue and green: parameterizations of export efficiency (f_D, f_L). Error bars on estimates are 95% confidence interval assuming Gaussian distribution (see Fig. 2.4 for number of float-years in each region.)

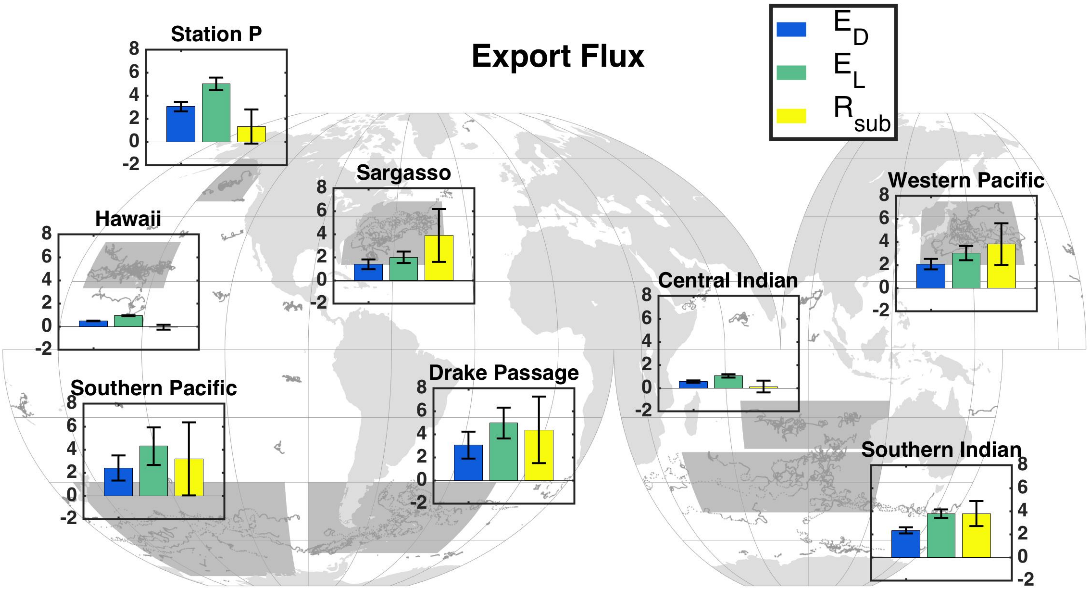

Figure 2.7: Identical to Fig. 2.6, but for carbon export. E_D and E_L are based on parameterizations, and R_{sub} is a lower bound of export estimated from float-observed respiration. Units are mol C m^{-2}yr^{-1}.

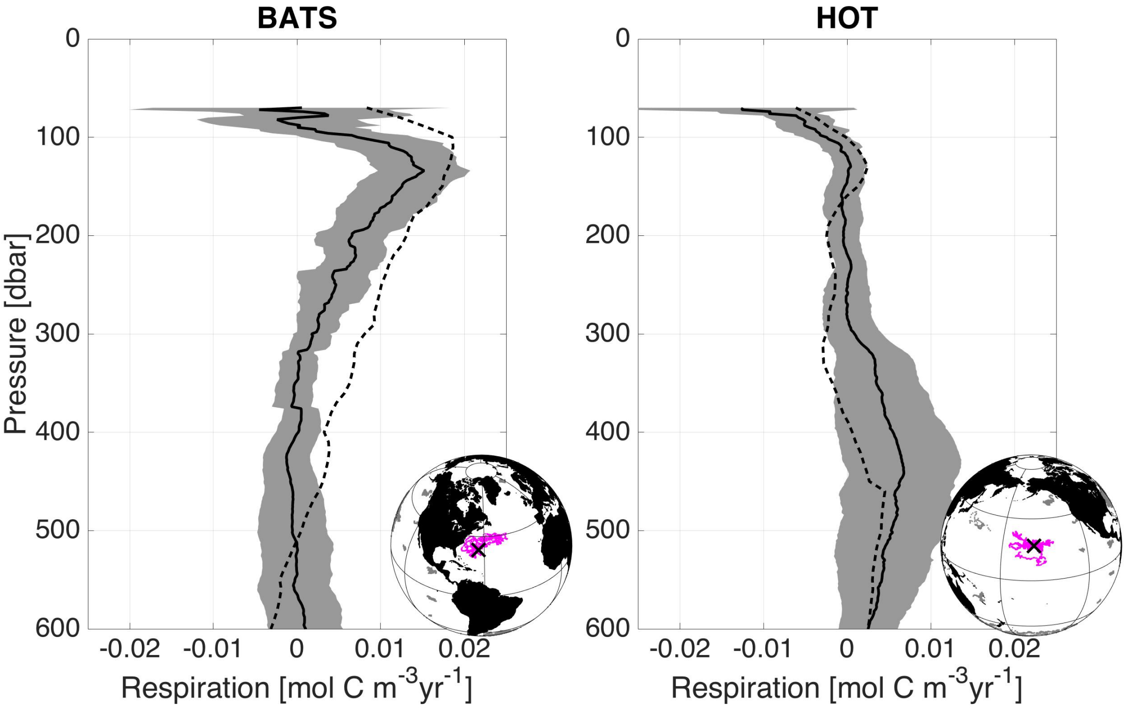

Figure 2.8: The net respiration profile calculated from oxygen time series at HOT and BATS. The solid black line is the mean respiration, and the shaded grey is the 95% confidence interval. The dashed line is the mean of the corresponding float data (identical to Fig. 2.4). The small globes show the locations of profiles used (magenta) and unused (grey) in the regional mean, as well as the HOT/BATS sites (black cross).

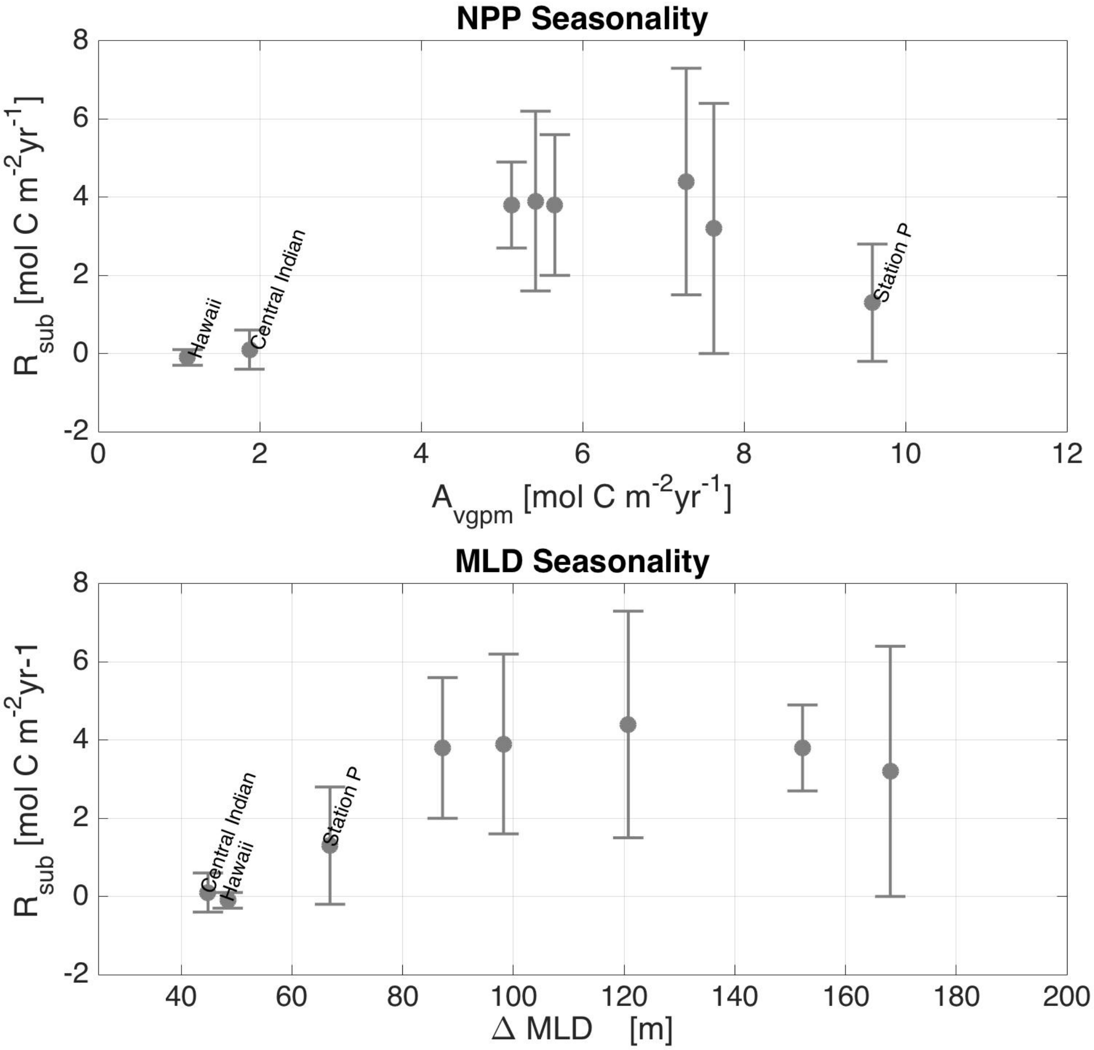

Figure 2.9: Upper panel: The amplitude of the NPP seasonal cycle ($\overline{A}_{vgpm}$) compared to R_{sub} in each region examined. Bottom panel: The difference difference between the maximum and minimum climatological MLD, $\overline{\Delta MLD}$, plotted against R_{sub} in each region. The region we expect our method may be underestimating respiration are labeled in each plot. See Section 2.4.4 for explanation of NPP and MLD seasonality estimates.

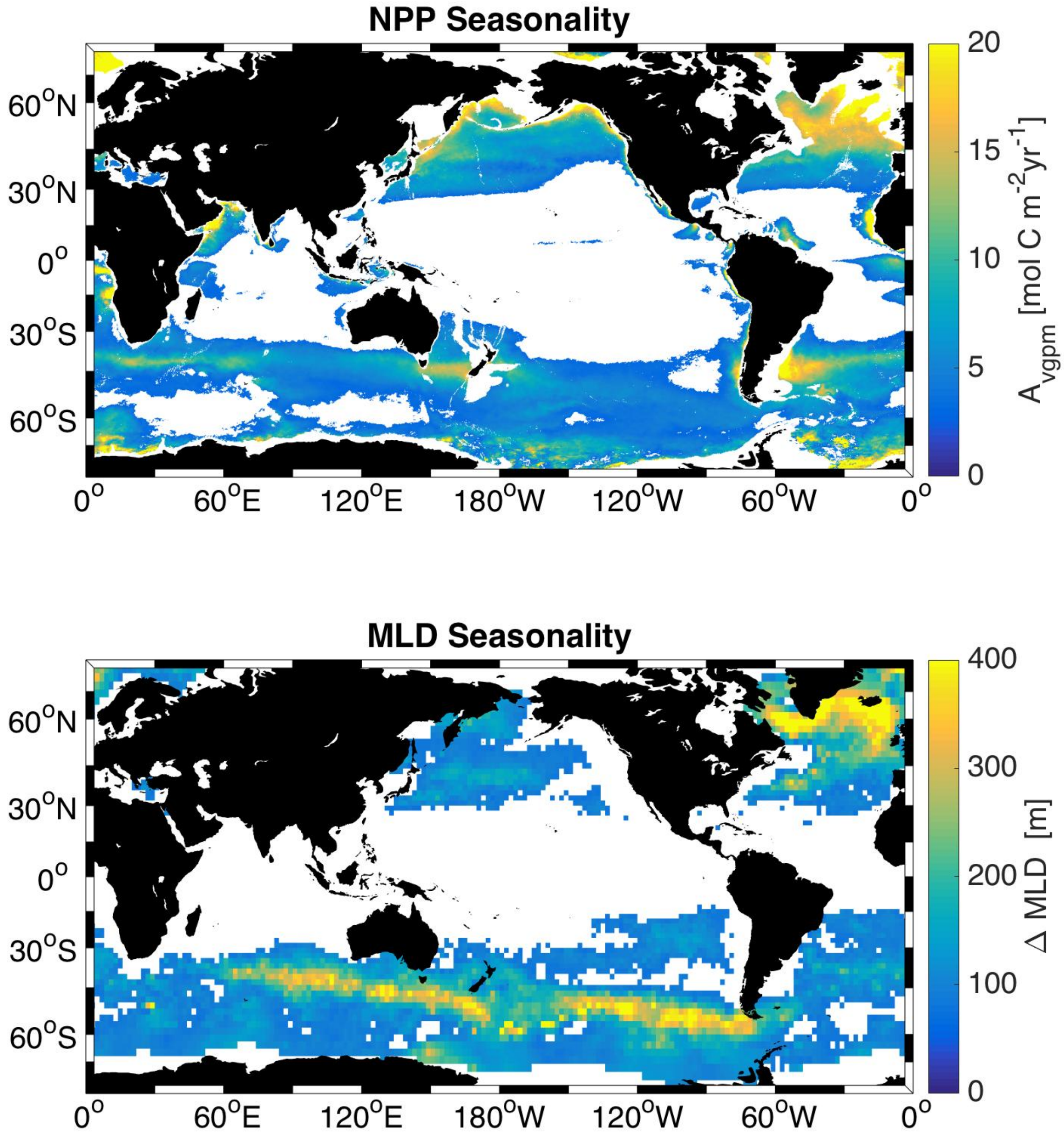

Figure 2.10: Top panel: A global plot of the NPP seasonl cycle amplitude (A_{vgpm}), where values below 3 mol C $m^{-2}yr^{-1}$ are masked. Bottom panel: A global plot of the difference between the maximum and minimum climatological MLD, where values below 80 m are masked. Non-masked regions are expected to be areas where the methods presented in this paper perform reasonably well. In the masked regions we expect our methods to result in an underestimate of respiration.

Chapter 3

USING REGIONAL COMPOSITES TO EXAMINE GLOBAL BIOPHYSICAL PATTERNS OF MESOSCALE EDDIES

Tyler D. Hennon and Stephen C. Riser ***[In Prep.]***

Abstract

The supply of nutrients to the euphotic zone, a crucial factor in the biological pump, is significantly influenced by the presence of mesoscale eddies. Here we utilize hydrographic data to create composite averages of mesoscale eddy features on the global scale. Combining these hydrographic composites with remote observations of chlorophyll, we characterize the effect of eddies on nutrient supply to the upper ocean and the corresponding surface chlorophyll expression. Markedly different trends arise between cyclonic and anticyclonic eddies. Cyclonic eddies, which uplift isopycnals, have anomalously high nitrate in the upper 200 m as well as elevated surface chlorophyll in the center of the eddy. Conversely, anticyclonic eddies tend to have negative nitrate anomalies and depleted surface chlorophyll. The influence of eddies on nitrate and chlorophyll is spatially variable. At low- and mid-latitudes, the nutrient supply from eddy pumping has a strong relationship with the surface chlorophyll, which suggests a biological response to changing nutrient availability. However, at high-latitudes, where micronutrients such as iron limit phytoplankton growth, there is no correlation between flux of macronutrients and surface chlorophyll. Factors such as wind speed, eddy age, and seasons, are not found to have a large effect on either nutrient anomalies or chlorophyll expression.

3.1 Introduction

The rate of nutrient supply throughout the surface ocean is often equated with new production (*Eppley and Peterson*, 1979), which at steady-state is related to the export of organic carbon sinking to depth, often referred to as the biological pump. The biological pump is a crucial component of the global carbon cycle and is estimated to sequester ~10 Pg C yr^{-1} (*Sarmiento and Gruber*, 2002).

There are many mechanisms that bring nutrients to the euphotic zone, thus fueling phytoplankton growth. Wind driven mixing can supply nutrients to the surface by episodic events (*Marra et al.*, 1990; *Wilkerson et al.*, 2006), accelerating the slow delivery by vertical diffusion (*Lewis and Harrison*, 1986). Such conventional processes, however, may not be enough to close the nutrient budget in some regions (*Planas et al.*, 1999). In the past few decades, nutrient delivery by eddies has been identified as an important source term on basin scales. Models and *in situ* observations show that eddies can account for up to one third of the overall nitrate supply to the euphotic zone in the Atlantic (*Oschlies and Garcon*, 1998).

There are several processes by which eddies influence biological production. *Eddy pumping* is a process where isopycnals shoal in cyclonic eddies (cyclones) and deepen in anticyclonic eddies (anticyclones). Consequently, in cyclones the nutricline is elevated closer to the euphotic zone, fueling the surface with nutrients needed for photosynthesis. In anticyclones the nutricline deepens, lessening nutrient availability in the euphotic zone and perhaps suppressing production. Many studies present evidence for enhanced biological production due to cyclonic eddy pumping (*Falkowski et al.*, 1991; *McNeil and Jannasch*, 1999; *Siegel et al.*, 1999). *Eddy-Ekman pumping* occurs in eddies under steady winds. Large-scale wind stress is higher on one side of the eddy and lower on the opposite side (winds are in the direction of surface currents on one side, and oppose currents on the other side). This causes convergence (downwelling) in cyclonic eddies and divergence (upwelling) in anticyclones. *Martin and Richards* (2001) observed evidence of eddy-Ekman pumping in the North Atlantic. Generally, the influences of eddy pumping and eddy-Ekman pumping oppose each other; however, *McGillicuddy et al.* (2007) find that these effects act in tandem in mode-water eddies to produce strong blooms. *Mahadevan et al* (2012) also suggest that eddies hasten the onset of the springtime bloom by increasing stratification (by shearing lateral density gradients), which causes a shallower mixed layer and in turn increases light levels past the threshold needed for a bloom (*Sverdrup*, 1953).

The very large datasets made available by remote satellite observations offer a powerful way to examine the global effect of eddies on surface chlorophyll. *Siegel et al.* (2011) and *Chelton et al.* (2011a) observe strong signals of *eddy advection*, where surface chlorophyll gradients are distorted by eddy rotation. While there are many insights gained by remote observation, there are limitations as well. Eddy advection itself has little biological impact (*Siegel et al.*, 2011) as it primarily stirs local chlorophyll gradients. Additionally, the overall effects of eddy pumping may not be readily apparent at the surface. Often the maximum chlorophyll enhancement in eddy-driven blooms occurs below the penetration depth of satellites (*Falkowski et al.*, 1991), since the penetration depth is typically less than 20 m for the wavelengths characteristic of chlorophyll (*Gordon and McCluney*, 1975). This may account for the relatively weak trends related to eddy pumping observed by *Siegel et al.* (2011).

As previously mentioned, there are numerous publications that utilize remote observations to measure the effects of eddies on chlorophyll. The power of these studies is their large sample size and ability to quantify the surface expression of an “average” eddy, however, they do not capture the full-depth dynamics. Conversely, there are many studies that provide great detail about a single eddy event; the obvious drawback is limited sample size.

Here, we aim combine large datasets of hydrography and satellite observations to increase sample size and global coverage while quantifying the full depth dynamics of mesoscale eddies. We identify historical shipboard vertical profiles (providing physical and biogeochemical variables) that are coincident with mesoscale eddies. Satellite surface chlorophyll, which coupled with the vertical profiles, allows us to construct a three dimensional synthesis of composite eddies using ensemble averaging techniques. The broad spatial domain of remote and hydrographic datasets enables us to observe the global variability of the effect of eddies on nutrient availability and surface chlorophyll expression. Many observations come from the oligotrophic regions of the ocean, an area that is critical to quantify as up to half of all surface organic matter export occurs here (*Emerson et al.*, 1997).

3.2 Data and Methods

3.2.1 Data used

We use multiple data products to address the role of eddies on chlorophyll and nutrients.

Satellite Altimetry:

We use the eddy dataset from *Chelton et al.* (2011b), which tracks eddy features globally from October, 1992, to April, 2012, on a 7-day temporal grid (data can be retrieved at http://cioss.coas.oregonstate.edu/eddies/). The product is derived from AVISO altimetry and characterizes the location, radial length scale, rotational velocity, and sea surface height expression for eddy-like features every seven days (all eddies persist for at least three weeks).

MODIS Chlorophyll a:

To characterize the surface chlorophyll concentration, we use observations from the Moderate Resolution Imaging Spectroradiometer (MODIS; *Esaias et al.* (1998)), which captures global surface chlorophyll *a* concentrations (via an empirical algorithm on the raw color). The gridded data have an 8-day time step and horizontal resolution of approximately 9km (1/12 degree by 1/12 degree).

Hydrography:

We use hydrographic data from the World Ocean Database (WOD; https://www.

nodc.noaa.gov/OC5/WOD/pr_wod.html) for observations of subsurface nutrients, such as nitrate and phosphate, and physical variables, such as temperature and salinity. We only use casts that have at least 10 samples of temperature, salinity, and nitrate in the upper 1500 m. Many casts have at least 24 samples distributed throughout the entire water column, where measurements are generally concentrated near the surface, consistent with standard depth levels of hydrographic surveying.

WOA (2009):

We also use monthly the World Ocean Atlas (WOA) climatology. Climatological values for temperature (*Locarnini et al.*, 2010), salinity (*Antonov et al.*, 2010), nitrate, and phosphate (*Garcia et al.*, 2010) serve as a baseline by which to compare synoptic measurements (WOD). Temperature, salinity, and oxygen climatology extend from the surface to a maximum depth of 1500 m, while nutrients (nitrate and phosphate) only extend to 500 m.

3.2.2 Spatial domains

In order to investigate the spatial variability of the effect of eddies on temperature, salinity, nutrients, and chlorophyll, we delineate data into many different regions (Fig. 3.1). The area encompassed by these regions is quite large, but this is required to obtain a decent sample size of hydrographic casts coincident with eddies in some of the regions (the number of satellite observations in each region usually reaches thousands). However, this is still adequate spatial resolution to establish broad patterns in global variability (addressed in Section 3.3.1). We do not include the equator in this analysis (latitudes less than 5^o). Near the equator the spatial density of eddies is relatively low, and signals from eddies at very low latitude might be obscured by strong equatorial upwelling (e.g. *Wyrtki* (1981)).

3.2.3 Subsurface data analysis

We utilize the *Chelton et al.* (2011b) eddy dataset in conjunction with hydrographic profiles (WOD) to determine the effect of cyclonic and anticyclonic eddies on the vertical profile of nutrients. In order to maintain focus on mesoscale eddies (instead of linear Rossby waves or misinterpreted sea surface height (SSH) features in fronts) we only consider eddies from the Chelton dataset that satisfy all of the following:

1. The rotational velocity is greater than the translational velocity. This maintains focus on nonlinear eddies and eliminates linear Rossby waves from consideration. The majority, ∼87% of the total, qualify as nonlinear by this definition.

2. SSH expression of eddies is greater than 5 cm. This targets stronger events and lessens the likelihood of including mischaracterized surface features. About half (45%) of all eddies have a surface expression greater than 5 cm.

3. We ignore regions of high velocity (> 0.25m/s). We use surface-velocity derived from a drifter data product (*Lumpkin and Johnson*, 2013) to constrain our observations to more quiescent regions, so that shear features associated with fronts are not misidentified as eddies. About 78% of eddies are not in regions of currents > 0.25 m/s.

These conditions leave ∼32% of the original dataset. Although this removes a considerable fraction of data, it still leaves over 8 x 10^4 eddy observations for analysis. For each hydrographic cast in the WOD dataset we find the nearest Chelton eddy (satisfying the aforementioned conditions) in space and time. The parameters of this eddy (location, radius, etc.), originally on a 7-day time step, are linearly interpolated to the exact time of the hydrographic cast. The lateral distance (in km) between the cast and the eddy center is converted to a normalized eddy radius (where 0 is at the eddy center and 1 is at the edge of the eddy). We use casts that fall within 3 radii of the nearest eddy, although we expect the strongest signals to be within 1 to 2 eddy radii. Casts not falling within 3 radii of the nearest eddy are not used in analysis. The number of *in situ* casts used in each region in Fig. 3.1 is, on average, several dozen. This is one to two orders of magnitude less than the number used in the composites of chlorophyll using satellite observations (Section 3.2.4), yet in most cases is sufficient to quantify the gross effects of eddies on subsurface variables.

We use monthly climatology (WOA) as a baseline to control for temporal and spatial variability. This allows us to calculate the vertical profile of the nitrate anomaly, $\Delta N(z)$, such that:

$$\Delta N(z) = N(z) - N(z)_{WOA} \tag{3.1}$$

where $N(z)$ is the vertical profile of hydrographic nitrate in the vicinity of an eddy, and $N(z)_{WOA}$ is the corresponding climatological profile interpolated to the location and depth grid of the cast (Fig. 3.2a). In each region (Fig. 3.1) we compile the profiles of $\Delta N(z)$ within three radii of eddies and use objective mapping to construct a composite of the nitrate anomaly induced by cyclonic and anticyclonic eddies (Fig. 3.2b). Our objective mapping scheme follows algorithms by *Barnes* (1994a,b,c) and uses a radial grid of 0 to 3 normalized radii, spaced by 0.05, and a depth grid from the surface to 400 m depth, spaced by 10 m. The smoothing length scales are 50 m and 0.5 radii. We refer to this two-dimensional composite anomaly as $\Delta N(r, z)$, which varies with normalized radius (r) and depth (z).

The manner in which we construct $\Delta N(r, z)$ naturally assumes that the effects of eddies on the nitrate anomaly is radially symmetric. Previous studies (*Castelao*, 2014; *Frenger et al.*, 2015)) that focus on temperature and salinity have found differences between the leading and trailing sides (i.e. west and east, respectively) of eddies, however these asymmetric effects are small and unlikely to severely effect our results. We do not divide the data into west and east sets in order to maintain an adequate sample size for our analysis.

We integrate the nitrate anomaly, $\Delta N(r, z)$ in order to obtain a gross estimate of the total anomaly in eddies:

$$\Delta N_{av} = 2\pi \int_{0}^{200m} \int_{0}^{R} r\Delta N(r, z) dr dz / \pi R^2 \tag{3.2}$$

Eq. 3.2 allows us to calculate the total nitrate anomaly, in mol m^{-2}, in upper 200 m within an average eddy. Here, we choose to integrate from the surface to a depth of 200 m, where 200 m represents the lower boundary of the euphotic zone in open ocean ecosystems (0.1% light penetration; *Karl and Church* (2014)). We also integrate radially to one normalized eddy radius (R), which we then scale to match the median eddy radius of the region (on the order of 100 km). Our analysis presented in later sections is not particularly sensitive to either radial or depth limits of integration. Eq. 3.2 yields two estimates for the nitrate anomaly in each region analyzed (Fig. 3.1); one for the cyclonic composite, and one for the anticyclonic composite.

In Eq. 3.1 we calculate the difference between the observed nitrate and the climatological nitrate on pressure surfaces. It is also instructive to evaluate the nitrate anomaly on isopycnal surfaces so that we may determine the importance of isopycnal motion on shaping nitrate anomalies within eddies. Here we define the nitrate anomaly on isopycnals as:

$$\Delta N(\rho) = N(\rho) - N(\rho)_{WOA} \tag{3.3}$$

Eq. 3.3 is identical to 3.1, but only evaluated with respect to potential density, ρ, instead of depth. We then transform $\Delta N(\rho)$ back to pressure coordinates, which we refer to as $\Delta N^{\rho}(z)$, in order to contrast to the anomalies on pressure surfaces ($\Delta N(z)$). We also calculate the average integrated isopycnal nitrate anomaly in the upper ocean, ΔN^{ρ}_{av}, by substituting $\Delta N^{\rho}(z)$ into Eq. 3.2. Comparisons between nitrate anomalies calculated on pressure surfaces and isopycnal surfaces are presented in Section 3.3.1.

3.2.4 Surface Chlorophyll analysis

We employ the same rejection criteria as in Section 3.2.3, where we set thresholds for eddy amplitude, nonlinearity, and surface current conditions. Following the methodology by *Siegel et al.* (2011) and *Chelton et al.* (2011a), we use an eddy-centric coordinate system to characterize the effects of mesoscale eddies on surface chlorophyll. In each region, we compile thousands of MODIS observations of chlorophyll concentration, *Chl*, within a window ±6 degrees longitude and latitude (approximately 600 km) centered on each eddy position (where the eddy's position is linearly interpolated to the MODIS time grid). We then log-transform the chlorophyll concentration, in mg/m^3, and calculate the mean value at each spatial grid point ($\log_{10}(Chl)$; Fig 3.3a). We then apply a low-pass filter (e.g. *Siegel et al.* (2011)) by calculating a moving average over 20 by 20 pixels of the $\log_{10}(Chl)$ (Fig. 3.3b), denoted as $\overline{log_{10}(Chl)}_{20x20}$. The difference between $\log_{10}(Chl)$ and $\overline{log_{10}(Chl)}_{20x20}$ is defined as the chlorophyll anomaly, ΔChl:

$$\Delta Chl = log_{10}(Chl) - \overline{log_{10}(Chl)}_{20x20} \tag{3.4}$$

We often observe that ΔChl has strong signals near the center of the eddy (Fig 3.3c). It is useful to attempt to quantify the different processes affecting ΔChl, namely eddy pumping and eddy advection. To accomplish this task, we estimate the monopole characteristics of ΔChl (as done for temperature by *Frenger et al.* (2015)). The ΔChl monopole, ΔChl_{mono}, is defined as the radial average of ΔChl (Fig. 3.4b). The residual, ΔChl_{res}, is defined as:

$$\Delta Chl_{res} = \Delta Chl - \Delta Chl_{mono} \tag{3.5}$$

The residual frequently displays patterns that strongly resemble the effects eddy advection consistent with the rotational direction of cyclonic and anticyclonic eddies (Fig. 3.4c). It is important to differentiate between the processes known to affect surface chlorophyll. We equate ΔChl_{mono} to a change in chlorophyll most likely due to eddy pumping. After the estimate of eddy pumping has been removed, we expect ΔChl_{res} to show signals of eddy advection (as in the observations of *Siegel et al.* (2011) and *Chelton et al.* (2011a)). We calculate the fraction of variance accounted for by the monopole, r^2_{mono}, such that:

$$r^2_{mono} = 1 - \sigma^2_{res}/\sigma^2_{\Delta Chl} \tag{3.6}$$

where $\sigma^2_{\Delta Chl}$ and σ^2_{res} are the total variance of ΔChl and ΔChl_{res}, respectively. We only use values of ΔChl and ΔChl_{res} within 200 km of the eddy center to so that we maintain focus on dynamics within or nearby eddies. In order to quantify the total magnitude of the chlorophyll monopole for further analysis, we evaluate the average chlorophyll anomaly per unit area:

$$\Delta Chl_{av} = 2\pi \int_0^R r\Delta Chl_{mono}(r)dr/\pi R^2 \tag{3.7}$$

Similar to Eq. 3.2, we integrate radially to one normalized eddy radius, which we scale to the median eddy radius of the region (typically ~100 km).

3.2.5 Combining surface and subsurface observations

For each region (Fig. 3.1), we combine our observations of ΔN, ΔChl, ΔChl_{mono}, and ΔChl_{res}, to fully characterize composite cyclonic and anticyclonic eddies and resolve nitrate and chlorophyll anomalies (see Fig. 3.5 for an example in Western Pacific). In most regions, ΔN is strongest near the core and decays substantially by one normalized eddy radius, consistent with expectations. Similarly, ΔChl and ΔChl_{mono} are generally strongest at the eddy center and decay with increasing radius. At many of the regions we examine, surface and subsurface patterns are highly suggestive of eddy pumping being an important process that shapes both the vertical nutrient profile and the surface chlorophyll expression.

In Section 3.3.2 we quantify the global behavior of ΔN_{av} and ΔChl_{av}. Here, we wish to highlight that although the main focus of this work is on ΔN_{av} and ΔChl_{av}, there is also a wealth of hydrographic phosphate data. We also estimate the phosphate anomaly, ΔP_{av}, using analogous forms of Eq. 3.1 and 3.2. The relationship between ΔN_{av} and ΔP_{av} (Fig. 3.6) is consistent with the Redfield ratio (16 N : 1 P; *Anderson and Sarmiento* (1994)) and the tight correlation (correlation coefficient = 0.91) suggests that the conclusions we reach using ΔN_{av} will not be significantly altered if we use ΔP_{av} instead. Therefore, the remainder of this paper will continue to use focus on trends in nitrate, but under the assumption that phosphate behaves very similarly.

3.2.6 Investigating effects of wind speed, seasonality, and eddy age

There are a number of factors that might modulate the effect of eddy pumping, such as surface wind speed, seasonality, and eddy age. As mentioned in Section 3.1, surface wind stress induces eddy-Ekman pumping that counteracts the effects of Ekman pumping. In order to investigate this possible effect we break the data into low and high wind speed classifications and calculate ΔN_{av} (as in Section 3.2.3) for both categories. We use NCEP winds (*Kalnay, et al.*, 1996) to estimate the average wind speed over the five days previous to each hydrographic cast coincident with an eddy, and use the median wind speed in the region as the threshold to delineate between low and high speed classes. We might expect to find that ΔN_{av} will have greater magnitudes (positive in cyclones, negative in anticyclones) under low wind speed, and lower magnitudes under high wind speed, due to the counteractive nature of surface wind stress on eddy pumping. Results are presented in Section 3.3.2.

We also suspect that seasonality could also play a role in the nitrate anomaly. For example, we may expect different nutrient uptake (thus different ΔN_{av}) between summer months and the winter months (where other variables, such as light and temperature, may limit phytoplankton growth). To observe potential seasonal differences, we break our data into summer and winter classifications. We define summer as May to September and winter as November to February in the northern hemisphere (vice versa for the southern hemisphere). As done for wind speed and eddy age, we calculate ΔN_{av} separately for summer and winter classifications. See Section 3.3.2 for results.

Another possible factor influencing ΔN_{av} is the age of the eddy. As an eddy is initially formed, it theoretically entraps its own "ecosystem" isolated from the surrounding waters. For example, in cyclonic eddies this may lead to biological stagnation, as nutrients lifted into the euphotic zone are utilized by phytoplankton, thus reducing the nitrate anomaly. We use a threshold of 3 weeks post-formation to differentiate between new and old eddies (all eddies used persist for at least three weeks after formation). The 3 week threshold is chosen so that we maintain an adequate sample size of young eddies (any less than this and we do not have sufficient data). See Section 3.3.2 for results.

3.3 Results

3.3.1 Global Observations

We calculate ΔChl_{av} and ΔN_{av} for all regions (Fig. 3.7), except those that have fewer than 10 casts within one radius of an eddy identified by *Chelton et al.* (2011b). The number of casts falling within one eddy radius for each region is presented in Fig. 3.7. In the majority of regions, cyclonic eddies show positive nutrient anomaly ($\Delta N_{av} > 0$) and positive chlorophyll anomaly (ΔChl_{av} 0), whereas anticyclonic eddies exhibit the opposite behavior. This general pattern suggests that shoaling isopycnals in cyclonic eddies deliver nutrients to the euphotic zone, causing increased phytoplankton production and higher chlorophyll concentrations. Conversely, anticyclonic eddies push the nitracline downward, causing a decrease in surface chlorophyll due to more limited nitrate availability. However, there are number of regions where the sign of ΔN_{av} is opposite that of ΔChl_{av}, indicating that there is a substantial level of variability.

Globally, we observe a significant correlation between ΔN_{av} and ΔChl_{av} (Fig. 3.8). Although chlorophyll is known to be an imperfect metric for biomass and carbon uptake (*Behrenfeld et al.*, 2016), the relatively consistent trends support the notion that eddies can have a significant impact on chlorophyll concentrations and other biological processes. We also examine the ΔN_{av} and ΔChl_{av} data by latitude (Fig. 3.9) and basin (Fig. 3.10). At low- and mid-latitude, there is a significant correlation between ΔN_{av} and ΔChl_{av}, while there is no correlation at high-latitude. The magnitude of nitrate and chlorophyll anomalies are greatest in mid-latitude, which we discuss in greater detail in Section 3.4.1. We observe a positive correlation between ΔN_{av} and ΔChl_{av} in all the basins examined, although correlations are only significant in the Pacific and Indian Ocean.

We also examine the relationship between the magnitude of the nitrate anomaly, $|\Delta N_{av}|$, and the fraction of variance in surface chlorophyll explained by monopole behavior, r^2_{mono} (Fig. 3.11). This gives a measure of how well the magnitude of the nutrient anomaly affects the strength of the monopole behavior of surface chlorophyll. At low-latitude $|\Delta N_{av}|$ and r^2_{mono} are somewhat closer to zero than at mid- and high- latitude (indicating less nitrate anomaly and weaker monopole structure in the surface chlorophyll). At mid-latitude, the $|\Delta N_{av}|$ and r^2_{mono} generally suggest higher nitrate anomalies and surface chlorophyll patterns with a stronger monopole structure. The values at high-latitude appear to fall somewhat in between the broad low-latitude and mid-latitude trends.

The difference between the nitrate anomaly determined on pressure surfaces and density surfaces is stark. For example, in the northwest Pacific region (Fig. 3.12) the strong nitrate anomaly derived from pressure surface analysis essentially vanishes completely when viewed on density surfaces, with no discernible patterns in radius or depth. These observations are broadly true for all regions examined globally (Fig. 3.13) as well. There is a large range in nitrate anomaly determined from pressure surfaces (ΔN_{av}), with clear differences between cyclonic and anticyclonic eddies. The estimates of nitrate anomaly on density surfaces (ΔN^{ρ}_{av}) are centered around zero (no anomaly) for both cyclonic and anticyclonic eddies.

3.3.2 Effects of wind speed, seasonality, and eddy age

We make observations of how the nitrate anomaly is affected by surface wind speed, eddy age, and seasonality (Fig. 3.14). There appears to be no effect of wind speed, as the slope of the linear regression between ΔN_{av} under low and high wind speeds (defined in Section 3.2.6) is not significantly different than 1 (Fig. 3.14a). Presumably, the effects of eddy Ekman pumping should act to drive the slope to be less than 1. Similarly, we do not see a significant effect of seasonality, as the regression between ΔN_{av} in summertime and wintertime is not significantly different than 1 (Fig. 3.14b). However, we do observe a significant effect of eddy age on ΔN_{av} (Fig. 3.14c). The slope of the regression, 0.67 ± 0.18, suggests that newer eddies begin with a stronger nitrate anomaly (positive in cyclones, negative in anticyclones), and that the anomaly decays moderately as the eddy ages.

3.4 Discussion

3.4.1 Spatial variability

This aim of this work is to estimate the broad patterns of *in situ* nutrient delivery of eddies and the corresponding surface chlorophyll expression. In most regions, ΔN_{av} and ΔChl_{av} are positive in cyclonic eddies and negative in anticyclonic eddies. We do observe a somewhat larger scatter in the ΔChl_{av} distribution, but this may be because chlorophyll is an imperfect measure of biomass (*Behrenfeld et al.*, 2016) as different communities of phytoplankton can have very different concentrations of chlorophyll and photo-acclimation to low light can result in an increase in chlorophyll per cell with out an increase in biomass.

Our observations of the surface chlorophyll response to cyclonic and anticyclonic eddies in the Sargasso Sea are similar to those by *Siegel et al.* (2011), who also observed elevated chlorophyll in cyclonic eddies and depleted chlorophyll in anticyclonic eddies (moderate differences between this study and *Siegel et al.* (2011) could be due to different spatiotemporal domains of the datasets used). Our subsurface observations allow us to investigate the subsurface nitrate signature that may be causing these chlorophyll patterns. We find that ΔN_{av} in cyclonic eddies is 0.11 ± 0.02 mol N m^{-2} and -0.04 ± 0.02 mol N m^{-2} in anticyclones.

Although there is significant regional variability (Fig. 3.7), we can arrive at some broad conclusions. The effect of eddies on surface chlorophyll is strongly dependent on latitude (Fig. 3.10). Low- and mid-latitudes (5-25^o S/N and 25-45^o S/N, respectively) show a clear, statistically significant link between nutrient transport and chlorophyll expression, while at high latitudes (45-65^o S/N), there is no such relationship. High latitudes are often associated with high-nutrient low-chlorophyll (HNLC) conditions (*Chisholm and Morel*, 1991), where nitrate is not the limiting resource in phytoplankton growth (instead it may be, for example, iron or light). Therefore, it is conducive that chlorophyll does not have a significant dependence on nitrate at high latitude.

The overall magnitude of the chlorophyll and nitrate anomalies appear to be somewhat higher at mid-latitude than at low-latitude. On average, we observe that eddies at mid-latitude have a greater SSH expression and shallower nitracline depths (the nitracline is defined as the depth of the maximum vertical nitrate gradient). These two characteristics likely act in tandem to produce the differences between low- and mid-latitude that we observe. At mid-latitudes, stronger eddy pumping coupled with a shallower nitracline is the likely cause of the stronger nitrate anomalies we observe, which in turn drive higher chlorophyll anomalies. Conversely, at low-latitudes, weaker eddy pumping and deeper nitracline depths cause smaller nitrate anomalies in the upper ocean, which leads to weak chlorophyll anomaly.

There appears to be a small, negative bias in the nitrate anomaly in the Southern Ocean. Nitrate, even at high latitude, increases in concentration with depth, and thus there should still be a positive anomaly associated with uplifted isopycnals in cyclonic eddies (blue points, Fig. 3.9c). The lack of positive nitrate anomaly could be due to errors in our calculations of the composites, perhaps associated with limited sample size. Alternatively, errors could arise from our use of climatology in the Southern ocean, which is based on a relatively limited number of hydrographic casts (*MacCready and Quay*, 2001). This may lead to moderate biases and would affect our calculations (Eq. 3.1).

We also see latitudinal differences in the relationship between r^2_{mono} and $|\Delta N_{av}|$ (Fig. 3.11). At low-latitude we see that both r^2_{mono} and $|\Delta N_{av}|$ are generally lower than at mid-latitude. Again, this may also be due to the different eddy SSH and nitracline characteristics between low- and mid-latitude. At mid-latitude, more effective eddy pumping likely creates a larger biological response (higher r^2_{mono}) than at low latitude. Once more, we do not observe obvious trends at high latitude, which may be because high latitude is generally under HNLC conditions and nitrate supply may not be strongly related to chlorophyll patterns.

The differences between nitrate anomalies determined on pressure surfaces and density surfaces (Fig. 3.13) strongly suggest that nitrate distribution in the upper ocean is primarily affected by isopycnal deflection within eddies, rather than other mechanisms such as diapycnal diffusive transport. Ultimately, the level of nitrate available for entrainment into the mixed layer will affect surface primary production and chlorophyll concentration, which is likely why we observe a strong correlation between the ΔN_{av} and ΔChl_{av}.

Previous studies suggest that mesoscale eddies are a net enhancer of biological production (*McGillicuddy et al.*, 2007; *Oschlies and Garcon*, 1998) driven by increased euphotic zone nitrate supplied by cyclonic eddies. Our results show the nitrate deficit in the euphotic zone caused by anticyclonic eddies is clearly associated with a decrease in surface chlorophyll, which is strongly suggestive of a reduction in biological production and biomass. One of the most intriguing aspects of this work is that the nutrient and chlorophyll anomalies in cyclonic and anticyclonic eddies are roughly opposite (Figs. 3.8 and 3.9). The discrepancy between our results and prior studies may hinge on the behavior of anticyclonic eddies. Past studies may assume that anticyclonic eddies drive no ecosystem response, while we find that anticyclonic eddies are likely important to the overall system and act to negate at least a large fraction of the nitrate supply from cyclonic eddies. Therefore, it will be critically important for future studies examining upper ocean primary production to consider the effects of anticyclonic eddies.

3.4.2 Wind speed, seasonality, and eddy age

We do not observe obvious trends in nitrate or chlorophyll anomaly associated with wind speed or seasonality, and only weak evidence of a correlation between nitrate and eddy age. It is not particularly surprising that we do not observe the expected effects of winds (Fig. 3.14a), as the strength of eddy-Ekman pumping may be less than eddy pumping by up to an order of magnitude (*Martin and Richards*, 2001). Many of the regions used in our analysis have relatively few hydrographic casts coincident with eddies, so we may lack the requisite sample size to resolve weak signals induced by surface winds.

We might expect that seasonality could affect the nitrate anomaly in eddies. For example, the nitrate made available by cyclonic eddies in the summer might be more quickly absorbed by phytoplankton than in cyclonic eddies in the winter (which would change the ΔN_{av} signature). However, we observe no significant differences between ΔN_{av} in summertime eddies and wintertime eddies (Fig. 3.14b).

We observe a significant effect of eddy age on the nitrate anomaly. Presumably, newly formed eddies have an initial nutrient anomaly (positive in cyclones and negative in anticyclones). The slope of the regression (Fig. 3.14c) suggests that the initial anomaly found in younger eddies decreases as eddies age. Yet, inspection of the data does not inspire great confidence that the effect of eddy age is strong, particularly with the cyclonic eddy observations (Fig. 3.14c, blue points). Moderate changes in the 3 week threshold (see Section 3.2.6) do not qualitatively change these interpretations. Additionally, due to fairly low sample sizes in many regions we are unable to analyze these trends in finer resolution (e.g. a week by week evolution of the nitrate anomaly).

We expect the biological response to a nitrate injection act rapidly (*Johnson et al.*, 2010), so perhaps the remaining anomaly in older eddies is not accessible for biological uptake. For example, it is certainly possible that not all the nitrate surplus in the upper 200 m (the depth interval of integration in Eq. 3.2) is within the euphotic zone if the water is turbid. Alternatively, eddies could be leaky (*Haller and Beron-Vera*, 2013) and cyclonic eddy formation does not represent a one-time injection to the surface of the ocean, but rather it is a continuous process, so uptake of nitrate is balanced by supply from nutrient rich waters outside the eddy. This latter scenario would have large implications on the role eddies are thought to have in supply of nutrients to the surface.

3.5 Conclusions

This work represents a step forward in resolving the role of eddies in the global nutrient distribution and surface chlorophyll expression. Based on *in situ* hydrographic observations we have created composite averages of mesoscale eddies, allowing us to build a global map of the variability of vertical nutrient flux due to eddy pumping.

We have also established a significant relationship between nitrate supply driven by eddy pumping and surface chlorophyll expression at low- to mid-latitude, but not at high latitude where micronutrients and light may limit growth (Fig. 3.9). We suggest that eddy pumping is the primary factor in shaping nutrient availability. Eddy age may have a small effect, and that other influences, such as seasonality and wind speed do not, in general, have strong effects on the nitrate anomaly.

We find that the nutrient supply of cyclones is approximately matched by the nutrient deficit created in anticyclones. This nutrient deficit is connected with a decrease in chlorophyll (which may suggest lower biomass and biological production of organic matter). Mesoscale eddies as a whole are often thought of as a boon to photosynthetic productivity, which is partly based on the nutrient supply driven by doming isopycnals in cyclonic eddies.

Anticyclonic eddies constitute roughly half of the overall eddy population which suggests, based on this work, that as a whole the enhancements in productivity in cyclonic eddies are at least partially mitigated by decreases in anticyclonic eddies.

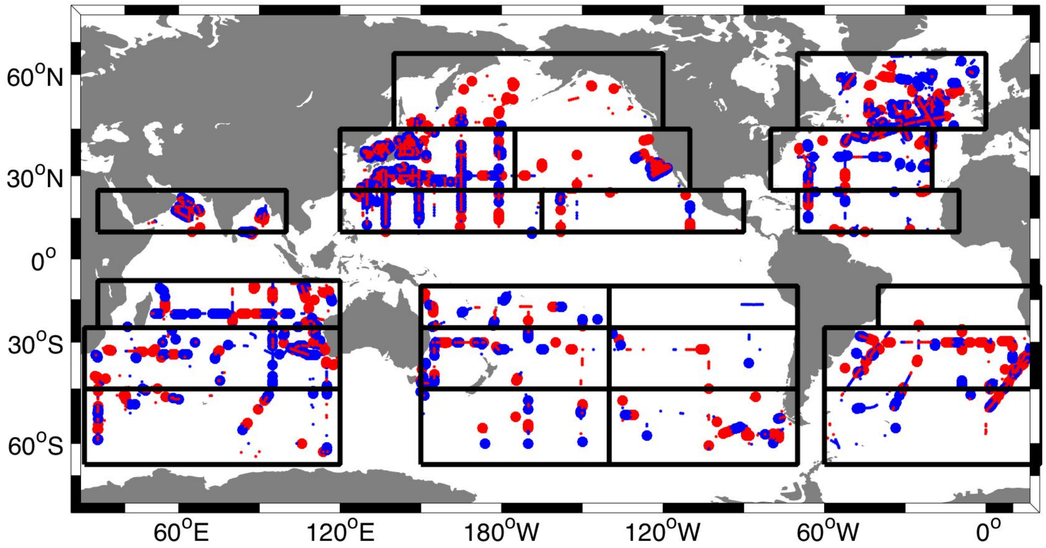

Figure 3.1: Black boxes show the spatial domain for the regions used in analysis. Blue points represent observations of cyclonic eddies, and red points represent observations of anti-cyclonic eddies. Large points indicate World Ocean Database (WOD) casts that fell within one eddy radius, and small points represent casts that fell within three eddy radii. All casts shown here fall between 1992 and 2012.

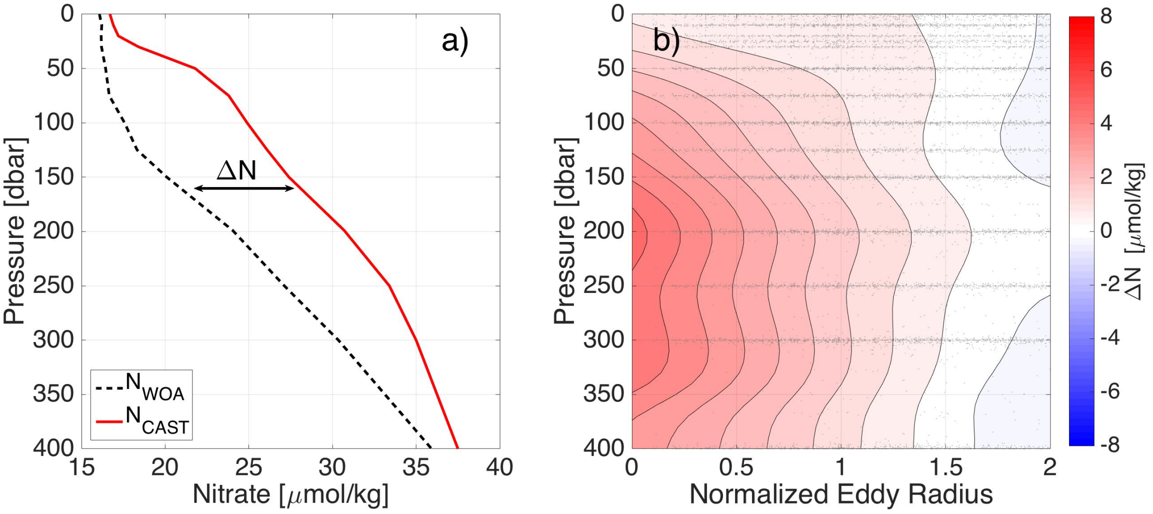

Figure 3.2: a) An example of calculating the nitrate anomaly (ΔN) for a cast inside a cyclonic eddy in the Northwest Pacific. The red line is the observed nitrate from hydrography and the dashed black line is what is expected based on climatologoy. b) The composite interior of the nitrate anomaly of a cyclonic eddy, constructed from many hydrographic observations (measurement locations indicated by grey dots). Red indicates higher nitrate concentrations than expected from climatology, and conversely blue represents a nitrate deficit (deficits are not prevalent in this figure, but strong in anticyclonic cases; see Fig. 3.5).

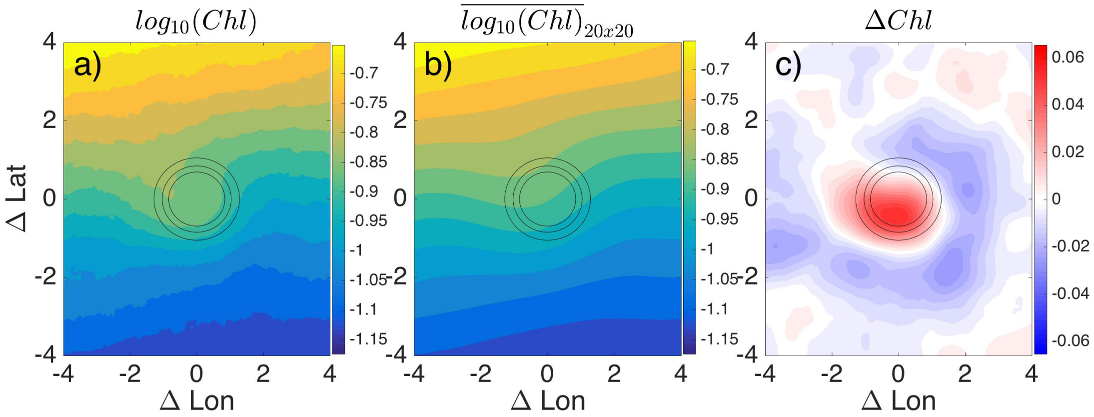

Figure 3.3: a) The average chlorophyll concentration (log-transformed) compiled from thousands of satellite observations of chlorophyll in and around cyclonic eddies in the Northwest Pacific. b) The smoothed average of (a), where we calculate a 20 by 20 pixel running average (in both latitude and longitude). c) The difference between (a) and (b), which we use as an estimate of the chlorophyll anomaly. Black lines represent the diameter of the eddies used in the ensemble averages (25%, 50%, and 75% percentiles of diamter are plotted). ΔChl is unitless because of the logarithm applied to the chlorophyll concentration [mg/m^3].

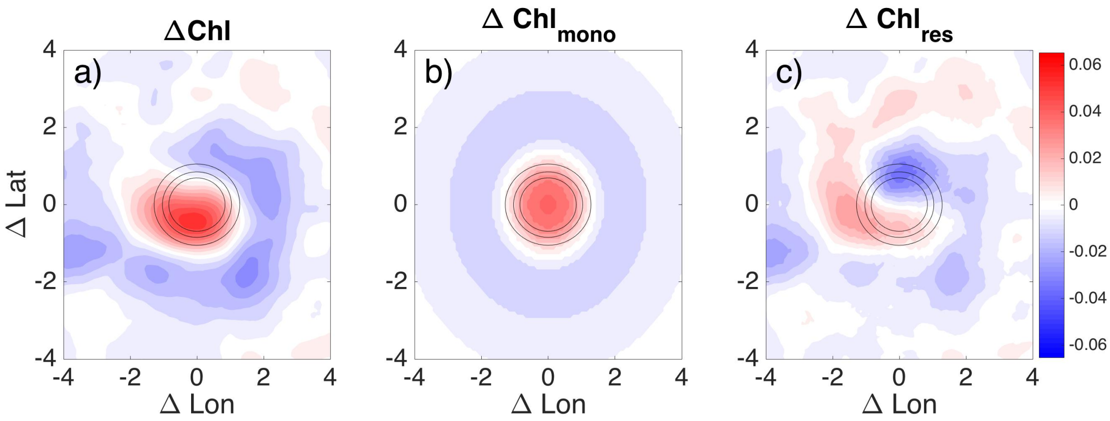

Figure 3.4: a) the chlorophyll anomaly (as in Fig. 3.3c). b) The chlorophyll monopole, which we define as the radial average of the chlorophyll anomaly. c) The chlorophyll residual (ΔChl_{res}), which we define as the difference between (a) and (b). We treat (b) as the chlorophyll signature induced by eddy pumping, while (c), the residual, shows distinct signs of eddy advection. As in Fig. 3.3, black lines represent the diameter of the eddies used in the ensemble averages (25%, 50%, and 75% percentiles of diameter are plotted).

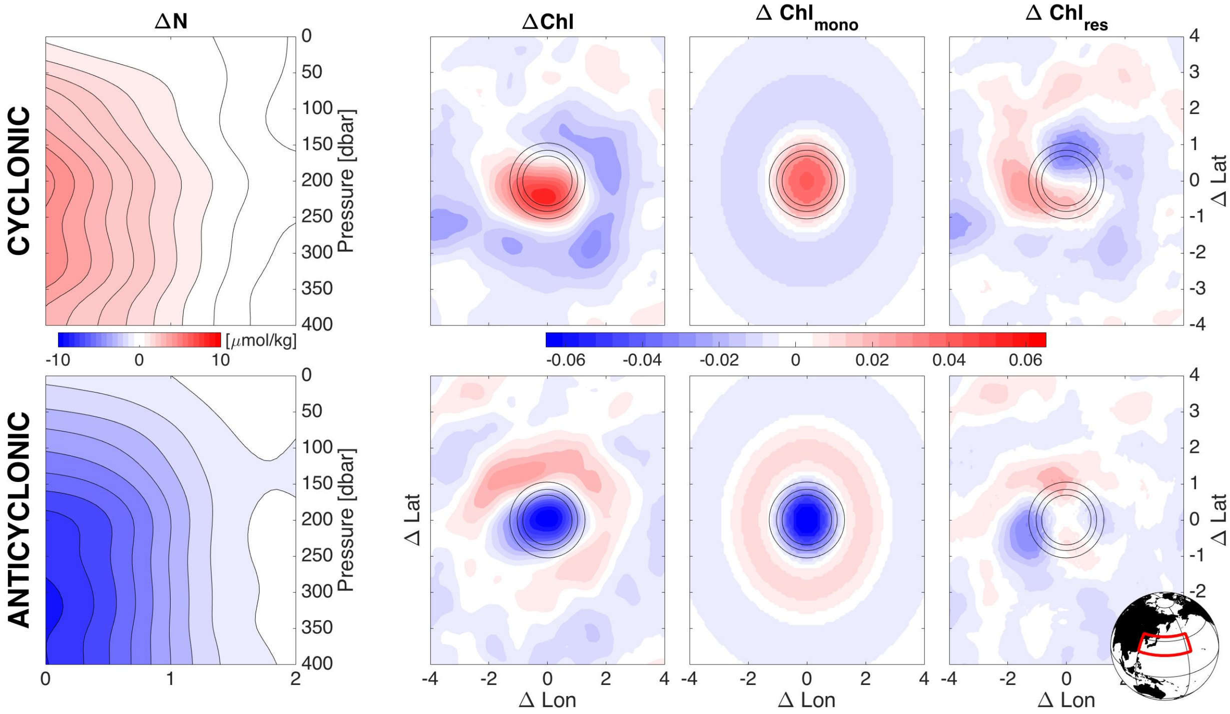

Figure 3.5: Summary figure for the northwest Pacific region (domain shown in small globe). a) The nitrate anomaly as in Fig 3.2b. c-d) ΔChl, ΔChl_{mono}, ΔChl_{res}, as in Fig. 3.4. e-h) Same as a-d, but for anticyclonic eddies in the northwest Pacific.

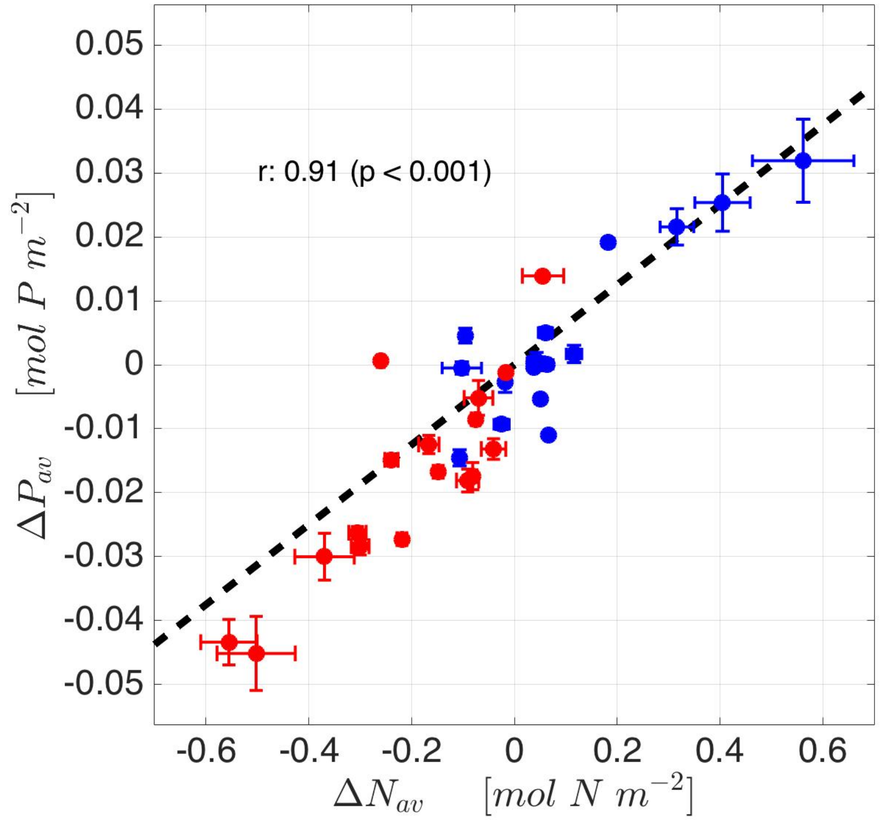

Figure 3.6: The relationship between the nitrate anomaly and the phosphate anomaly, globally. Each region used (17 total) yields one data point for cyclonic eddies (blue) and anticyclonic eddies (red) based on the local estimates of ΔN_{av} and ΔP_{av}. The dashed black line is the Redfield ratio (16N:1P; *Anderson and Sarmiento* (1994)).

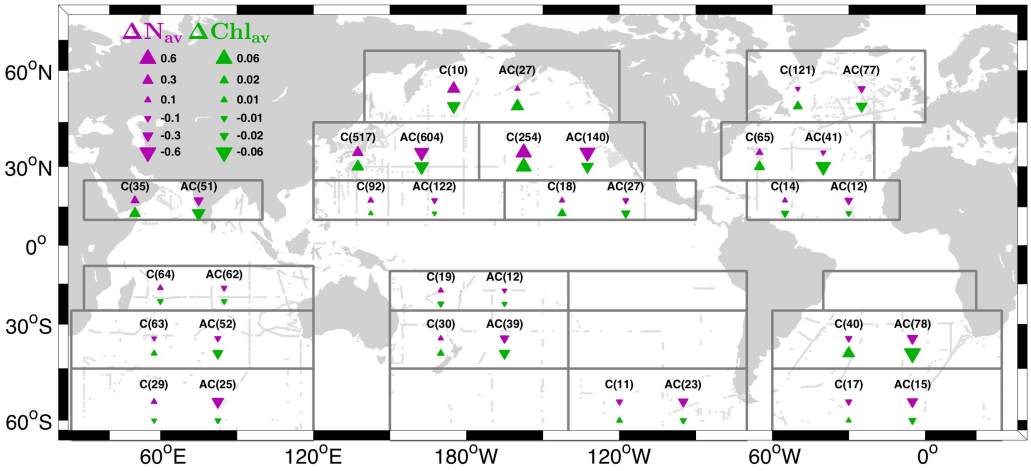

Figure 3.7: A summary of ΔN_{av} and ΔChl_{av} in each region examined (grey boxes). The arrows represent the sign and magnitude of ΔN_{av} (purple) and ΔChl_{av} (green). The numbers in parenthesis are the number of hydrographic casts that occurred within one radius of cyclonic (C) and anticyclonic (AC) eddies. The units of ΔN_{av} are mol N m^{-2}. Empty boxes contain less than 10 casts coincident with Chelton eddies.

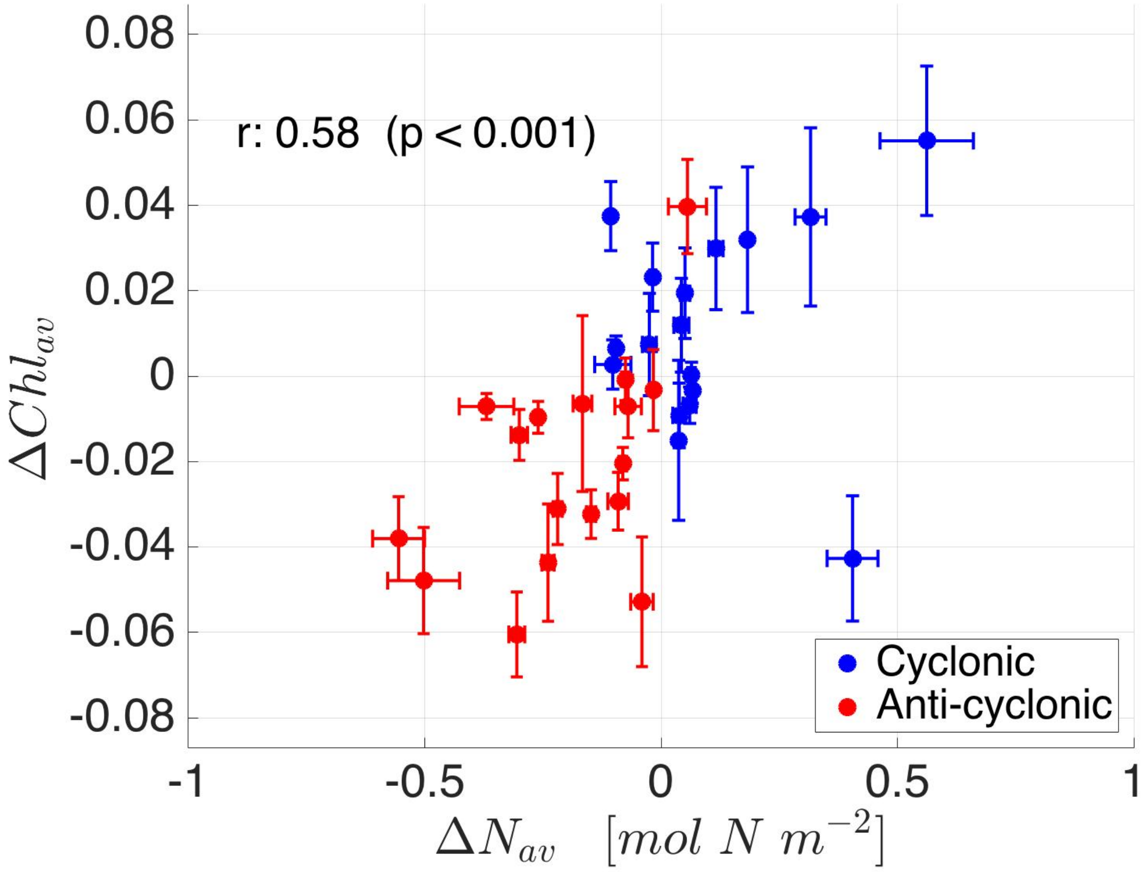

Figure 3.8: The relationship between the nitrate anomaly and the chlorophyll anomaly, globally. Each region used (17 total) yields a data point for the cyclonic (blue) and anticyclonic (red) composite eddy based on the local estimates of ΔN_{av} and ΔChl_{av}. The correlation coefficient (r) is given in the upper left, as well as the p-value, which tests if the correlation is significantly different from zero.

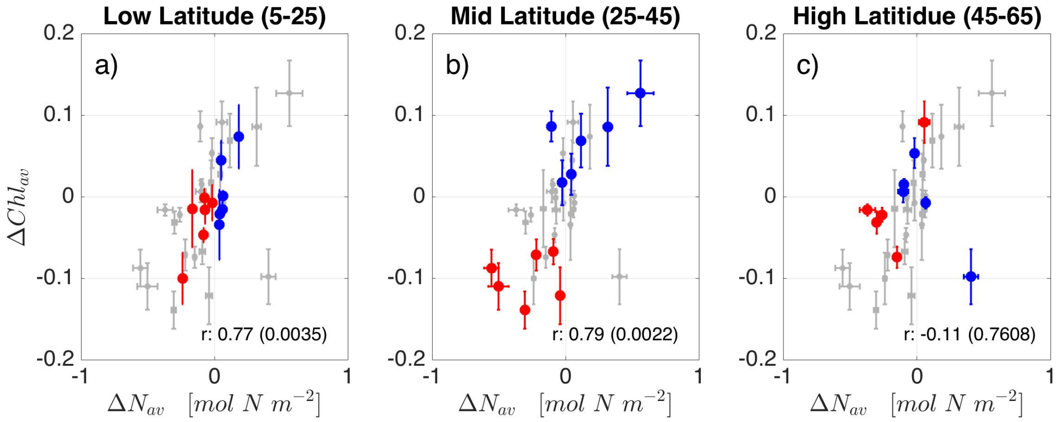

Figure 3.9: Same as Fig. 3.8, but now broken into low, mid, and high latitude categories (panels a, b, and c, respectively). Once again, data from composite cyclonic eddies are represented by blue, and data of composite anticyclonic eddies are red. Grey points are global data that do not fall in that particular latitude range. Both northern and southern hemispheres are included in latitude ranges. The correlation coefficient, r, is calculated from only the points within the latitude range (i.e. blue and red points), and the p-value is in parenthesis.

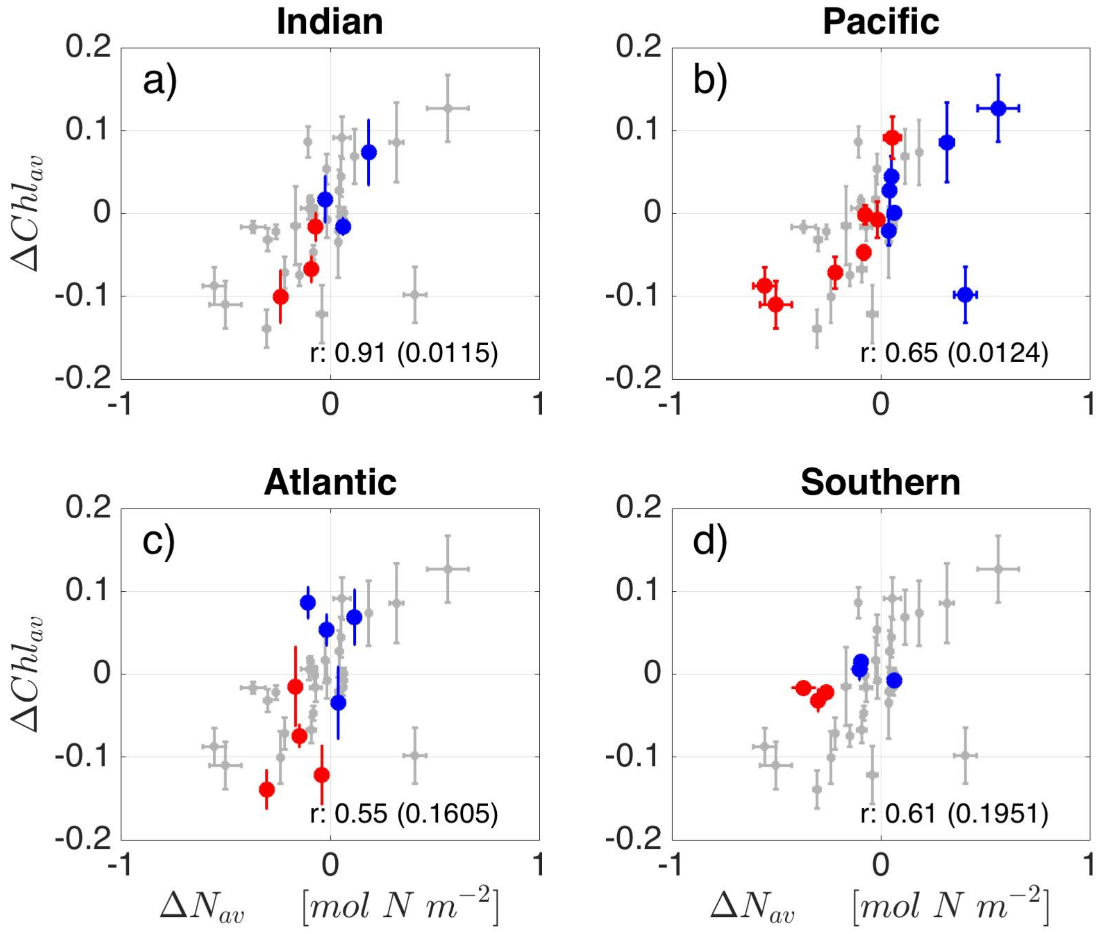

Figure 3.10: Same as Fig. 3.9, but here we delineate between ocean basins. The Southern Ocean is defined as south of 45^{o}S.

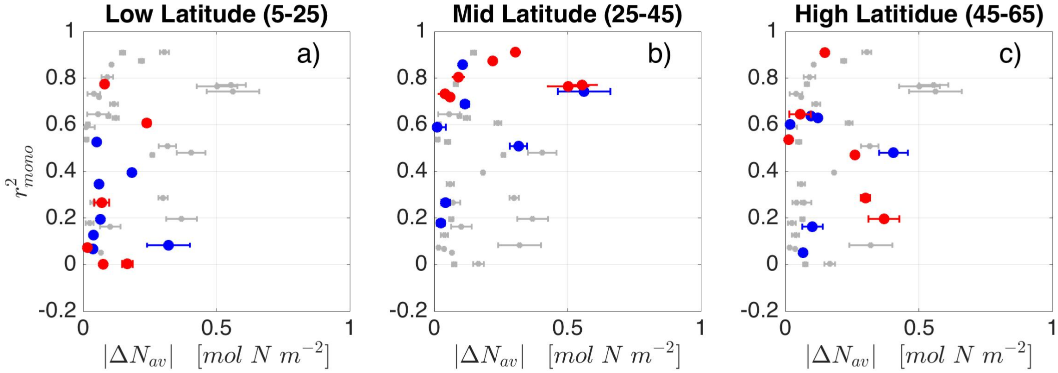

Figure 3.11: Similar to Figs. 3.8-3.10, however now we plot the absolute value of ΔN_{av} against r^2_{mono} (Eqs. 3.2 and 3.5, respectively) for low, mid, and high latitudes (panels a, b, and c, respectively). Each point corresponds to an estimate from one region (Fig. 3.7), where blue points correspond to cyclonic eddies and red points correspond to anticyclonic eddies.

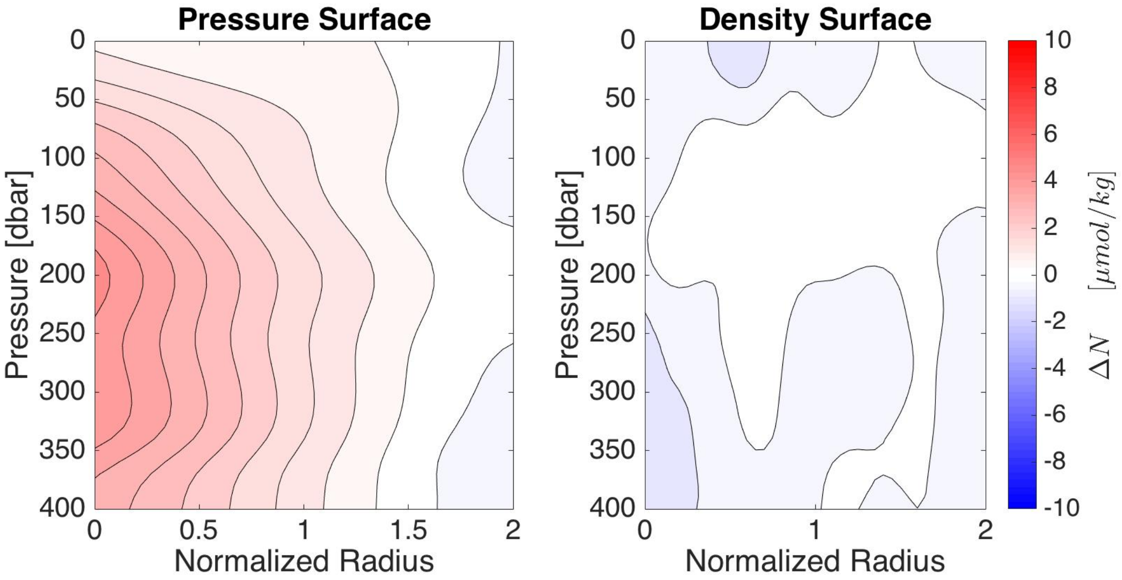

Figure 3.12: Left panel: The nitrate anomaly determined from pressure surfaces (as in Fig. 3.2). Right panel: The nitrate anomaly determined from density surface analysis, transformed back to pressure coordinates (see Section 3.2.3).

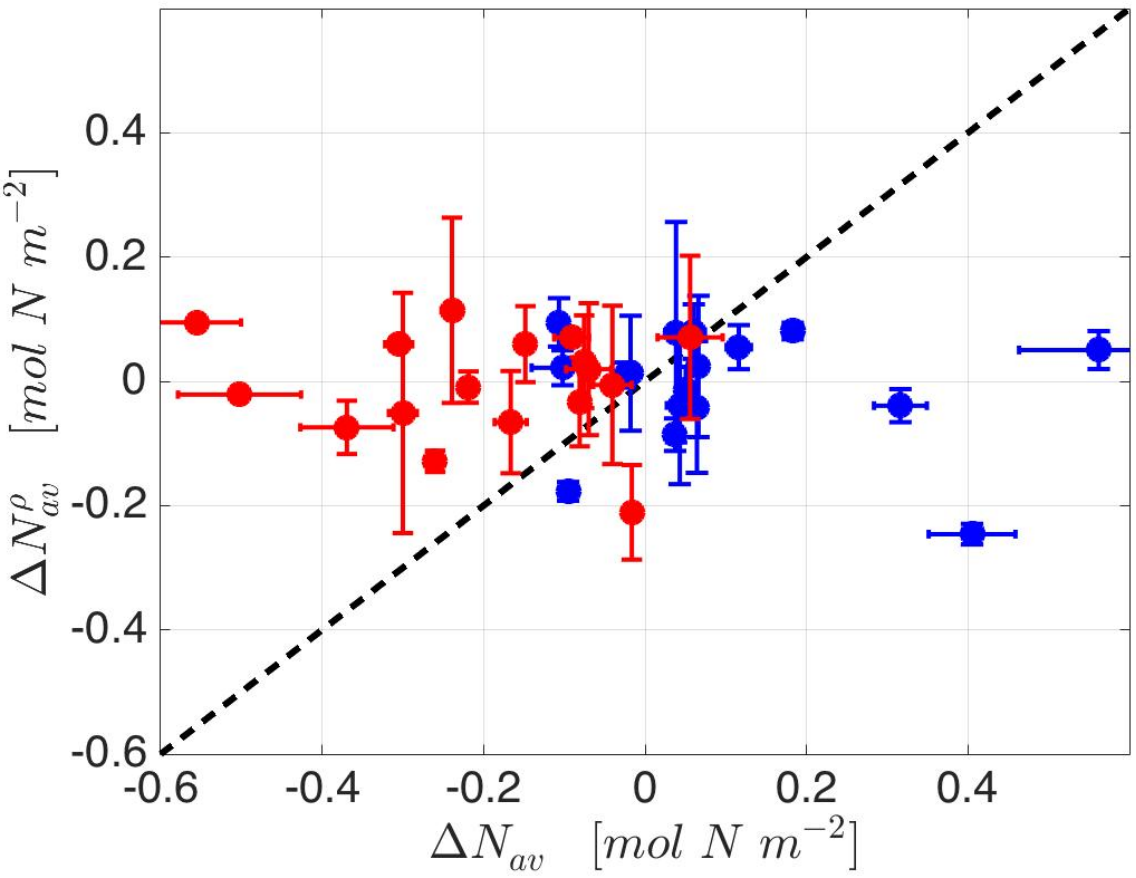

Figure 3.13: The relationship between the depth integrated nitrate anomaly determined on pressure surfaces (ΔN_{av}) and density surfaces (ΔN_{av}^{ρ}). As in Figs. 3.8-3.11 each point represents a cyclonic (blue) or anticyclonic (red) estimate from one region (Fig. 3.1). The dashed black line shows the 1:1 relationship.

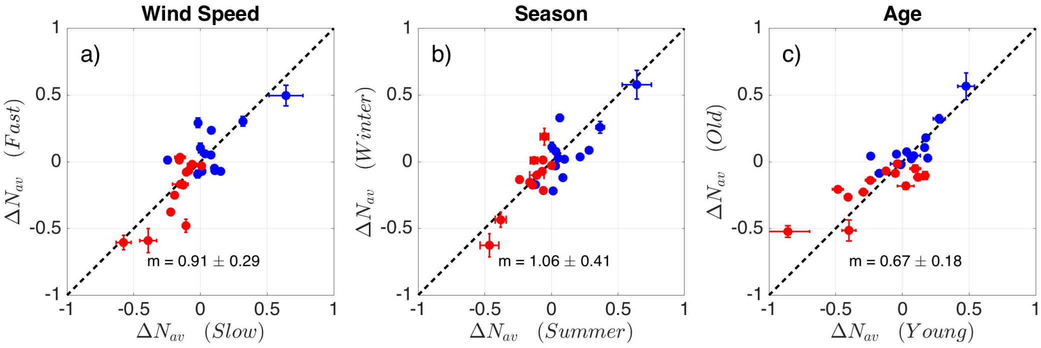

Figure 3.14: a) Nitrate anomaly under slow wind conditions against nitrate anomaly under fast wind conditions. b) Nitrate anomaly in summer months against nitrate anomaly in winter months. c) Nitrate anomaly in young eddies against nitrate anomaly for old eddies. The black dashed line is the the 1:1 line. We also present the slope of the linear regression, m, with the 95% confidence interval. The units for both horizontal and vertical axis are mol N m^{-2}.

SUMMARY

The work herein has used many datasets to determine the large-scale behavior of several physical and biogeochemical phenomena in the ocean.

In Chapter 1, we see that Argo floats that collect park-phase measurements are capable of accurately estimating internal gravity wave displacement. The global patterns of internal wave intensity are strongly heterogeneous and bear striking resemblance to recent estimates of diapycnal diffusivity (*Whalen et al.*, 2012), which supports the notation that breaking internal waves are one of the primary mechanisms responsible for abyssal mixing. Internal waves are found to be positively correlated with seafloor roughness as well as proximity to the seafloor itself, a result that is analogous to the patterns observe by *Polzin et al.* (1997). We also examine how the observed internal wave field compares to Garrett-Munk expectations (*Garrett and Munk*, 1975). Averaged globally, the float-observed internal waves approximately match what is predicted by the Garrett-Munk parameterization. However, there is a large deviation at high latitude, possibly due to inadequate parameterization at high latitude. Additionally, we also demonstrate that even though Argo observations are usually most instructive on broad spatial scales (> 100 km), floats are capable of capturing finer processes as well (~ 10 km), in the case of the seamount-trapped interal waves presented in Section 1.3.2.

In Chapter 2, we demonstrate that Argo floats equipped with dissolved oxygen sensors can be quite useful in quantifying biogeochemical processes (in addition to physical phenomena). Respiration profiles and depth-integrated respiration is quantified across eight geographically distinct regions, revealing strong variability in the overall magnitude and depth structure of respiration. We use depth-integrated respiration to estimate a lower bound for organic carbon export from the upper $\sim$70 m of the ocean. We also employ satellite observations of net primary production to formulate estimates of export efficiency. We find that export and export efficiency are both low at low-latitude and higher at high-latitude, consistent with expectations (*Laws et al.*, 2000; *Dunne et al*, 2005). By comparing our results to independent studies (*Midorikawa et al.*, 2002; *Emerson*, 2014), we find that float-based estimates of export are likely too low at weakly seasonal locations, where oxygen is largely at steady-state. Examination of the seasonality of both NPP and MLD shows that this oxygen-based method of determining respiration will perform well for most locations poleward of $\sim 30^o$, and likely underestimate respiration at lower latitudes.

In Chapter 3, we use the WOD dataset as our primary *in situ* observations because of the relative abundance of nitrate and phosphate samples. In addition to WOD, we employ several other global datasets to estimate the influence of mesoscale eddies on nutrient availability and surface chlorophyll concentration. We find that behavior is not globally uniform, where at low- and mid-latitude nutrient availability is significantly correlated to chlorophyll concentration. Yet at high-latitude we observe no such trend, likely because micronutrients (e.g. iron) or light, rather than nitrate, are limiting phytoplankton growth. The effects of surface wind speed and seasonality are not found to have a significant impact on nutrient availability within eddies. Finally, the stark contrast between the nitrate anomaly on pressure and density surfaces strongly suggests that the vertical heaving of isopycnals within eddies is the dominant factor in redistributing nutrients, over other processes like diapycnal diffusive flux.

BIBLIOGRAPHY

Alford, M. H. (2003). Redistribution of energy available for ocean mixing by the long-wave propagation of internal waves. *Nature*, **423**, 159-162.

Alford, M. H., and M. Whitmont (2007). Seasonal and Spatial Variability of Near-Inertial Kinetic Energy from Historical Moored Velocity Records. *Journal of Physical Oceanography*, **37 (8)**, 2022-2037, doi:10.1175/JPO3106.1.

Alford, M. H., and Z. Zhao (2007). Global Patterns of Low-Mode Internal-Wave Propagation Part I: Energy and Energy Flux. *Journal of Physical Oceanography*, **37 (7)**, 1829-1848, doi:10.1175/JPO3085.1.

Amante, C., and B. Eakins (2009). ETOPO1: 1 arc-minute relief model: Procedures data sources and analysis. NOAA technical Memo. NESDIS NGDC-24, 19pp..

Anderson, L. A. and J. L. Sarmiento. (1994). Redfield ratios of remineralization determined by nutrient data analysis. *Global biogeochemical cycles*, 8, 65–80.

Antonov, J. I., and Coauthors (2010). S. Levitus, Ed. NOAA Atlas NESDIS 69, U.S. Government Printing Oce, Washington, D.C., 184 pp..

Barnes, S. L. (1994a). Applications of the Barnes objective analysis scheme: Part I: effects of undersampling, wave position, and station randomness. *J. of Atmos. and Oceanic Tech.*, **11**, 1433-1448.

Barnes, S. L. (1994b). Applications of the Barnes objective analysis scheme: Part II: Improving derivative estimates. *J. of Atmos. and Oceanic Tech.*, **11**, 1449-1458.

Barnes, S. L. (1994c). Applications of the Barnes objective analysis scheme: Part III: Tuning for minimum error. *J. of Atmos. and Oceanic Tech.*, **11**, 1459-1479.

Behrenfeld, M. J. and P. G. Falkowski. (1997). Photosynthetic rates derived from satellite-based chlorophyll concentration. *Limnology and Oceanography*, 42, 1–20.

Behrenfeld, M. J., and Coauthors (2016). Revaluating ocean warming impacts on global phytoplankton.. *Nature Climate Change*, **6**, 323-330.

de Boyer Montégut, T.P., J. I. Antonov, O. K. Baranova, C. Coleman, H. E. Garcia, A. Grodsky, D. R. Johnson, R. A. Locarnini, A. V. Mishonov, T.D. O'Brien, C.R. Paver, J.R. Reagan, D. Seidov, I. V. Smolyar, and M. M. Zweng, 2013: World Ocean Database 2013, NOAA Atlas NESDIS 72, S. Levitus, Ed., A. Mishonov, Technical Ed.; Silver Spring, MD, 209 pp., http://doi.org/10.7289/V5NZ85MT

Buesseler, K. O., C. H. Lamborg, P. W. Boyd, P. J. Lam, T. W. Trull, R. R. Bidigare, J. K. B. Bishop, K. L. Casciotti, F. Dehairs, M. Elskens, M. Honda, D. M. Karl, D. A., Siegel, M. W. Silver, D. K. Steinberg, J. Valdes, B. Van Mooy, and S. Wilson (2007). Revisiting carbon flux through the ocean's twilight zone. *Science*, **316**, 567–570.

Bushinsky, S. M. and S. Emerson (2013). A method for in-situ calibration of Aanderaa oxygen sensors on surface moorings. *Marine Chemistry*, **155**, 22–28, doi:10.1016/j.marchem.2013.05.001

Cairns, J. L., and G. O. Williams (1976). Internal Wave Observations from a midwater float. *J. Geophys. Res.*, **81**, 1943-1950.

Castelao, R. M. (2014). Mesoscale eddies in the South Atlantic Bight and the Gulf Stream Recirculation region: Vertical Structure. *Journal of Geophysical Research: Oceans*, **119**, 2048-2065, doi:10.1002/2014JC009796.

Chelton, D. B., P. Gaube, M. G. Schlax, J. J. Early, and R. M. Samelson (2011a). The influence of nonlinear mesoscale eddies on near-surface oceanic chlorophyll. *Science*, **334 (6054)**, 328-32, doi:10.1126/science.1208897.

Chelton, D. B., M. G. Schlax, and R. M. Samelson (2011b). Global observations of nonlinear mesoscale eddies. *Progress in Oceanography*, **91 (2)**, 167-2016, doi:10.1016/j.pocean.2011.01.002.

Chisholm, S., and F. Morel (1991). What contols phytoplankton production in nutrient-rich areas of the open sea?. *Limnol. Oceanogr.*, **36**, 1507-1965.

de Boyer Montegut, C., G. Madec, A. S. Fishcer, A. Lazar, and D. Ludicone (2004). Mixed layer depth over the global ocean: an examination of profile data and a profile-based climatology. *J Geophys. Res.*, **109**, C12003. doi:10.1029/2004JC002378.

Dunne, J. P., R. A. Armstrong, A. Gnanadesikan, and J. L. Sarmiento (2005). Empirical and mechanistic models for the particle export ratio. *Global Biogeochemical Cycles*, **19**, GB4026, doi:10.1029/2004GB002390.

Egbert, G. A., A. Bennet, and M. Foreman (1994). TOPEX/POSEIDON tides estimated using a global inverse model. *Journal of Geophysical Research*, **99**, 821-852.

Emerson, S. (2014). Annual net community production and the biological carbon flux in the ocean. *Global Biogeochemical Cycles*, **28**, 14–28, doi:10.1002/2013GB004680.

Emerson, S., P. Quay, D. Karl, C. Winn, L. Tupas, and M. Landry (1997). Experimental determination of the organic carbon flux from open-ocean surface waters (1997). *Nature*, **389**, 951-954.

Eppley, R. W., and B. J. Peterson (1979). Particulate organic matter flux and planktonic new production in the deep ocean. *Nature*, **282**, 677–680.

Eriksen, C. (1991). Observations of amplified flows atop a large seamount.. *Journal of Geophysical Research*, **96 (C8)**, 1-13.

Esaias, W. E., M. R. Abbott, I. Barton, O. B. Brown, J. W. Campbell, K. L. Carder, D. K. Clark, R. H. Evans, F. E. Hoge, H. R. Gordon, W. M. Balch, R. Letelier, and P. J. Minnett (1998). An Overview of MODIS Capabilties for Ocean Science Observations. *IEEE Transactions on Geoscience and Remote Sensing*, **36(4)**, 1250–1265.

Falkowski, P. D. Ziemann, Z. Kolber, and P. Bienfang (1991). Role of eddy pumping in enhancing primary production in the ocean. *Letters to Nature*, **352**, 55-58.

Field, C. B., M. J. Behrenfeld, J. T. Randerson, and P. Falkowski (1998). Primary Production of the Biosphere: Integrating Terrestrial and Oceanic Components. *Science*, **281**, 237–240, doi:10.1126/science.281.5374.237

Frenger, I. M. Munnich, N. Gruber, and R. Knutti (2015). Southern Ocean eddy phenomenology. *Journal of Geophysical Research: Oceans*, **120**, doi:10.1002/2014JC010632.

Garcia, H. E., R. A. Locarnini, T. P. Boyer, J. I. Antonov, M. M. Zweng, O. K. Baranova, and D. R. Johnson (2010a). World Ocean Atlas 2009, Volume 4: Nutrients (phosphate, nitrate, silicate). S. Levitus, Ed. NOAA Atlas NESDIS 71, U.S. Government Printing Office, Washington, D.C. 398 pp.

Garcia, H., R. Locarnini, T. Boyer, J. Antonov, O. Baranova, M. Zweng, and D. Johnson (2010). *World Ocean Atlas 2009, Volume 3: Dissolved Oxygen, Apparent Oxygen Utilization, and Oxygen Saturation.* S. Levitus, Ed. NOAA Atlas SESDIS 70, U.S. Government Printing Office, Washington, D.C., 344 pp.

Garrett, C. and W. Munk (1975). Space-time scales of internal waves: A progress report. *Journal of Geophysical Research*, **80 (3)**, 291-297.

Gordon, H. R., and W. R. McCluney (1975). Estimation of the depth of sunlight penetration in the sea for remote sensing. *Applied optics*, **14(2)**, 413–416.

Gregg, M. (1989). Scaling turbulent dissipation in the thermocline. *Journal of Geophysical Research*, **94 (C7)**, 9686-9698.

Gruber, N., S. C. Doney, S. R. Emerson, D. Gilbert, T. Kobayashi, A. Körtzinger, G. C. Johnson, K. S. Johnson, S. C. Riser, and O. Ulloa (2007). The Argo-Oxygen Program. (White Paper), http://www-argo.ucsd.edu/o2_white_paper_web.pdf.

Haller, G., F. J. Beron-Vera (2013). Coherent Lagrangian vorticies: the black holes of turbulence. *Journal of Fluid Mechanics*, **731**, R4, doi:10.1017/jfm.2013.391.

Hansell, D. A., and , C. A. Carlson (1998). Deep-ocean gradients in the concentration of dissolved organic carbon. *Nature*, **395**, 263–266.

Henson, S. A., R. Sanders, E. Madsen, P. J. Morris, , F. Le Moigne, and G. D. Quartly (2011). A reduced estimate of the strength of the ocean's biological carbon pump. *Geophysical Research Letters*, **38**, L04606, doi:10.1029/2011GL046735.

Henson, S. A., R. Sanders, and E. Madsen (2012). Global patterns in efficiency of particulate organic carbon export and transfer to the deep ocean. *Global Biogeochemical Cycles*, **26**, GB1028, doi:10.1029/2011GB004099.

Hirata, T., N. J. Hardman-Mountford, R. J. W. Brewin, J. Aiken, R. Barlow, K. Suzuki, T. Isada, E. Howell, T. Hashioka, M. Noguchi-Aita, and Y. Yamanaka (2011). Synoptic relationships between surface Chlorophyll a and diagnostic pigments specific to phytoplankton functional types. *Biogeosciences*, **8**, 311–327. doi:10.5194/bg-8-311-2011

Hooker, S. B., and C. R. McClain (2000). The calibration and validation of SeaWiFS data. *Progress in Oceanography*, **45**, 427–465.

Hovis, W. A., D. K. Clark, F. Anderson, R. W. Austin, W. H. Wilson, E. T. Baker, D. Ball, H. R. Gordon, J. T. Mueller, S. Z. El-Sayed, B. Sturm, R. C. Wrigley, and C. S. Yentsch (1980). Nimbus-7 Coastal Zone Color Scanner: System Description and Initial Imagery. *Science*, **210**, 60–63.

Johnson, K. S., S. C. Riser, and D. M. Karl (2010). Nitrate supply from deep to near-surface waters of the North Pacific subtropical gyre. *Nature*, **465**, 1062-1065, doi:10.1016/j.dsr2.2008.01.012.

Kalnay et al. (1996). The NCEP/NCAR 40-year reanalysis project, Bull. Amer. Meteor. Soc., **77**, 437-470.

Karl, D. M., and M. J. Church (2014). Microbial oceanography and the Hawaii Ocean Time-series programme. *Nature Reviews: Microbiology*, **12**, 699-713.

Karl, D. M. and R. Lukas. (1996). The Hawaii Ocean Time-series (HOT) program: Background, rationale and field implementation. *Deep Sea Research Part II: Topical Studies in Oceanography*, 43, 129–156, doi:10.1016/0967-0645(96)00005-7

Kostadinov, T. S., D. A. Siegel, and S. Maritorena (2009). Retrieval of the particle size distribution from satellite ocean color observations. *Journal of Geophysical Research*, 114, C09015, doi:10.1029/2009JC005303.

Kunze, E. (1985). Near-inertial wave propagation in geostrophic shear. *Journal of Physical Oceanography*, **15 (5)**, 544-565.

Kunze, E., E. Firing, J. M. Hummon, T. K. Chereskin, and A. M. Thurnherr (2006). Global abyssal mixing infered from lowered ADCP shear and CTD strain profiles. *Journal of Physical Oceangraphy*, **19**, 1553-1576.

Laws, E. A., P. G. Falkowski, W. O. Smith Jr., H. Ducklow, and J. J. McCarthy, (2000). Temperature effects on export production in the open ocean. *Global Biogeochemical Cycles*, **14(4)**, 1231–1246.

Ledwell, J., A. J. Watson, and C. S. Law (1993). Evidence for slow mixing across the pycnocline from an open-ocean tracer-release experiment. *Nature*, **364**, 701–703.

Ledwell, J., E. Montgomery, K. Polzin, L. C. St. Laurent, R. Schmitt, and J. Toole (2000). Evidence for enhanced mixing over rough topography in the abyssal ocean. *Nature*, **403**, 179-82, doi:10.1038/35003164.

Levine, M. (2002). A modification of the Garrett-Munk internal wave spectrum. *Journal of Physical Oceanography*, **32 (11)**, 3166-3181.

Lewis, M., and W. Harrison (1986). Vertical Nitrate Fluxes in the Oligotrophic Ocean. *Science*, **234**, 870-873.

Locarnini, R. A., A. V. Mishonov, J. I. Antonov, T. P. Boyer, H. E. Garcia, O. K. Baranova, M. M. Zweng, and D. R. Johnson (2010). St. Levitus, Ed. NOAA Atlas NESDIS 68, U.S. Government Printing Office, Washington, D.C. 184 pp.

Lumpkin, R., and G. C. Johnson (2013). Global ocean surface velocities from drifters: Mean, variance, El Niño Southern Oscillation response, and seasonal cycle. *J. Geophys. Res. Oceans*, **118**, 2992-3006.

MacCready, P. and P. Quay (2001). Biological export flux in the Southern Ocean estimated from a climatological nitrate budget. *Deep Sea Research Part II*, **48**, 4299-4322.

Mahadevan, A., E. D'Asaro, C. Lee, and M. J. Perry (2012). Eddy-driven stratification initiates North Atlantic spring phytoplankton blooms. *Science*, **337**, 54-58, doi:10.1126/science.1218740.

Marra, J., R. Bidigare, and T. Dicky (1990). Nutrients and mixing, chlorophyll and phytoplankton growth. *Deep Sea Research Part A*, **37(1)**, 127-143.

Martin, J. H., G. A. Knauer, D. M. Karl, and W. W. Broenkow (1987). VERTEX: carbon cycling in the northeast Pacific. *Deep Sea Research Part A: Oceanographic Research Papers*, **34(2)**, 267-285, doi:10.1016/0198-0149.

Martin, P., R. S. Lampitt, M. Jane Perry, R. Sanders, C. Lee, and E. D'Asaro (2011). Export and mesopelagic particle flux during a North Atlantic spring diatom bloom. *Deep-Sea Research Part I: Oceanographic Research Papers*, **58(4)**, 338–349, doi:10.1016/j.dsr.2011.01.006.

Martin, A., and K. Richards (2001). Mechanisms for vertical nutrient transport within a North Atlantic mesoscale eddy.. *Deep Sea Research Part A*, **48**, 757-773.

Martz, T. R., K. S. Johnson, and S. C. Riser (2008). Ocean metabolism observed with oxygen sensors on profiling floats in the South Pacific. *Limnology and Oceanography*, 53(5-2), 2094–2111.

McGillicuddy, D., L. Anderson, and N. Bates (2007). Eddy / Wind Interactions Stimulate extraordinary mid-ocean plankton blooms. *Science*, **316**, 1021-1027.

McNeil, J., and H. Jannasch (1999). New chemical biooptical and physical observations of upper ocean response to the passage of a mesoscale eddy off Bermuda. *Journal of Geophysical Research*, **104**, 537-548.

Michaels, A. F., and A. H. Knap (1996). Overview of the U.S. JGOFS Bermuda Atlantic Time-series Study and the Hydrostation S program. *Deep Sea Research Part II: Topical Studies in Oceanography*, **43(2–3)**, 157–198.

Michaels, A. F., and M. W. Silver (1988). Primary production, sinking fluxes and the microbial food web. *Deep Sea Research*, **35(4)**, 473–490.

Midorikawa, T., T. Umeda, N. Hiraishi, K. Ogawa, K. Nemoto, N. Kubo, and M. Ishii (2002). Estimation of seasonal net community production and airsea CO2 flux based on the carbon budget above the temperature minimum layer in the western subarctic North Pacific. *Deep Sea Research Part I*, 49, 339–362.

Monterey, G., and S. Levitus (1997). *Seasonal Variability of Mixed Layer Depth for the World Ocean, NOAA Atlas NESDIS 14*, 100 pp., Natl. Oceanic and Atmos. Admin., Silver Spring, MD.

Munk, W. (1966). Abyssal recipes. *Deep Sea Research and Oceanographic Abstracts*, **13 (4)**, 707-730, doi:10.1016/0011-7471(66)90602-4.

Munk, W., and C. Wunsch (1998). Abyssal Recipies II: energetics of tidal and wind mixing. *Deep Sea Research I: Oceanographic Research Papers*, **45 (12)**, 1977-2010, doi:10.1016/S0967-0637(98)00070-3.

Nikurashin, M., and R. Ferrari (2011). Global energy conversion rate from geostrophic flows into internal lee waves in the deep ocean. *J. Geophys. Lett.*, **38**, L08610.

Najjar, R. G., and R. F. Keeling (1997). Analysis of the mean annual cycle of the dissolved oxygen anomaly in the World Ocean. *Journal of Marine Research*, **55**, 117–151.

Oschlies, A., and V. Garcon (1998). Eddy-induced enhancement of primary production in a model of the North Atlantic Ocean. *Letters to Nature*, **394**, 1994-1997.

Planas, D., Q. Hc, S. Agust, C. M. Duarte, T. C. Granata, and I. D. Ciencias (1999). Nitrate uptake and diffusive nitrate supply in the Central Atlantic. *Limnol. Oceanog.*, **44 (1)**, 116-126.

Platt, T. and S. Sathyendranath (1988). Oceanic Remote Primary Production: Estimation by Remote Sensing at Local and Regional Scales. *Science*, **241**, 1613–1620.

Platt, T., C. Caverhill, and S. Sathyendranath (1991). Basin-Scale Estimates of Oceanic Primary Production by Remote Sensing: The North Atlantic. *Journal of Geophysical Research*, **96(C8)**, 15147–15159.

Polzin, K. L., J. Toole, J. Ledwell, and R. Schmitt (1997). Spatial variability of Turbulent Mixing in the Abyssal Ocean. *Science*, **276**, 93-96, doi:10.1126/science.276.5309.93.

Rainville, L. (2004). Observations of energetic high-wavenumber internal waves in the Kuroshio. *Journal of Physical Oceanography*, **34**, 1495-1505.

Riser, S. C. and K. S. Johnson (2008). Net production of oxygen in the subtropical ocean. *Nature*, **451**, 323–325.

Risien, C. M. and D. B. Chelton (2008). A Global Climatology of Surface Wind and Wind Stress Fields from Eight Years of QuikSCAT Scatterometer Data. *Journal of Physical Oceanography*, 38, 2379–2413.

Roemmich, D. S. Riser, R. Davis, and Y. Desaubies (2004). Autonomous profiling floats: Workhorse for broad-scale observations. *Mar. Technol. Soc.*, **38**, 21-29.

Sabine, C. L., R. A. Feely, N. Gruber, R. M. Key, K. Lee, J. L. Bullister, R. Wanninkhof, C. S. Wong, D. W. R. Wallace, B. Tilbrook, F. J. Millero, T. H. Peng, A. Kozyr, T. Ono, and A. F. Rios (2004). The oceanic sink for anthropogenic CO2. *Science*, **305**, 367–371.

Samelson, R. (1998). Large-Scale Circulation with Locally Enhanced Vertical Mixing. *Journal of physical oceanography*, **28**, 712-726.

Sarmiento, J., and N. Gruber (2002). Sinks for Anthropogenic Carbon. *Phys. Today* **55**, 30–36.

Siegel, D. D. Court, D. Menzies, P. Peterson, S. Maritorena, and N. Nelson (2008). Satellite and in situ observations of the bio-optical signatures of two mesoscale eddies in the Sargasso Sea. *Deep Sea Research Part II: Topical Studies in Oceanography*, **55**, 1218-1230, doi:101016/j.dsr.2008.01.012.

Siegel, D., P. Peterson, D. J. McGillicuddy, S. Maritorena, and N. Nelson (2011). Bio-optical footprints created by mesoscale eddies in the Sargasso Sea. *Journal of Geophysical Research*, **38**, L13608.

Siegel, D. A., D. McGillicuddy, and E. A. Fields (1999). Mesoscale eddies, satellite altimetry, and new production in the Sargasso Sea. *Journal of Geophysical Research*, **104**, 13359-13379.

Simmons, H. (2004). Tidally driven mixing in a numerical model of the open ocean general circulation. *Ocean Modelling*, **6 (3-4)**, 245-263, doi:10.1016/S1463-5003(03)00011-8.

Sonnerup, R. E., S. Mecking and J. L. Bullister (2013). Transit time distributions and oxygen utilization rates in the Northeast Pacific Ocean from chlorofluorocarbons and sulfur hexafluoride. *Deep Sea Research Part I: Oceanographic Research Papers*, **72**, 61-71, doi:10.1016/j.dsr.2012.013.

Stanley, R. H. R., S. C. Doney, W. J. Jenkins, and D. E. Lott, III (2012). Apparent oxygen utilization rates calculated from tritium and helium-3 profiles at the Bermuda Atlantic Time-series Study site. *Biogeosciences*, **9**, 1969–1983.

Sverdrup, H. U. (1953). On conditions for the vernal blooming of phytoplankton. *J. Cons. int. Explor. Mer.*, **18**, 287-295.

Takeshita, Y., T. R. Martz, K. S. Johnson, J. N. Plant, D. Gilbert, S. C. Riser, C. Neill, and B. Tilbrook (2013). A climatology-based quality control procedure for profiling float oxygen data. *Journal of Geophysical Research: Oceans*, **118**, 5640–5650, doi:10.1002/jgrc.20399.

Westberry, T., M. J. Behrenfeld, D. A. Siegel, and E. Boss (2008). Carbon-based primary productivity modeling with vertically resolved photoacclimation. *Global Biogeochem. Cycles*, **22**, GB2024, doi:10.1029/2007GB003078.

Whalen, C. B., L. D. Talley, and J. A. MacKinnon (2012). Spatial and temporal variability of global ocean mixing inferred fom Argo profiles. *Geophysical Research Letters*, **39 (18)**, L18612, doi:10.1029/2012GL053196.

Wilkerson, F. P., A. M. Lassiter, R. C. Dugdale, A. Marchi, and V. E. Hogue (2006). The phytoplankton bloom response to wind events and upwelled nutrients during the CoOP

WEST study. *Deep Sea Research Part II: Topical Studies in Oceanography*, **53 (25-26)**, 3023-3048, doi:10.1016/j.dsr2.2006.07.007.

Wu, L., Z. Jing, S. Riser, and M. Vsbeck (2011). Seasonal and spation variations of Southern Ocean diapycnal mixing from Argo profiling floats. *Nature Geoscience*, **4 (6)**, 363-366, doi:10.1038/ngeo1156.

Wunsch, C. (1975). Deep ocean internal waves: What do we really know? *Journal of Geophysical Research*, **80 (3)**, 339-343.

Wyrtki, K. (1981). An estimate of equatorial upwelling in the Pacific. *J. Phys. Oceanogr.*, **11**, 1205-1214.